



UNIVERSITÀ
DEGLI STUDI
DI PADOVA

Sede Amministrativa: Università degli Studi di Padova

Dipartimento di Tecnica e Gestione dei Sistemi Industriali

CORSO DI DOTTORATO DI RICERCA IN: Ingegneria Meccatronica e dell'Innovazione Meccanica del Prodotto

CICLO: XXXII

WIND-INDUCED FATIGUE SIMULATION APPROACH FOR STEEL MEGASTRUCTURES

Tesi redatta con il contributo finanziario di Cimolai S.p.A.

Coordinatore: Ch.mo Prof. Daria Battini

Supervisore: Ch.mo Prof. Filippo Berto

Co-Supervisore: Ing. Marco Antonello

Dottorando : Alberto Lorenzon

Abstract

WIND-INDUCED FATIGUE is the phenomenon of progressive degradation and, eventually, rupture in structural elements due to continuous cyclic action of wind. The assessment of wind-induced fatigue is in general an extremely demanding and multidisciplinary activity. In fact, it requires multiple blocks which range from the simulation of wind action, simulation of structural dynamic response, climatic statistics analysis, local stress analysis and detailed fatigue calculations. For some structural cases, i.e. simple cantilever structures, light poles, traffic signals, closed formulations for assessing this loading have been proposed in recent years in literature and standards.

The proposed research focuses, on the contrary, on large, complex steel structures, often called megastructures, which can be very sensitive to wind action and for which the calculation of wind-induced fatigue is not feasible using closed formulations and which is an underdeveloped subject in literature. Since megastructures are unique, simulations are necessary all along the design process, including both wind simulation and structural analysis. Up to now, wind tunnels have been the standard tool for simulating wind loading, but recent advances in High-Performance Computing (HPC), have also permitted to use numerical approaches of Computational Wind Engineering (CWE), which adopt Computational Fluid Dynamics (CFD) models.

This thesis proposes a complete approach for the calculation of wind-induced fatigue in megastructures where CFD is introduced in the fatigue design process, making the process entirely numerical. Since CFD must respond to strict requirements related to accuracy, robustness and computational cost, an original development is pro-

posed in the context of the recent and promising class of Partially Averaged Navier Stokes (PANS) models. New PANS models are developed in view of the application on transient analyses on large steel structures. These models are validated using standard benchmark cases showing improvements compared to reference models. Finally, a complete calculation of wind-induced fatigue is shown relative to the real-world application of a stadium roof thus proving the feasibility and the results of the procedure, where PANS models are envisioned as the missing link to perform an entirely numerical calculation at reasonable computational cost.

Abstract

FATICA INDOTTA DA VENTO è il termine utilizzato per identificare il fenomeno del progressivo degrado e, in ultima, della rottura degli elementi strutturali a causa della continua azione ciclica del vento. La valutazione della fatica indotta dal vento è in generale un'attività estremamente impegnativa e multidisciplinare. Infatti, richiede blocchi multipli che vanno dalla simulazione dell'azione del vento, alla simulazione della risposta dinamica strutturale, all'analisi statistica climatica, all'analisi delle sollecitazioni locali e ai calcoli dettagliati della fatica. Per alcuni casi strutturali, come strutture a sbalzo semplici, pali della luce, segnali stradali, sono state proposte negli ultimi anni in letteratura e nelle norme, formulazioni chiuse per la valutazione di questo fenomeno.

La ricerca proposta si concentra, al contrario, su grandi e complesse strutture in acciaio, spesso chiamate megastrutture, che possono essere molto sensibili all'azione del vento e per le quali il calcolo della fatica indotta dal vento non è realizzabile con formulazioni chiuse e che è un argomento ancora poco sviluppato in letteratura. Poiché le megastrutture sono uniche, molteplici simulazioni sono necessarie lungo tutto il processo di progettazione. Le gallerie del vento sono state tradizionalmente lo strumento standard per simulare il carico del vento, ma i recenti progressi nell'High-Performance Computing (HPC), consentono ora di inserire nel processo anche gli approcci numerici dell'Ingegneria Computazionale del Vento (CWE), che adottano i modelli tipici della Fluidodinamica Computazionale (CFD).

Questa tesi propone un approccio completo per il calcolo della fatica indotta dal vento in megastrutture dove la fluidodinamica computazionale è introdotta nel processo

di progettazione della fatica, rendendo il processo interamente numerico. Poiché una simulazione CFD deve rispondere a severi requisiti di precisione, robustezza e costi di calcolo, viene proposto uno sviluppo originale nel contesto dei recenti e promettenti modelli PANS (Partially Averaged Navier Stokes). Sono quindi sviluppati all'interno del progetto di ricerca nuovi modelli PANS, in vista della loro applicazione ad analisi transitorie su grandi strutture in acciaio. Questi modelli sono validati utilizzando casi standard, esibendo miglioramenti rispetto ai modelli di turbolenza di riferimento. Infine, viene mostrato un calcolo completo della fatica indotta dal vento in relazione all'applicazione reale al caso del tetto di uno stadio, dimostrando così la fattibilità e i risultati della procedura, nel quale i modelli PANS sono considerati come l'anello mancante per eseguire un calcolo interamente numerico con oneri computazionali ragionevoli.

Contents

1	Introduction	1
1.1	Background and motivations	1
1.2	Reference	12
2	Turbulence models for wind loads: a critical review	17
2.1	Turbulence models for wind loading simulations	17
2.1.1	Theoretical framework	18
2.1.2	Reynolds-averaged Navier-Stokes (RANS) equations	20
2.1.3	Standard $k - \varepsilon$	21
2.1.4	Realizable $k - \varepsilon$ model	23
2.1.5	MMK and LK models	25
2.1.6	$v^2 - f$ model	25
2.1.7	LES approach	27
2.1.8	PANS approach	30
2.2	Atmospheric wind turbulence reproduction in Wind Tunnel tests	37
2.3	Critical review	41
2.4	Reference	42
3	The problem of wind-induced fatigue	47
3.1	Wind-induced fatigue	47
3.1.1	Cycle counting procedure	47
3.2	Fatigue calculation	59

Contents

3.2.1	Nominal stress method	59
3.2.2	Modified nominal stress	63
3.2.3	Estimation of the fatigue damage	65
3.3	Reference	69
4	Simulation-based approach for wind-induced fatigue calculation of megastructures	73
4.1	Complete procedure	73
4.2	Wind simulation	75
4.3	Modal analysis	79
4.4	Statistical analysis of wind data	80
4.5	Cycle-counting	83
4.6	Loading of local shell FE model	89
4.7	Detailed fatigue calculation	90
4.7.1	Base material checks	90
4.7.2	Welded joints checks	91
5	New Partially Averaged Navier Stokes model development and validation	97
5.1	Highlights	97
5.2	Realizable $k - \varepsilon$ PANS equations	98
5.3	$\overline{v^2} - f$ with variable C_μ PANS equations	100
5.4	Model validation	103
5.4.1	Flow around square cylinder	103
5.4.2	Backwards facing step	109
5.5	Conclusions and future developments	117
5.6	Reference	118
6	Application: wind-induced fatigue calculation of a stadium roof	121
6.1	Highlights	121
6.2	Case study	122
6.3	Dynamical properties	125
6.4	Statistical analysis of wind data	127
6.5	Wind simulation	133
6.5.1	Wind Tunnel Test	133
6.5.2	Computational Wind Engineering simulation	138
6.6	Modal analysis	142
6.7	Cycle counting	147

Contents

6.8	Detailed fatigue design	154
6.8.1	Approach for fatigue design	154
6.8.2	Calculation of damage	156
6.9	Conclusions	160
6.10	Acknowledgements	161
7	Conclusions	163

CHAPTER *1*

Introduction

1.1 Background and motivations

The definition of fluctuating, time-dependent wind loads acting on large steel structures is necessary for the assessment of a time-dependent structural response to wind action. This was a long due application that emerged in conjunction with the rise in building sizes and weight optimization. In fact, as buildings and bridges become larger and more weight-optimized, they become also more sensitive to the dynamic effects of wind.

In the case of structurally simple structures, high-cycle wind-induced fatigue collapse is a well-documented phenomenon for which the characteristics of the relevant dynamic excitation due to the wind can be defined aprioristically. In case of larger and more complex structures, this type of phenomenon is not as easily recognizable and accountable. This research considers the latter type of structures as they represent a typical case in which, as of today, regulations require to consider the phenomenon of wind-induced fatigue but do not appropriately address the phenomenon scientifically and operatively. International standards such as EN 1993-1-1:2005+A1:2014 [10], Annex C have recently reinforced the request to consider the fatigue phenomenon for the design of large steel structures. The size of the structure is implicitly part of the concept

Chapter 1. Introduction

of Consequence Class and the large size almost automatically leads to fatigue calculations. Large steel structures, such as stadiums, transportation hubs, industrial roofs and airport terminals, are characterized as light, flexible and sensitive to the random wind loading. Although they are sufficiently rigid to restrict strong aero-elastic phenomena, they are sufficiently flexible to allow a significant dynamic response. Moderate and frequent wind actions can thus lead to accumulation of fatigue damage and potential structural failure without exceeding design wind actions. The risk of in-service failures is enhanced by the large size of these structures that also affects the potential number of imperfections, as first studied by Davidenkov [9].

The study of the wind-induced fatigue is an evolving topic which is constantly widening to most structural applications and, in latest decades, it has gained an ever increasing attention by researchers and industry. In fact, the advent of advanced calculation tools and high-strength materials has made even the most complex structures to become slender and lighter, and consequently more susceptible to stress fluctuations linked to wind turbulence, which can progressively damage the structure through the mechanisms of fatigue. Initially, research involved structures such as traffic signals, light poles, antenna towers and wind turbines and, more recently, literature has also widened to the study of its effect on more complex structures like offshore lattice flare booms and suspended bridges decks. However, in the case of a megastructure, the assumptions underlying the available methods are often incompatible with its characteristics, as will be highlighted below.

Many research efforts have been dedicated to developing closed-form methods that allow to calculate fatigue damage. The work of the research group of Repetto and Solari is particularly important, as their research led in 2018 to the inclusion, for the first time, of an analytical procedure for the calculation of wind-induced fatigue within a common code, the CNR-DT 207 R1/2018 "Instructions for the evaluation of wind actions and effects on buildings" [91] and opens the way to an implementation at the level of European Standards. In 2002, Repetto and Solari [34] focused their research on the study of the fatigue damage due to gust-excited alongwind vibrations and proposed a closed-form method that allowed to derive a histogram of the stress cycles and fatigue life of slender structures such as towers, chimneys, poles and masts. In the same year, Holmes [17] also proposed a closed formulation for calculating the phenomenon of alongwind load fatigue, including both narrow-band and broad-band response. Subsequently, Repetto [32] proposed a counting method applicable to different bimodal processes, frequent in the dynamic response of structures, taking into account two independent contributions: the first, due to large cycles, linked with the pseudo-envelope

1.1. Background and motivations

of the process, the second, induced by small cycles related to the high frequency component. This method was then further improved and utilized in [36], in the hypothesis of Gaussian process and alongwind wind actions. Since wind induced fatigue is sensitive to moderate wind speeds, for which stable or unstable atmospheric conditions may exist, Repetto and Solari [73] also took into account the effects of wind field conditions. The complete method was then applied to realize a backwards diagnosis of the fatigue failures of two slender structures [37], exhibiting a good prediction accuracy. In 2012, Repetto and Solari completed the work [38] proposing a complete approach to evaluate the alongwind-induced fatigue of structures and structural elements also splitting the method in two alternative options, one simpler and more conservative, the other, more complex and detailed. This formulation was finally introduced in the new version of the Italian CNR wind instructions [91].

However, despite their great novelty, such closed-form approaches are still not always applicable. First of all, the procedure is applicable for alongwind loads, and thus it would not be usable for the calculation of wind-induced fatigue in complex large roofs. A great understanding of the phenomena of excitation at every point of the structure is also required, and this is hardly possible in any geometrically complex structure that does not fall within the types proposed by the standards, for which dynamic response parameters are not available. Moreover, frequency approaches are not able to take into account non-linear effects of load, large deformations and plasticity and, in addition, the power spectrum of critical stresses due to dynamic wind load may not be activated at narrow-band by the influence of the background components of the incident turbulence [13], laterally induced vibrations, the directional effects of wind and structural damping.

For these reasons, in recent years some researchers have focused on the use of time domain dynamic analysis for the calculation of wind-induced fatigue damage. Kvittem and Moan [23] procedure a time-domain procedure for the fatigue assessment of a semi-submersible wind turbine; [6] compared different time-domain methods for the fatigue assessment of offshore wind turbine jacket substructure.

Jia [20] developed an approach for calculating wind induced fatigue on tubular structures such as flare booms, taking into account the effects of the joint probability of speed and direction, and the increase in drag due to large displacements, finding a high dependance of the fatigue damage on the across-wind components and on the directionality effects of the wind loading. Regarding the wind directionality, several studies have shown the importance of its effect on fatigue life. Their influence on the structural dynamic response has been studied by Simiu and Filliben [41], Wen [44] and Kem-

Chapter 1. Introduction

per [21]. Kemper evaluated the impact of the "worst direction" approach used by EN 1991-1-4 B.3, underlining its tendency to excessively overestimate fatigue damage.

In this thesis, the focus is placed on the case of large steel structures, such as large stadium or industrial roofs, which are usually characterized by complex geometries, with a skeleton consisting of a reticular structure structure covered with a cladding and have a dynamic wind response influenced by a wide frequency spectrum. Due to the complexity of coherent turbulent structures around megastructures that generate a state of time-varying stress induced by the wind, the way in which load histories are defined is fundamental. A series of approaches used in literature and industrial practice to define a fatigue spectrum from a wind load are given in the following sections.

Characterization of wind loading for wind-induced fatigue

The determination of the statistical distribution of fatigue cycles still represents one of the most important problems in fatigue analyses as wind is a random loading and, especially in case of complex structures, the load spectrum varies with the position. The process for the determination of wind-induced fatigue is dependent on the characteristics of the available wind loading data. In fact, depending on the availability of test (or experimental) data, it might be necessary to introduce stochastic assumptions about the characteristics of the wind excitation. In literature, many studies of wind-induced fatigue have been performed. A series of studies are here referred and described with the aim of identifying how the wind loading is treated with different approaches, with the purpose of discussing a possible role of CFD.

Wind loading from on-site measurements

Ideally, assuming that the transient wind loading is known for the complete lifetime of a structure, and that the complete time history of stresses is available at every location, an appropriate cycle counting method such as the rainflow cycle counting can be applied and the fatigue damage can be evaluated using Palmgren-Miner rule. This could be the case of a full-scale structure built on site with the availability of data from a structural health monitoring system. If time series obtained from full scale measurements are available, usually they cover only a limited period compared to the life of the structure and it is necessary to perform a statistical analysis in order to obtain a complete joint probability density function that takes into account mean wind speed and direction. As a practical application, Xu et al. [45] performed fatigue calculation due to buffeting of a long suspension bridge, based on data measured on site, where the distribution of the complete population of wind speed at the bridge site is built by using Weibull distribution. Such a situation is clearly not the case of design phases, but this type of

data can still be very useful for validating or calibrating models.

Wind loading from stochastic approach

Often only mean or peak pressure coefficients are available by wind tunnel tests or literature and the fluctuating wind action must be modelled by applying principles of random dynamics as first shown by Davenport [95], or by generating synthetic time histories using Monte Carlo algorithms.

The first approach, which is performed in frequency domain, requires a comprehension of the characteristics of the wind loading on the structure or on the structural component. Two different types of stationary random processes can be distinguished: narrow-band and wide band [17]. In narrow-band processes it is possible to identify a predominant frequency response, such as in case of along-wind response of structures with low natural frequencies or cross-wind vortex shedding of circular cylindrical structures. In wide band processes, the PSD has relevant values over a broad interval of frequencies, with a large background response peak. In case of complex structures, the wide-band component can be dominant. As pointed out in [35] these methods are able to provide elegant solutions but are difficult to use in practical applications; moreover, the link between the stochastic characteristics of excitations and those of the structural response is easily determinable only when the structural model is linear [7].

Many closed form formulations [5, 17, 29, 35] to assess the wind-induced fatigue damage in narrow-band and wide band hypothesis have been proposed.

As an example, Petrov [114] executed the calculation of the fatigue life of a tower-shaped steel monument. The wind load was applied by considering that stress fluctuations of the static, resonant and quasi-static stresses in the structure are assumed to be statistically independent processes.

Wind loading from test measurements

The availability of wind test data obtained from a wind tunnel represents a typical case in the design of a megastructures.

In case time series of pressures are available, time domain-based methods are applicable. A series of instantaneous pressure fields on a whole building for different wind speeds and for different wind directions are measured in a boundary layer wind tunnel, on a fixed (not flexible) scaled model of the structure. The instantaneous stress can be calculated by performing modal analysis, also including the resonant part of the wind load. The application of deterministic counting method such as the rain-flow counting algorithm to time series of stresses, provides the total fatigue damage by using the Miner's law. In order to predict the fatigue life of the structure, statistical property of the on-site wind are considered. As underlined in [39], rain-flow cycles counting of

Chapter 1. Introduction

long time series is the approach that is most widely used in different fields and among codes and is part of the framework of classical fatigue theory.

The study performed by Flamand et al. [102] falls in this category. The authors performed fatigue analyses for the cables design of a large steel stadium exposed to wind. Boundary layer wind tunnel provided the time series of the pressures on a 1:200 scaled fixed model of the stadium. Using a FE model, the calculation of stress time series due to quasi-static and resonant wind components was then performed. A rain-flow counting method was then used to build the fatigue load spectrum and the total damage was evaluated using Palmgren-Miner rule. In order to calculate the number of cycles for each stress group, the authors used site wind data measured over 30 years to calculate the probability of occurrence of every wind speed. Still, the authors limited the calculations to a component, such as the cables, where the fatigue phenomenon is not dependent on details and do not require local fatigue methods.

Although experimentally onerous, this type of approach allows the identification of wind flow characteristics without the introduction of aprioristic assumptions about the relevant spectral components for the structural response. It is noted that the availability of the time series of the pressures in all positions of the structure fits well with the use of FE models.

Although, to date, wind tunnels are clearly the preferred tool for obtaining a wind load history acting on a large structure, a numerical alternative to experimental approaches is possible. Although these approaches present some challenges for them to be successfully used for this purpose, at a procedural level they can be framed in a similar way to experimental approaches, and promise to become a powerful design tool allowing for great flexibility, as will be further discussed in Chapter 4.

Detailed fatigue assessment

Global approaches, and in particular nominal stress, and hot-spot stress, are, to date, the most commonly used methods for the fatigue design of welded joints, together with a series of classified structural details and related S-N curves, as discussed by Hobbacher [14, 104]. Nominal stress is the basis of most codes (IIW recommendations [103], Eurocode 3, 1-9 [87]) and has been accepted by major industries. Despite this, even though it is conceptually easy to define by the classical principles of beam theory, there is no clear definition of nominal stress, nor recommendation on how to derive this value from the finite element stress plot, which provides local stresses [14, 104]. Hobbacher observed that the lack of any local concept in several new fatigue design codes leaving the determination of the nominal stress from FEA results to the engineer-

1.1. Background and motivations

ing assessment of the designer.

IIW provides a series of general recommendations for performing nominal stress calculations:

- the meshing can be simple and coarse since it is not needed to evaluate the stresses concentration factor;
- the nominal stress should be evaluated at a distance from the weld toe that is sufficiently large in order to avoid stress concentration effects, but not too large as stresses underestimation could occur. This distance is generally chosen as 1 or 1.5 times the wall thickness apart from the weld toe;
- the suggested element types to be used can be plane, such as quadrilateral element, or solid, such as tetrahedral and hexagonal elements. However, the extrapolation of stresses from Gauss points should be avoided, preferring extrapolation from centroid points. This ensures that the stress is the results of an average procedure.

These recommendations are clearly not sufficient to provide a robust fatigue design. As hot-spot stress based approaches are known to require complex conditions on mesh generation as shown in [18] (Fig. 1.1) and are not as widely accepted as the nominal stress, many local approaches have been developed in the last two decades.

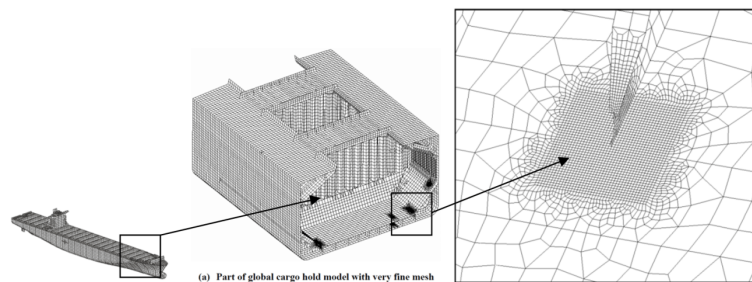


Figure 1.1: *Very fine mesh suggested to be used for hot spot stress based approaches [18]*

Some of the most relevant methods are the effective notch stress method, as formulated by Radaj [31], the notch stress intensity approach [25] and the Strain Energy Density (SED) approach has been formulated by Lazzarin and Zambardi [26]. Compared to other methods, SED approach does not require extremely refined meshes while maintaining its robustness.

Chapter 1. Introduction

Wind-induced fatigue in megastructures

The previous brief discussion on the state of the art of the problem of wind induced fatigue highlights the number of different solutions proposed so far to this subject, and the dependence on the type of structure and the type of wind load. Wind-induced fatigue literature is still fragmented and incomplete. All authors highlight the complexity of the problem, involving meteorological aspects, defining the wind load, calculating the stress cycles based on the aerodynamic response, and estimating the damage, however no exhaustive simulation-based approach has emerged so far. In case of large structures, the problem is further complicated because of the difficulties in properly modelling the time and space variant wind pressure fields, their aerodynamic behaviour, the geometry of the details. The assessment of the wind-induced fatigue for large steel structures is also a computationally demanding task; by considering a typical number of 500 joints and estimating the number of welds components at a ratio 10:1, each of which requires up to 28 checks, the total number of weld checks is of the order of 10^5 , most of which need to be performed all along each weld length. In general, the prediction of wind-induced fatigue life requires first the description of wind loading and, then the estimation of fatigue damage. Hobbacher reported in [14] that the exact knowledge of the actions is one of the most relevant issues and a source of many uncertainties in fatigue calculations, and that only evaluations of the stress history can be made for many applications: this is particularly true for the case of wind excitation. A typical approach for the description of wind loading is the generation of time series of pressure fluctuations by adopting semi-analytical approaches, together with the assumption of Gaussian random fluctuations. However, as shown in [109], the hypothesis of Gaussian loads can result in non-conservative fatigue life estimates. Moreover, the characteristics of wind pressures depend on the geometry, on the location and on the wind direction and semi-analytical models find a difficult application when the geometry of the structure becomes complex. In such cases, evaluation of wind loading is alternatively performed with the aid of wind tunnel tests. In wind tunnels, it is in fact, possible to describe the spectral features of the natural wind and to provide simultaneous measurements of instantaneous pressures at various locations [3]. Wind tunnel tests are frequently performed in the workflow for the design of large complex structures, but often in case of buildings, execution times and costs of these tests do not allow to frame wind tunnel tests in early design stages, where multiple design iterations may be needed, framing them as a one-shot test campaign to validate a final design. Also, since wind tunnels are obviously based on limited-size and the test is performed on scaled models, many fluid non-dimensional numbers that are representative of the flow

1.1. Background and motivations

in the prototype scale, cannot be represented in reduced scale, e.g. the Reynolds number. In fact, by reducing the geometric scale by hundreds or even thousands of times, it would be necessary to increase by the same amount the wind speed at which the model is excited in the wind tunnel. Since this is almost never possible, it is usually impossible to faithfully reproduce the Reynolds number in a scaled simulation and it is necessary to carry out engineering considerations to justify the absence of phenomena related to the different number of Reynolds between the model and the prototype. In the case of structures with curved geometries particularly sensitive to this dependence, different surface roughnesses are often used to correct this phenomenon as much as possible; this is, however, a technological limit whose effects are difficultly accountable. As wind-induced fatigue is sensitive to in-service wind conditions, relative to wind speeds lower than the design wind speed, the effects of the reduced scale are expected to increase in relation to this phenomenon.

These drawbacks give rise to the interest and the search for a practical instrument capable of providing fluctuating wind loads numerically with a sufficient level of reliability. As Computational Fluid Dynamics (CFD) over the last decades has emerged as a tool which has been successfully used to determine static wind loads on practical applications such as buildings, large roofs and bridges, an extension of its use for this purpose is desirable.

Until recently, this was not be considered feasible, because of various factors, i.e. the high computational cost involved with the use of advanced turbulence models due to the extremely high number of computational cells and to the extremely low time steps which are required to obtain high-fidelity time-dependent series of instantaneous pressures, the difficulty to model natural wind and the fact that CFD is still a relatively recent tool. Many of these problems were outlined especially where peak-type values needed to be predicted in order to allow for a wind-resistant design and gust evaluation, for example in AIJ guidelines [79, 80].

In particular, ISO 4354:2009 "Wind Actions on Structures" [19] was very categorical in stating that:

with the current state of development of CFD techniques, such methods are not able to fully reproduce the fluctuating flow characteristics required to obtain the appropriate fractile of the extreme value distribution of pressure coefficients, or the correct correlations between fluctuating pressure coefficients over the surface to give large area (or global) force or moment coefficients.

In ten years since the release of the ISO 4354, a wide number of studies and develop-

Chapter 1. Introduction

ments in CFD have improved the ability of such methods of evaluating fluctuating flow characteristics. Now, many of these drawbacks have been (or are being) overcome:

- even though Moore's law has slowed down in recent years, the advent of many High Performance Computing (HPC) facilities and the spread of Cloud Computing technologies, which have already been implemented by all major commercial and open-source CFD software suppliers, are contributing to an unprecedented availability of computational resources, allowing to execute more advanced and burdensome simulations. In the field of research, it is worth mentioning the large computing power gained by Cineca with its Marconi system. For the industrial world, all the main players in the technological world now offer services that can offer on-demand computing power at competitive prices, such as Amazon EC2 and Microsoft Azure.
- A new generation of the so-called "hybrid" turbulence models is being developed and validated to provide high quality results with lower computational effort [57, 125]. These models usually combine the high-fidelity of DNS (Direct Numerical Simulation) and LES (Large Eddy Simulation) approaches to the simplicity and robustness of RANS (Reynolds Averaged Navier Stokes) models.
- A series of inflow generators has been developed, e.g. the Consistent Discrete Random Flow Generation (CDRFG) [46] or the Divergence Free Synthetic Eddy Method (DFSEM) [30], which are able to create in the computational domain a consistent set of synthetic coherent turbulent structures that reproduce the natural turbulence spectrum.
- CFD has been applied with good results for assessing peak loads on buildings on recent studies [27, 40].

The fact that CFD techniques are experiencing an unprecedented phase of growth and that they are increasingly approaching maturity and applicability also in the case of civil structures is demonstrated by the recent release of the new CNR-DT 207 R1/2018 "Instructions for the evaluation of wind actions and effects on buildings" [91], which has reserved a full Chapter on the description of the features and of the capabilities of CFD models, stating the suitability of scale-resolving CFD models for the computation of integral wind loads and of peak wind loads on buildings, both at preliminary design phase and final design phase. The recent advances of CFD turbulence models are reviewed in Chapter 2 with a practical attention to their potential use for the determination of wind-fatigue loads on buildings and large structures. Since there is not, at

1.1. Background and motivations

the moment, an universal turbulence model available for every application, the choice of models which are able to correctly represent the complexity of coherent turbulent structures on buildings is fundamental in this evaluation and still represents a relevant research topic for industrial CFD [48], hence a review of studies that involve various turbulence models is presented with the aim of addressing the most efficient turbulence models for the application on civil structures.

Recently, research into wind-induced fatigue has also accelerated rapidly. The same document cited earlier, the CNR-DT 207 R1/2018, was the first "quasi-standard" document to present a complete procedure for the calculation of wind-induced fatigue. The fact that this document introduces the two themes at the same time is not by chance, but rather indicates that they are very topical and that they may now converge for the first time.

Whereas the determination of the fluctuating wind loads is a major issue today, the actual fatigue calculation of a complex structure is not yet a completely solved problem. Hobbacher [14] noted that in almost every modern structural project, the use of FE models is often at the center of design workflow. As FEA determines notch stresses and not nominal stress, it is necessary to process the information provided by the models, but, unfortunately, no common code guides the designer in the determination of nominal stress from FEA results. The choice of an appropriate method is thus fundamental to obtain a sound evaluation of fatigue damage and it is addressed in Chapter 3.

Available methods for wind-induced fatigue, at the moment, fall short when a complete simulation chain is needed, such as in the case of megastructures. Megastructures are in fact unique and their design is deeply based on simulation, both on structural side and on aerodynamic side. An original simulation-based procedure to calculate the fatigue damage distribution within a complex steel megastructure is thus proposed by this research. The procedure starts from the experimental or numerical wind simulation, evaluates the structural global dynamic response of the structure using FE models, extracts the fatigue loading accounting climatic statistics and calculates the fatigue damage using advanced local fatigue methods on local shell FE models. The procedure is outlined in Chapter 4. The assessment of wind actions in Wind Tunnels is usually performed with the purpose of designing the structure for Ultimate Limit State (ULS), i.e. for the determination of the design actions for resistance checks, and in few cases, also for the assessment of wind-induced vibrations for confort studies. The nature of the question of determining wind-induced fatigue necessitates certain "restrictions," the key one being focusing on only those large steel structures that are sufficiently stiff to limit significant aero-elastic phenomena. Studying the problem for lightweight

Reference

structural systems, such as cable-supported structures and membrane structures, would involve modeling their aeroelastic behavior, which is not the topic of the current study.

The possibility of envisioning CFD techniques as the missing link to make the simulation of wind-induced fatigue completely numerical even in cases of complex structures appears within reach. Since the development of promising hybrid models is still recent and still requires efforts of improvement and validation, two original turbulence models based on the Partially Averaged Navier Stokes equations are here developed and are discussed in Chapter 5. In this chapter, the theoretical development of these two new models and two applications to literature benchmark cases are presented: the case of the square cylinder and the case of the backwards facing step. The aim of this original development is to improve the quality of the results compared to the literature models, in particular with regard to the fluctuating components of the flow.

Finally, in Chapter 6, the application of the complete procedure for the calculation of wind-induced fatigue in the real-life test case of a stadium roof is presented. It is shown how the complete procedure is feasible using data typically available for the design of a megastructure and enables the structural engineer to gain a deep knowledge on the fatigue loading acting on potentially every point of the structure without the need of imposing rigid hypothesis on wind loading or on structural response.

1.2 Reference

- [1] *EN 1993-1-9 Eurocode 3: Design of steel structures - Part 1-9: Fatigue*. European Committee for Standardization, Brussels, 2005.
- [2] Haitham Aboshosha, Ahmed Elshaer, Girma T. Bitsuamlak, and Ashraf El Damatty. Consistent inflow turbulence generator for LES evaluation of wind-induced responses for tall buildings. *Journal of Wind Engineering and Industrial Aerodynamics*, 142:198–216, 2015.
- [3] Aerospace Division of ASCE. *Wind Tunnel Studies of Buildings and Structures*. American Society of Civil Engineers, Reston, VA, mar 1999.
- [4] B. Basara. PANS method as a computational framework from an industrial perspective. *Notes on Numerical Fluid Mechanics and Multidisciplinary Design*, 130:3–17, 2015.

- [5] Denis Benasciutti and R Tovo. Frequency-based fatigue analysis of non-stationary switching random loads. *Fatigue and Fracture of Engineering Materials and Structures*, 30(11):1016–1029, 2007.
- [6] Chi Yu Chian, Yi Qing Zhao, Tsung Yueh Lin, Bryan Nelson, and Hsin Haou Huang. Comparative study of time-domain fatigue assessments for an offshore wind turbine jacket substructure by using conventional grid-based and monte carlo sampling methods. *Energies*, 11(11), 2018.
- [7] Federico Cluni, Vittorio Gusella, and Filippo Ubertini. A parametric investigation of wind-induced cable fatigue. *Engineering Structures*, 29(11):3094–3105, 2007.
- [8] CNR. CNR DT 207 R1/2018 Istruzioni per la valutazione delle azioni e degli effetti del vento sulle costruzioni, 2018.
- [9] N. N. Davidenkov, E. Shevandin, and F. Wittmann. The Influence of Size on the Brittle Strength of Steel. *International Journal of Applied Mechanics*, 68, 1946.
- [10] EN 1993-1-1+A1. Eurocode 3: Design of steel structures- Part 1-1:General rules for buildings. *European Committee for Standardization*, 2014.
- [11] Jochen Fröhlich and Dominic von Terzi. Hybrid LES/RANS methods for the simulation of turbulent flows. *Progress in Aerospace Sciences*, 44(5):349–377, 2008.
- [12] Sharath Girimaji and Khaled Abdol-Hamid. Partially-Averaged Navier Stokes Model for Turbulence: Implementation and Validation. *43rd AIAA Aerospace Sciences Meeting and Exhibit*, (January):1–14, 2005.
- [13] M. Gu, Y. L. Xu, L. Z. Chen, and H. F. Xiang. Fatigue life estimation of steel girder of Yangpu cable-stayed bridge due to buffeting. *Journal of Wind Engineering and Industrial Aerodynamics*, 80(3):383–400, 1999.
- [14] A. F. Hobbacher. The new IIW recommendations for fatigue assessment of welded joints and components - A comprehensive code recently updated. *International Journal of Fatigue*, 31(1):50–58, 2009.
- [15] A. F. Hobbacher. *Recommendations for Fatigue Design of Welded Joints and Components*. 2016.

Reference

- [16] Adolf F. Hobbacher. New developments at the recent update of the IIW recommendations for fatigue of welded joints and components. *Steel Construction*, 3(4):231–242, 2010.
- [17] J. D. Holmes. Fatigue life under along-wind loading - Closed-form solutions. *Engineering Structures*, 24(1):109–114, 2002.
- [18] IACS. *CSR - Common Structural Rules for Bulk Carriers*. Number July. 2012.
- [19] ISO. ISO 4354:2009 - Wind actions on structures. 4354, 2009.
- [20] Junbo Jia. Wind and structural modelling for an accurate fatigue life assessment of tubular structures. *Engineering Structures*, 33(2):477–491, 2011.
- [21] Frank H. Kemper and Markus Feldmann. Fatigue life prognosis for structural elements under stochastic wind loading based on Spectral Methods, Part II: Non-linear Structures. *Proceedings of the 8th International Conference on Structural Dynamics, EUROLYN 2011*, (June):1636–1643, 2011.
- [22] K Suresh Kumar and T Stathopoulos. Fatigue analysis of roof cladding under simulated wind loading. *Journal of Wind Engineering and Industrial Aerodynamics*, 77-78:171–183, 1998.
- [23] Marit I. Kvittem and Torgeir Moan. Time domain analysis procedures for fatigue assessment of a semi-submersible wind turbine. *Marine Structures*, 40:38–59, 2015.
- [24] B E Launder and D B Spalding. The numerical computation of turbulent flows. *Computer Methods in Applied Mechanics and Engineering*, 3(2):269–289, 1974.
- [25] P Lazzarin and R. Tovo. A Notch Intensity Factor Approach To the Stress Analysis of Welds. *Fatigue Fracture of Engineering Materials and Structures*, 21(9):1089–1103, 1998.
- [26] P. Lazzarin and R. Zambardi. A finite-volume-energy based approach to predict the static and fatigue behavior of components with sharp V-shaped notches. *International Journal of Fracture*, 112(3):275–298, 2001.
- [27] Yuriy Marykowskyi. *CFD study of pressure peaks on building facades*. Master’s degree thesis, POLITECNICO DI MILANO, 2019.

- [28] Albert A. Petrov. Dynamic response and life prediction of steel structures under wind loading. *Journal of Wind Engineering and Industrial Aerodynamics*, 74-76:1057–1065, 1998.
- [29] G Petrucci and B Zuccarello. Fatigue life prediction under wide band random loading. *Fatigue and Fracture of Engineering Materials and Structures*, 27(12):1183–1195, 2004.
- [30] R. Poletto, T. Craft, and A. Revell. A new divergence free synthetic eddy method for the reproduction of inlet flow conditions for les. *Flow, Turbulence and Combustion*, 91(3):519–539, 2013.
- [31] Dieter Radaj. *Design and Analysis of Fatigue Resistant Welded Structures*. Woodhead Publishing, Cambridge, 1990.
- [32] M. P. Repetto. Cycle counting methods for bi-modal stationary Gaussian processes. *Probabilistic Engineering Mechanics*, 20(3):229–238, 2005.
- [33] M P Repetto and G Solari. Wind-induced fatigue of structures under neutral and non-neutral atmospheric conditions. *Journal of Wind Engineering and Industrial Aerodynamics*, 95(9-11):1364–1383, 2007.
- [34] Maria Pia Repetto and Giovanni Solari. Dynamic alongwind fatigue of slender vertical structures. *Wind and Structures, An International Journal*, 5(6):527–542, 2002.
- [35] Maria Pia Repetto and Giovanni Solari. Dynamic crosswind fatigue of slender vertical structures. *Wind and Structures, An International Journal*, 5(6):527–542, 2002.
- [36] Maria Pia Repetto and Giovanni Solari. Bimodal alongwind fatigue of structures. *Journal of Structural Engineering*, 132(6):899–908, 2006.
- [37] Maria Pia Repetto and Giovanni Solari. Wind-induced fatigue collapse of real slender structures. *Engineering Structures*, 32(12):3888–3898, 2010.
- [38] Maria Pia Repetto and Giovanni Solari. Closed-form prediction of the alongwind-induced fatigue of structures. *Journal of Structural Engineering (United States)*, 138(9):1149–1160, 2012.
- [39] Maria Pia Repetto and Alessio Torrielli. Long term simulation of wind-induced fatigue loadings. *Engineering Structures*, 132:551–561, 2017.

Reference

- [40] M. Ricci, L. Patruno, and S. de Miranda. Wind loads and structural response: Benchmarking LES on a low-rise building. *Engineering Structures*, 144:26–42, 2017.
- [41] Emil Simiu and James J. Filliben. Wind direction effects on cladding and structural loads. *Engineering Structures*, 3(3):181–186, 1981.
- [42] Tetsuro Tamura. Towards practical use of LES in wind engineering. *Journal of Wind Engineering and Industrial Aerodynamics*, 96(10-11):1451–1471, 2008.
- [43] Tetsuro Tamura, Kojiro Nozawa, and Koji Kondo. AIJ guide for numerical prediction of wind loads on buildings. In *The Fourth International Symposium on Computational Wind Engineering (CWE2006)*, Yokohama, pages 161–164, 2006.
- [44] Yi Kwei Wen. Wind direction and structural reliability: II. *Journal of Structural Engineering (United States)*, 110(6):1253–1264, 1984.
- [45] Y. L. Xu, T. T. Liu, and W. S. Zhang. Buffeting-induced fatigue damage assessment of a long suspension bridge. *International Journal of Fatigue*, 31(3):575–586, 2009.

CHAPTER 2

Turbulence models for wind loads: a critical review

2.1 Turbulence models for wind loading simulations

Turbulence is one of the most complex phenomena in nature and there is, as of today, no way to entirely describe the time-dependent features of every aspect of a turbulent flow of engineering interest. The physics of turbulence is completely described by Navier Stokes' equations. However, a sufficiently accurate direct numerical solution of such equations requires the simulation of almost all turbulent vortices, and since the smaller vortices are associated with characteristic lengths and times which are of many orders of magnitude smaller than the larger ones, it is impossible to obtain direct numerical solutions of Navier Stokes' equations for turbulent flows.

All this complexity is due to the intrinsic properties of a turbulent flow. A turbulent flow is in fact defined by Hinze [84] as:

an irregular condition of flow in which the various quantities show a random variation with time and space coordinates, so that statistically distinct average values can be discerned.

Chapter 2. Turbulence models for wind loads: a critical review

Among their main characteristics, turbulent flows:

- Have a wide range of significant scales;
- Are always dissipative, and through a cascade process energy is transferred from larger eddies to smaller eddies through kinetic energy, and ultimately the smaller eddies dissipate into heat through molecular viscosity;
- It is possible to describe the field variables statistically;

While the origin in turbulence modeling can be traced back to the end of the 19 – *th* century, when Reynolds performed his research on time-averaged properties of turbulent flows and when Boussinesq introduced the concept of an eddy-viscosity, by finding a relation between turbulent stresses and molecular gradient-diffusion process, only after the advent of the computer, with the birth of computational fluid dynamic, it has found a widespread application in the industrial field.

The most important development in turbulence modeling was probably the extensive work of Launder and Spalding [24] on the two-equation models, which led to the release of the popular Standard $k - \varepsilon$ model. Despite the fact that its limits and defects have been extensively studied, and numerous models modified to overcome the known limitations in its formulation have been proposed, the Standard model, and, in general the Reynolds-Averaged Navier Stokes (RANS) approach, has remained, until now, the most popular model of turbulence among CFD practitioners.

This is not by chance, since these models are simple to use, computationally affordable and stable. However, this class of models is just not able to provide accurate information regarding the fluctuating components of the flow and, for this reason, several techniques, like Large Eddy Simulation or hybrid models, such as Partially Averaged Navier Stokes (PANS), have emerged in the latest decades to address this lack.

A brief theoretical introduction about turbulence models for CFD is reported below, together with a series of corresponding practical applications from literature regarding wind flow around civil structures and, in general, bluff bodies of practical interest.

The following is a selection of turbulence models for which relevant applications are available in literature. For an extensive review of turbulence approaches the interested reader is directed to papers such as, for example, Argyropoulos et al. [47].

2.1.1 Theoretical framework

Navier-Stokes equations provide every information about all the features of a turbulent flow. In general, Navier-Stokes equations for homogeneous incompressible fluids of

2.1. Turbulence models for wind loading simulations

constant viscosity can be expressed as:

$$\frac{\partial \mathbf{v}}{\partial t} + (\mathbf{v} \cdot \nabla) \mathbf{v} = -\frac{1}{\rho} \nabla p + \nu \nabla^2 \mathbf{v} \quad (2.1)$$

$$\nabla \cdot \mathbf{v} = 0 \quad (2.2)$$

As shown by many [47, 61, 78], limitations in computational power make it impossible for now and the foreseeable future to provide a complete solution to the equations in complex turbulent flows of practical interest.

This is because turbulence is by nature an irregular condition of flow, with strong non-linearity and large width in the scales of length, time and velocity.

The use of mathematical models that simulate the physics of turbulence without analytically resolving Navier-Stokes equations has thus emerged as a necessity even though, in practice, this affects the ability of the computational method of describing the actual irregular behavior of the flow. In relation to computational wind engineering, this translates into a partial description of the wind spectral density and thus to neglecting potentially relevant dynamic effects on structures. The different approaches to turbulence modeling differ fundamentally in this ability, and change the portion of turbulence which is described by solving Navier-Stokes equations against the portion that is instead modeled.

The three major classes of models are:

- *DNS (Direct Numerical Simulation)*: Navier-Stokes equations are numerically simulated at all length and at all scales and therefore no turbulence model is used. Its computational requirements are far too high for most practical application.
- *LES (Large Eddy Simulation)*: the major vortices are analytically solved while sub-grid eddies are described with sub-grid models.
- *RANS (Reynolds Averaged Navier-Stokes)*: the entire flow is averaged and the turbulence is modeled using various approaches, reducing the physical complexity of turbulent flow and, thus, neglecting all the effects of turbulent fluctuations.

Between these classes are also present many other models that aim to realize improvements in the description of the physics while obtaining reduction in computational cost. An ample review of hybrid RANS-LES models has been provided in the paper of Fröhlich and von Terzi [57]. Some of the most successful hybrid approaches are:

- *VLES (Very Large Eddy Simulation)* [66]

Chapter 2. Turbulence models for wind loads: a critical review

- *DES (Detached Eddy Simulation)* [77]
- *PANS (Partially-Averaged Navier-Stokes)* [125]

In recent years, Partially Averaged Navier-Stokes methods proposed by Girimaji et al. [60] have gained appreciation for their ability to improve the evaluation of fluctuating components of the flow at reasonable computational cost and for their easy implementation into existing RANS solvers [57] and many researchers are foreseeing their adoption for industrial purposes [48].

2.1.2 Reynolds-averaged Navier-Stokes (RANS) equations

RANS models have been for many years the only tool available to calculate the features of a turbulent flow in relevant, complex applications [62]. The fundamental concept of RANS methods lies in Reynolds decomposition of Navier-Stokes equations: turbulent flow is described as a random variation around a mean value. The Reynolds-averaged Navier-Stokes equations can be written as [84]:

$$\rho \frac{\partial U_i}{\partial t} + \rho U_j \frac{\partial U_i}{\partial x_j} = -\frac{\partial p}{\partial x_i} + \frac{\partial}{\partial x_j} (2\mu S_{ji} - \overline{\rho u'_j u'_i}) \quad (2.3)$$

while time-averaged mass-conservation is identical to the instantaneous:

$$\frac{\partial U_i}{\partial x_i} = 0 \quad (2.4)$$

In RANS equation, the quantity $\overline{\rho u'_j u'_i}$ is known as the *Reynolds stress tensor*:

$$\overline{\rho u'_j u'_i} = \rho \tau_{ij} \quad (2.5)$$

The unknowns are 10: one pressure, three velocity components, six Reynolds stress tensor components, while the equations are four. To solve the problem, it is necessary to introduce more equations. This is called the “closure problem” and the system is resolved with the aid of turbulence models.

Hanjalic [61] defines the major requirements and expectation over a turbulence model such that the model should be able to mimic faithfully the flow and turbulence physics in a broad range of flow situations, to satisfy mathematical rigor and physical constraints, to be manageable with relatively simple numerical methods and to serve as a computational tool for predicting new complex flows. Most critical physical effects are typically flow separation and recirculation, unsteadiness, wall proximity, three-

2.1. Turbulence models for wind loading simulations

dimensionality, swirl, rotation, streamline curvature, extra strain rate and buoyancy. In case of buildings and large structures the focus should be on the flow phenomena of separation, unsteadiness, wall proximity and three-dimensionality.

At the moment there is no turbulence model which is able to accomplish perfectly all these features, but many have proven to be reliable and effective in multiple types of complex flows.

2.1.3 Standard $k - \varepsilon$

Theoretical framework

The most popular two-equation model is certainly the Standard $k - \varepsilon$ model, which is based on the physical hypothesis that the production of dissipation should be proportional on the Boussinesq hypothesis and to the production of turbulent kinetic energy. The following equations define a Standard $k - \varepsilon$ model:

$$\tau_{ij} = \frac{2}{3}k\delta_{ij} - \nu_t \left(\frac{\partial \bar{u}_i}{\partial x_j} + \frac{\partial \bar{u}_j}{\partial x_i} \right) \quad (2.6)$$

$$\nu_t = C_\mu \frac{k^2}{\varepsilon} \quad (2.7)$$

$$\frac{\partial k}{\partial t} + \bar{u}_i \frac{\partial \bar{u}_i}{\partial x_i} = -\tau_{ij} \frac{\partial \bar{u}_i}{\partial x_j} - \varepsilon + \frac{\partial}{\partial x_i} \left(\frac{\nu_t}{\sigma_k} \frac{\partial k}{\partial x_i} \right) + \nu \nabla^2 k \quad (2.8)$$

$$\frac{\partial \varepsilon}{\partial t} + \bar{u}_i \frac{\partial \varepsilon}{\partial x_i} = -C_{\varepsilon 1} \frac{\varepsilon}{k} \tau_{ij} \frac{\partial \bar{u}_i}{\partial x_j} - C_{\varepsilon 2} \frac{\varepsilon^2}{k} + \frac{\partial}{\partial x_i} \left(\frac{\nu_t}{\sigma_\varepsilon} \frac{\partial \varepsilon}{\partial x_i} \right) + \nu \nabla^2 \varepsilon \quad (2.9)$$

where:

- τ_{ij} is the Reynolds stress tensor;
- k is the turbulent kinetic energy;
- δ_{ij} is the Dirac delta;
- ν_t is the eddy viscosity;
- \bar{u}_i is the mean velocity vector;
- μ is the molecular viscosity;
- ε is the turbulent dissipation rate.

The constants assume the following approximate values of $C_\mu = 0.09$, $\sigma_k = 1.0$, $\sigma_\varepsilon = 1.3$, $C_{\varepsilon 1} = 1.44$, $C_{\varepsilon 2} = 1.92$.

Practical application

The standard $k - \varepsilon$ model is one of the most widely adopted turbulence models and thus a very large literature of test cases for this turbulence model is available, also in relation to buildings and large structures. Despite its popularity this model is also known for its defects, which have been highlighted by many relevant authors. Among them, in AIJ guide for numerical prediction of wind loads on buildings [81], the model has been reviewed for the case study of a steady wind flow over a cubic low-rise building: for a wind angle normal to windward face, the model greatly overestimates turbulent kinetic energy k , and consequently the surface pressure distribution, in the impinging region around the frontal corner of the roof; it also shows limited ability to reproduce correct flow physics as the flow separation from the frontal corner of the roof is not reproduced. For skew wind directions, the model cannot reproduce the conical vortices, which can be observed in wind tunnel and in more advanced simulations.

In [65] the model was used to calculate the time dependent wind load on the Commonwealth Advisory Aeronautical Council (CAARC) standard tall building, which is a relevant validation case referred by multiple authors. The authors reported that, although the $k - \varepsilon$ model causes a typical over-estimation of the pressure distributions on the front face, the under-estimation of the pressure distribution on the rear face is such as to lead to a drag coefficient calculation of 20% lower than the reference results. As expected, the model proved to be unsuitable for evaluating the fluctuating features of the flow.

Because of these deficiencies, relevant guideline papers such as Franke et al. [55] have discouraged the use of the Standard $k - \varepsilon$ model in the simulation of wind engineering problems in favour of more advanced linear or non-linear eddy viscosity models.

Modifications of the Standard $k - \varepsilon$ model

The coefficients for the standard $k - \varepsilon$ model were devised specifically to predict certain low-Reynolds-number phenomena in boundary layer and duct flows [53]. Since the first introduction of the model, many of its weaknesses in more complex flows have been outlined, such as excessive production of turbulent shear stress and excessive levels of turbulence in stagnation and impingement regions. The standard $k - \varepsilon$ model is therefore generally considered unsuitable for wind engineering studies of buildings especially for cases with high separation [55, 80], frequent for large steel structures exposed to wind. As large CPU time requirements of more sophisticated CFD approaches such as DNS and LES make them unfit for an application to many wind engineering

2.1. Turbulence models for wind loading simulations

problems of practical interest and, given the interests to maintain the computational advantages of the RANS framework, various authors have proposed improved versions of the standard $k - \varepsilon$ model to overcome the deficiencies of the original model without compromising its simplicity: other closure models differ essentially by the choice of the modeled equations along with the equation of turbulent kinetic energy. Many modified models have been developed over the years, here only a few are presented in the following sections:

- Realizable $k - \varepsilon$ model;
- RNG $k - \varepsilon$ model;
- LK and MMK $k - \varepsilon$ models;
- $v^2 - f$ model;

2.1.4 Realizable $k - \varepsilon$ model

The Realizable $k - \varepsilon$ is one of the most popular and effective alternatives to the Standard formulation. A different eddy-viscosity formulation is introduced, based on the realizability constraints, the positivity of normal Reynolds stresses and Schwarz's inequality for turbulent shear stresses. In fact, it can be shown that, in standard $k - \varepsilon$, if the strain is large enough, the normal stress, which is a positive quantity by definition, becomes negative and the Schwarz inequality for shear stresses can be violated. In order to fix this, the coefficient C_μ is variable, in opposition to standard $k - \varepsilon$, where it is fixed. This model improved the performance of the standard $k - \varepsilon$ model in various flows including jets, mixing layers, channels, boundary layers, separated flows, and completely removed the spreading rate anomaly of planar and round jets. The equations for the Realizable $k - \varepsilon$ [132] are:

$$\frac{\partial k}{\partial t} + U_j \frac{\partial k}{\partial x_j} = \frac{\partial}{\partial x_j} \left(\frac{\nu_t}{\sigma_k} \frac{\partial k}{\partial x_j} \right) - \overline{u_i u_j} \frac{\partial U_i}{\partial x_j} - \varepsilon \quad (2.10)$$

$$\frac{\partial \varepsilon}{\partial t} + U_j \frac{\partial \varepsilon}{\partial x_j} = \frac{\partial}{\partial x_j} \left(\frac{\nu_t}{\sigma_\varepsilon} \frac{\partial \varepsilon}{\partial x_j} \right) + C_1 S \varepsilon - C_2 \frac{\varepsilon^2}{k + \sqrt{\nu \varepsilon}} \quad (2.11)$$

where:

$$S = \sqrt{2S_{ij}S_{ij}} \quad (2.12)$$

$$C_1 = \max \left\{ 0.43, \frac{\eta}{5 + \eta} \right\} \quad (2.13)$$

Chapter 2. Turbulence models for wind loads: a critical review

$$\eta = S \frac{k}{\varepsilon} \quad (2.14)$$

The Reynolds stress term $-\overline{u_i u_j}$ is defined as:

$$-\overline{u_i u_j} = \nu_t \left(\frac{\partial U_i}{\partial x_j} + \frac{\partial U_j}{\partial x_i} \right) - \frac{2}{3} k \delta_{ij} \quad (2.15)$$

the turbulent viscosity is:

$$\nu_t = C_\mu \frac{k^2}{\varepsilon} \quad (2.16)$$

the realizability conditions impose that:

$$\overline{u_\alpha} \geq 0 \quad (\alpha = 1, 2, 3) \quad (2.17)$$

$$\frac{\overline{u_\alpha u_\beta^2}}{\overline{u_\alpha^2} \overline{u_\beta^2}} \leq 1 \quad (\alpha = 1, 2, 3; \beta = 1, 2, 3) \quad (2.18)$$

The coefficient C_μ is not constant and is defined as:

$$C_\mu = \frac{1}{A_0 + A_s \frac{k U^*}{\varepsilon}} \quad (2.19)$$

$$U^* \equiv \sqrt{S_{ij} S_{ij} + \tilde{\Omega}_{ij} \tilde{\Omega}_{ij}} \quad (2.20)$$

$$\tilde{\Omega}_{ij} = \Omega_{ij} - 2\epsilon_{ijk} \omega_k \quad (2.21)$$

$$\Omega_{ij} = \overline{\Omega}_{ij} - \epsilon_{ijk} \omega_k \quad (2.22)$$

where Ω_{ij} is the mean rate-of-rotation tensor viewed in a rotating reference frame with the angular velocity ω_k . The model constant A_0 and A_s are given by

$$A_0 = 4.0, \quad A_s = \sqrt{6} \cos \phi \quad (2.23)$$

$$\phi = \frac{1}{3} \cos^{-1}(\sqrt{6}W), \quad W = \frac{S_{ij} S_{jk} S_{ki}}{\tilde{S}^3}, \quad \tilde{S} = \sqrt{S_{ij} S_{ij}}, \quad S_{ij} = \frac{1}{2} \left(\frac{\partial u_j}{\partial x_i} + \frac{\partial u_i}{\partial x_j} \right) \quad (2.24)$$

The model constants are:

$$C_{1\epsilon} = 1.44, \quad C_2 = 1.9, \quad \sigma_k = 1.0, \quad \sigma_\epsilon = 1.2 \quad (2.25)$$

2.1.5 MMK and LK models

The LK (Launder-Kato) [67] modification of the Standard $k - \varepsilon$ model was developed with the aim of improving the original model in its ability to capture vortex-shedding flows. The authors of the model ascribe the poor predictions of the Standard model in these flows to the excessive generation of turbulence energy $P_k = C_\mu \varepsilon S^2$ in the vicinity of the stagnation point. As a solution, a modification of the energy production rate was proposed, by modifying the original production term introducing the vorticity term in the equation:

$$P_k = C_\mu \varepsilon S \Omega \quad (2.26)$$

where Ω is the dimensionless vorticity parameter and S is the dimensionless strain parameter:

$$\Omega = \frac{k}{\varepsilon} \sqrt{\frac{1}{2} \left(\frac{\partial U_i}{\partial x_j} - \frac{\partial U_j}{\partial x_i} \right)^2}; \quad S = \frac{k}{\varepsilon} \sqrt{\frac{1}{2} \left(\frac{\partial U_i}{\partial x_j} + \frac{\partial U_j}{\partial x_i} \right)^2} \quad (2.27)$$

This modification allows to reduce the energy production near the stagnation point, where the deformation is nearly irrotational ($\Omega \rightarrow 0$) while simple shear flow is not affected.

MMK (Murakami, Mochida, Kondo) model [82] was developed on the basis of Launder-Kato (LK) modification and aimed at the elimination of turbulence overproduction at the impinging region by correcting the production term, which is defined as $P_k = \nu_t S^2$ in the Standard model, where:

- $\nu_t = C_\mu \frac{k^2}{\varepsilon}$
- $S = \sqrt{\frac{1}{2} \left(\frac{\partial \langle u_i \rangle}{\partial x_j} + \frac{\partial \langle u_j \rangle}{\partial x_i} \right)^2}$

The turbulent viscosity equation is modified to:

$$\nu_t = C_\mu^* \frac{k^2}{\varepsilon} \quad (2.28)$$

where $C_\mu^* = C_\mu \frac{\Omega}{S}$ (for $\frac{\Omega}{S} < 1$) and $C_\mu^* = C_\mu$ (for $\frac{\Omega}{S} > 1$).

2.1.6 $v^2 - f$ model

Durbin's $v^2 - f$ [53] is based on the elliptic relaxation concept and introduces two additional equations, in addition to k and ε : one for the velocity scale v^2 and one for the

Chapter 2. Turbulence models for wind loads: a critical review

elliptic relaxation function f . The main target of this model is to improve the modelling of near-wall turbulence. The model has further been modified by Lien and Kalitzin [127] and by Davidson, Nielsen and Svingsson [123] to improve its efficiency and stability. The transport equation of dissipation, of turbulent kinetic energy, of wall normal stress and of elliptic relaxation function, considering the latter modifications, are:

$$\frac{\partial \varepsilon}{\partial t} + u_j \frac{\partial \varepsilon}{\partial x_j} = \frac{C_{\varepsilon 1} P_k - C_{\varepsilon 2} \varepsilon}{T} + \frac{\partial}{\partial x_j} \left[\left(\nu + \frac{\nu_t}{\sigma_\varepsilon} \right) \frac{\partial \varepsilon}{\partial x_j} \right] \quad (2.29)$$

$$\frac{\partial k}{\partial t} + u_j \frac{\partial k}{\partial x_j} = P_k - \varepsilon + \frac{\partial}{\partial x_j} \left[\left(\nu + \frac{\nu_t}{\sigma_k} \right) \frac{\partial k}{\partial x_j} \right] \quad (2.30)$$

$$\frac{\partial \overline{v'^2}}{\partial t} + u_j \frac{\partial \overline{v'^2}}{\partial x_j} = \overline{v'^2}_{source} - 6 \overline{v'^2} \frac{\varepsilon}{k} + \frac{\partial}{\partial x_j} \left[\left(\nu + \frac{\nu_t}{\sigma_k} \right) \frac{\partial \overline{v'^2}}{\partial x_j} \right] \quad (2.31)$$

where

$$\overline{v'^2}_{source} = \min \left[kf, -\frac{1}{T} \left[(C_1 - 6) \overline{v^2} - \frac{2}{3} k (C_1 - 1) + C_2 P_k \right] \right] \quad (2.32)$$

$$L^2 \frac{\partial^2 f}{\partial x_j^2} - f = \frac{1}{T} \left[(C_1 - 6) \frac{\overline{v^2}}{k} - \frac{2}{3} (C_1 - 1) \right] - C_2 \frac{P_k}{k} \quad (2.33)$$

Production term P_k is defined as:

$$P_k = \overline{u'_i u'_j} \frac{\partial u_i}{\partial x_j} = 2 \nu_t S_{ij} \frac{\partial u_i}{\partial x_j} \quad (2.34)$$

where eddy viscosity is defined as:

$$\nu_t = \min \left[C_{\mu, SKE} \frac{k^2}{\varepsilon}, C_\mu \overline{v'^2} T \right] \quad (2.35)$$

Where $S_{ij} = 0.5 \left(\frac{\partial u_i}{\partial x_j} + \frac{\partial u_j}{\partial x_i} \right)$.

T and L are the turbulent time scale and turbulent length scale:

$$T = \max \left[\frac{k}{\varepsilon}, 6 \sqrt{\frac{\nu}{\varepsilon}} \right] \quad (2.36)$$

$$L = C_L \max \left[\frac{k^{(3/2)}}{\varepsilon}, C_\eta \frac{\nu^{3/4}}{\varepsilon^{1/4}} \right] \quad (2.37)$$

2.1. Turbulence models for wind loading simulations

The model coefficients are: $C_\mu = 0.22$, $\sigma_k = 1.0$, $\sigma_\varepsilon = 1.3$, $\sigma_{\varepsilon 1} = 1.4 \left(1 + 0.05\sqrt{k/v^2}\right)$, $C_{\varepsilon 2} = 1.9$, $C_1 = 1.4$, $C_2 = 0.3$, $C_L = 0.23$, $C_\eta = 70$.

2.1.7 LES approach

Theoretical framework

In LES, the large eddies are fully resolved and the smallest, subgrid-scale eddies are modeled. Instead of time-averaging, the resolved (large-eddy) field is separated from the small-eddy (sub-grid) field by using a spatial filtering:

$$u_i = \bar{u}_i + \bar{u}'_i \quad (2.38)$$

where \bar{u}_i is the grid-scale component and \bar{u}'_i is the sub-grid scale component.

The governing equations for incompressible flow are shown in Equation 2.39:

$$\frac{\partial \bar{u}_i}{\partial t} + \frac{\partial}{\partial x_j} (\bar{u}_i \bar{u}_j) = -\frac{1}{\rho} \frac{\partial P}{\partial x_i} + \frac{\partial}{\partial x_j} \left[\nu \frac{\partial \bar{u}_i}{\partial x_j} + \tau_{ij} \right] \quad (2.39)$$

where:

$$\tau_{ij} = - \left(Q_{ij} - \frac{1}{3} Q_{kk} \delta_{ij} \right) \quad (2.40)$$

$$P = \bar{p} + \frac{1}{3} \rho Q_{kk} \delta_{ij} \quad (2.41)$$

$$Q_{ij} = R_{ij} + C_{ij} \quad (2.42)$$

Smagorinsky Lilly model

Smagorinsky developed a model for the Sub-Grid Stresses (SGS) assuming that they follow a gradient-diffusion process similar to molecular motion, whose governing equations are:

$$\tau_{ij} = 2\nu_t S_{ij} \quad (2.43)$$

where $S_{ij} = \frac{1}{2} \left(\frac{\partial \bar{u}_i}{\partial x_j} + \frac{\partial \bar{u}_j}{\partial x_i} \right)$ is the strain rate. The Smagorinsky eddy viscosity is:

$$\nu_T = (C_s \Delta)^2 \sqrt{2S_{ij} S_{ij}} \quad (2.44)$$

where:

- $C_s = 0.1 - 0.2$ is the Smagorinsky coefficient;

Chapter 2. Turbulence models for wind loads: a critical review

- $\Delta = (\Delta_x \Delta_y \Delta_z)^{\frac{1}{3}}$ is the filter width;

It is possible to observe that the size of each computational cell defines the width of the filter through the parameter Δ . This means that the level of grid refinement modifies the SGS model and, consequently, that progressive grid refinements lead to different turbulence models. The accuracy of LES is much dependent on the use of an accurate SGS stress model and in the correct representation of boundary conditions.

Turbulence generation

One of the most relevant advantages of LES over RANS consists in the fact that LES is able to resolve both energy containing spectral subrange and a large part of inertial subrange, while dissipation subrange is modeled, and this allows the introduction of inflow turbulence which follows the von Karman model, similarly to what is done in wind tunnels. This is crucial, as wind speed fluctuations in atmospheric boundary layer obey the von Karman model and this spectrum is used by major wind Standards. One of the most discussed topics in the field of LES model research at the moment is the modeling of the turbulent Atmospheric Boundary Layer (ABL). In literature three different approaches can be found to generate an inflow turbulence for LES [46]:

1. Precursor database method;
2. Recycling method;
3. Turbulent inflow generators.

Both the first and the second methods involve an auxiliary model that is used to calculate the temporal and spatial distribution of the turbulent velocities at the inlet of the targeted zone. These methods have the advantage of generating coherent turbulent structures inside the computational domain, and are particularly suitable if a database of inlets is built to represent different wind and terrain conditions that can be used multiple times. Otherwise, this type of approach is generally considered to be computationally costly as it requires a two-stage analysis.

The third method, on the contrary, employs an algorithm that introduces a synthetic inflow turbulence in the domain that respects the target flow statistics. An example of a inflow turbulence generator suitable for ABL reproduction can be found in [46] with the Consistent Discrete Random Flow Generator (CDRFG) method, which is found to provide an accurate response spectrum compared to the boundary layer wind tunnel. Other types of inflow generators are shown in [30, 64, 85].

2.1. Turbulence models for wind loading simulations

Practical applications

LES has been proven to be capable of providing accurate predictions of wind effects on structures in atmospheric boundary layers which are comparable to wind tunnel experimental data [79]. Among the many studies on LES models present in the literature, the following works concerning simulations of external flows of buildings are worth mentioning:

- In AIJ guide for numerical prediction of wind loads on buildings [81], the use of LES on many wind engineering problems was reviewed, showing its ability in providing accurate predictive values which well match wind tunnel experimental data. The adoption of LES for the calculation of peak wind loads is also foreseen.
- A typical case study where LES has been employed is the study of the flow around standard tall building (CAARC) with/without flow generation models and with/without surrounding buildings [46, 52, 64, 86]. The results of these studies indicated the ability of LES to evaluate steady and unsteady features of the flow, including an accurate description of wind load spectra. Results are compared against other CFD approaches, such as URANS, which fall short in these predictions against reference experimental data from wind tunnels. In particular, in Zhang et al. [86] paper, the analysis of wind-induced vibrations were performed by coupling CFD and structural modal analysis proving good agreement with maximum displacements of the wind-excited structure.
- Other successful application include [74, 83], where LES analyses of flow around bridge section were performed proving good agreement with the experimental results both on steady and unsteady characteristics, and [70], where the flow field around a large roof was studied and mean and rms pressure coefficients was correctly evaluated.

The ability of LES methods to predict stationary and unstable flow characteristics is now well established in literature. However, their applicability in industrial CFD and, in general, to the outside of the research field remains a topic of discussion. In fact, while on the one hand papers such as *"Towards practical use of LES in wind engineering"* from Y. Tamura [79] about a decade ago envisioned a broad use of LES as a tool with reasonable computational cost, other, more recent works [48] observe that even though LES has been more frequently used in the last years, its adoption is still mostly limited to benchmarks and visibility studies because of very high computational costs. Besides that, LES needs a more careful analysis compared to URANS in order to accept the

Chapter 2. Turbulence models for wind loads: a critical review

results, which could represent an obstacle for everyday use in industry and, in particular, LES experiences severe shortcomings in dealing with near-wall flows unless very fine grids are used in the vicinity of the wall.

2.1.8 PANS approach

Partially Averaged Navier-Stokes is a bridging method that allows for a seamless and smooth transition from RANS to DNS, depending on the values of the filter-width control parameters [60]. The filter-width control parameter represent the ratio between unresolved to total kinetic energy and dissipation (in case of PANS $k - \varepsilon$ model). When the filter-width control parameter are equal to unity, the results of the parent RANS model are recovered; when it is equal to zero, Navier-Stokes equations are entirely resolved.

The instantaneous velocity V and pressure p fields for incompressible Navier-Stokes equations are shown in Eq. 2.45 and 2.46:

$$\frac{\partial V_i}{\partial t} + V_j \frac{\partial V_i}{\partial x_j} = -\frac{\partial p}{\partial x_i} + \nu \frac{\partial^2 V_i}{\partial x_j \partial x_j} \quad (2.45)$$

$$\frac{\partial V_i}{\partial x_i} = 0 \quad (2.46)$$

The instantaneous velocity component, V_i , is decomposed into resolved and unresolved parts [125]:

$$V_i = U_i + u_i \quad (2.47)$$

where U_i is the resolved flow velocity component and u_i is the unresolved part. U_i can also be written using the filter operator $\langle \dots \rangle$, which is a constant preserving arbitrary filter:

$$U_i = \langle V_i \rangle \quad (2.48)$$

$$\langle u_i \rangle \neq 0 \quad (2.49)$$

The filtering operation on the instantaneous Navier-Stokes equations produces the governing equations for the resolved velocity field, which are the evolution equations in terms of partially averaged velocity U and pressure $\langle p \rangle = p_u$:

$$\frac{\langle \partial V_i \rangle}{\partial t} + \langle V_j \frac{\partial V_i}{\partial x_j} \rangle = -\frac{\partial p_u}{\partial x_i} + \nu \frac{\partial^2 \langle V_i \rangle}{\partial x_j \partial x_j} \quad (2.50)$$

2.1. Turbulence models for wind loading simulations

$$\frac{\partial^2 p_u}{\partial x_i \partial x_i} = -\left\langle \frac{\partial V_i \partial V_j}{\partial x_j \partial x_i} \right\rangle \quad (2.51)$$

The generalized central second moment [58] is introduced:

$$\tau(A, B) = \langle AB \rangle - \langle A \rangle \langle B \rangle \quad (2.52)$$

as well as the generalized central third moment:

$$\tau(A, B, C) = \langle ABC \rangle - \langle A \rangle \tau(B, C) - \langle B \rangle \tau(C, A) - \langle C \rangle \tau(A, B) - \langle A \rangle \langle B \rangle \langle C \rangle \quad (2.53)$$

Using the definitions of generalized central second moment, and generalized third moment as given by Germano (equation 2.52), the terms in the latter equations are exploited as:

$$\tau(V_i, V_j) = (\langle V_i V_j \rangle - \langle V_i \rangle \langle V_j \rangle) \quad (2.54)$$

$$\tau(V_i, V_j, V_k) = \langle V_i V_j V_k \rangle - \langle V_i \rangle \tau(V_j, V_k) - \langle V_j \rangle \tau(V_k, V_i) - \langle V_k \rangle \tau(V_i, V_j) - \langle V_i \rangle \langle V_j \rangle \langle V_k \rangle \quad (2.55)$$

the evolution equations become:

$$\frac{\partial U_i}{\partial t} + U_j \frac{\partial U_i}{\partial x_j} + \frac{\partial \tau(V_i, V_j)}{\partial x_j} = -\frac{\partial p_u}{\partial x_i} + \nu \frac{\partial^2 U_i}{\partial x_j \partial x_j} \quad (2.56)$$

$$-\frac{\partial^2 p_u}{\partial x_i \partial x_i} = \frac{\partial U_i}{\partial x_j} \frac{\partial U_j}{\partial x_i} + \frac{\partial^2 \tau(V_i, V_j)}{\partial x_j \partial x_j} \quad (2.57)$$

In the PANS equations, $\tau(V_i, V_j)$ is the Sub-Filter Stress (SFS) term, which needs closure. Its evolution equation is given by:

$$\frac{\partial \tau(V_i, V_j)}{\partial t} + U_k \frac{\partial \tau(V_i, V_j)}{\partial x_k} = P_{ij} + \Phi_{ij} - D_{ij} + T_{ij} \quad (2.58)$$

where P_{ij} is the production term, Φ_{ij} is the pressure-correlation term, D_{ij} is the dissipation term and T_{ij} is the transport term of SFS stress, defined as follows:

$$P_{ij} = -\tau(V_i, V_k) \frac{\partial U_j}{\partial x_k} - \tau(V_j, V_k) \frac{\partial U_i}{\partial x_k} \quad (2.59)$$

$$\Phi_{ij} = 2\tau(p_u, S_{ij}) \quad (2.60)$$

S_{ij} is the strain tensor:

$$S_{ij} = \frac{1}{2} \left(\frac{\partial \langle U_i \rangle}{\partial x_j} + \frac{\partial \langle U_j \rangle}{\partial x_i} \right) \quad (2.61)$$

Chapter 2. Turbulence models for wind loads: a critical review

$$D_{ij} = 2\nu\tau \left(\frac{\partial U_i}{\partial x_k}, \frac{\partial U_j}{\partial x_k} \right) \quad (2.62)$$

$$T_{ij} = -\frac{\partial}{\partial x_k} \left(\tau (V_i, V_j, V_k) + \tau (p, V_i) \delta_{jk} + \tau (p, V_j) \delta_{ik} - \nu \frac{\partial \tau (V_i, V_j)}{\partial x_k} \right) \quad (2.63)$$

K_u and ε_u are the PANS unresolved kinetic energy and unresolved dissipation rate and can be defined as:

$$K_u = \frac{1}{2} \tau (V_i, V_j) \quad (2.64)$$

$$\varepsilon_u = \nu\tau \left(\frac{\partial V_i}{\partial x_j}, \frac{\partial V_i}{\partial x_j} \right) \quad (2.65)$$

The subscript u indicates PANS unresolved statistics.

The derivation of a PANS model starts from the RANS parent and hence inherits many of its advantages and disadvantages. As the PANS model is developed on the basis of a parent RANS closure, its performance are affected by the goodness of the parent RANS.

In case of the Standard $k - \varepsilon$ model, the parent equations are defined in section 2.1.3 and the filter-width parameters are defined as:

$$f_k = \frac{K_u}{k} \quad (2.66)$$

$$f_\varepsilon = \frac{\varepsilon_u}{\varepsilon} \quad (2.67)$$

where f_k is the ratio of the unresolved (K_u) to total (k) turbulent kinetic energy and f_ε is the ratio of unresolved (ε_u) to total (ε) dissipation.

Applying PANS approach, the transport equation of the total kinetic energy becomes:

$$\frac{\partial K_u}{\partial t} + U_j \frac{\partial K_u}{\partial x_j} = P_u - \varepsilon_u + T_{ku} \quad (2.68)$$

where

- $P_u = \tau (V_i, V_j) \frac{\partial U_i}{\partial x_j}$ is the production term;
- $T_{ku} = \frac{\partial}{\partial x_j} \left(\frac{\nu_u}{\sigma_{ku}} \frac{\partial K_u}{\partial x_j} \right)$ is the transport term;

Since f_k is a constant, the evolution of the PANS and RANS kinetic energies are related according to:

$$\frac{\partial K_u}{\partial t} + \overline{U_j} \frac{\partial K_u}{\partial x_j} = f_k \left(\frac{\partial k}{\partial t} + \overline{U_j} \frac{\partial k}{\partial x_j} \right) \quad (2.69)$$

2.1. Turbulence models for wind loading simulations

which leads to:

$$\frac{\partial K_u}{\partial t} + U_j \frac{\partial K_u}{\partial x_j} = f_k \left[P - \varepsilon + \frac{\partial}{\partial x_j} \left(\frac{\nu_t}{\sigma_k} \frac{\partial k}{\partial x_j} \right) \right] + (U_j - \bar{U}_j) \frac{\partial K_u}{\partial x_j} \quad (2.70)$$

By equating the LHS term in Eq. 2.68 and 2.70, it is possible to write:

$$P_u + \varepsilon_u + T_{ku} = f_k \left[P - \varepsilon + \frac{\partial}{\partial x_j} \left(\frac{\nu_t}{\sigma_k} \frac{\partial k}{\partial x_j} \right) \right] + (U_j - \bar{U}_j) \frac{\partial K_u}{\partial x_j} \quad (2.71)$$

By equating the source-sink terms,

$$P_u - \varepsilon_u = f_k(P - \varepsilon) \Rightarrow P = \frac{1}{f_k}(P_u - \varepsilon_u) + \frac{\varepsilon_u}{f_\varepsilon} \quad (2.72)$$

Likewise, by equating the advection/transport terms:

$$T_{ku} = \frac{\partial}{\partial x_j} \left(\frac{\nu_t}{\sigma_k} \frac{\partial K_u}{\partial x_j} \right) - (\bar{U}_j - U_j) \frac{\partial K_u}{\partial x_j} = \frac{\partial}{\partial x_j} \left(\frac{\nu_u f_\varepsilon}{\sigma_k f_k^2} \frac{\partial K_u}{\partial x_j} \right) - (\bar{U}_j - U_j) \frac{\partial K_u}{\partial x_j} \quad (2.73)$$

By assuming that the resolved fluctuations do not contribute to sub-filter-stress energy transport (ZT, zero-transport model):

$$(\bar{U}_j - U_j) \frac{\partial K_u}{\partial x_j} = 0 \Rightarrow T_{ku} = \frac{\partial}{\partial x_j} \left(\frac{\nu_u f_\varepsilon}{\sigma_k f_k^2} \frac{\partial K_u}{\partial x_j} \right) = \frac{\partial}{\partial x_j} \left(\frac{\nu_u}{\sigma_{ku}} \frac{\partial K_u}{\partial x_j} \right) \quad (2.74)$$

and therefore, under the ZT assumption, the Prandtl constant for unresolved turbulent kinetic energy is defined as:

$$\sigma_{ku} = \sigma_k \frac{f_k^2}{f_\varepsilon} \quad (2.75)$$

The transport equation for the unresolved turbulent kinetic energy is therefore defined as:

$$\frac{\partial K_u}{\partial t} + U_j \frac{\partial K_u}{\partial x_j} = P_u - \varepsilon_u + \frac{\partial}{\partial x_j} \left[\left(\frac{\nu_u}{\sigma_{ku}} + \nu \right) \frac{\partial K_u}{\partial x_j} \right] \quad (2.76)$$

Similarly, the equation for the unresolved dissipation ε_u is obtained as:

$$\frac{\partial \varepsilon_u}{\partial t} + U_j \frac{\partial \varepsilon_u}{\partial x_j} = C_{\varepsilon 1} \frac{P_u \varepsilon_u}{K_u} - C_{\varepsilon 2}^* \frac{\varepsilon_u^2}{K_u} + \frac{\partial}{\partial x_j} \left(\frac{\nu_u}{\sigma_{\varepsilon u}} \frac{\partial \varepsilon_u}{\partial x_j} \right) \quad (2.77)$$

Where the coefficient $C_{\varepsilon 2}^*$ includes the filter-width coefficients:

$$C_{\varepsilon 2}^* = C_{\varepsilon 1} + \frac{f_k}{f_\varepsilon} (C_{\varepsilon 2} - C_{\varepsilon 1}) \quad (2.78)$$

Chapter 2. Turbulence models for wind loads: a critical review

and the Prandtl coefficient for the unresolved dissipation is:

$$\sigma_{\varepsilon u} = \sigma_{\varepsilon} \frac{f_k^2}{f_{\varepsilon}} \quad (2.79)$$

The various model coefficients are those of the parent RANS $k - \varepsilon$ model, shown in the previous sections.

By following similar approaches, other PANS models have been derived from the basis of existing RANS models:

- $k - \omega$ SST PANS [69];
- $\zeta - f$ PANS [120];
- LRN $k - \varepsilon$ PANS [71]

Each of these models provides some improvement over the Standard $k - \varepsilon$ PANS formulation. The model that has probably found more applications in literature is currently the second in the list ($\zeta - f$ PANS), developed by the research group of Basara, which benefits from a particularly high-performance parent model, such as the $\zeta - f$ derived by Hanjalic. [63].

Practical applications

Despite the fact that the diffusion of the PANS approach is very recent compared to other methodologies, numerous tests on validation cases are already available in literature.

These models have shown good results over the last decade, with performance comparable to even the most computationally demanding LES models and have been widely tested on test cases.

- In [133] a two-stage RANS-PANS simulations was performed to simulate the flow past a square cylinder, using the PANS implementation of $k - \omega$ SST model. First, a RANS simulation allowed for the determination of the initial value of control parameter f_k in each cell by calculating the distribution of turbulence length scale and Kolmogorov length scale. Then PANS simulation is started and the control parameter is constantly updated over time. The results of the simulation, including time series and rms of fluctuating velocities, are generally in good agreement with experiments and they show a low grid-dependency.

2.1. Turbulence models for wind loading simulations

- In [72] a PANS simulation is performed for the flow around a two bluff bodies. The PANS model is developed on the basis of a $\zeta - f$ model and the control parameter f_k is dynamic, being updated at the end of every time step for each point. In the first simulation the flow around a surface mounted cube is computed. The results of PANS using a coarse grid are similar to Unsteady RANS while as the grid is refined the PANS flow structures become similar to those provided by LES.
- A first use of PANS for computational wind engineering purposes has also been reviewed in [52], where the authors remarked the need to provide further insight on its cost effectiveness and prediction accuracy.

Filter parameter definition

As shown by Girimaji [60], the filter-width parameter f_k is related to the smallest resolved length scale η_r in PANS. In fact, it is shown that the smallest resolved scale is proportional to the ratio of local dissipation and local eddy viscosity:

$$\eta_r \sim \left(\frac{\nu_u^3}{\varepsilon} \right)^{\frac{1}{4}} \quad (2.80)$$

By noting that $f_\varepsilon = 1$ and, thus, $\varepsilon_u = \varepsilon$,

$$\nu_u = C_\mu \frac{K_u^2}{\varepsilon_u} \approx C_\mu f_k^2 \frac{k^2}{\varepsilon} \quad (2.81)$$

The resolved-field Kolmogorov scale is:

$$\eta_r = C_\mu^{0.75} f_k^{1.5} \Lambda \quad (2.82)$$

Where $\Lambda = k^{1.5}/\varepsilon$ is the Taylor scale of turbulence. Therefore, by considering that in DNS the grid-spacing should be of the order of the Kolmogorov length scale, Girimaji calculated the limit for the value of f_k :

$$\eta_r = C_\mu^{0.75} f_k^{1.5} \Lambda \sim \Delta \quad (2.83)$$

Where Δ is the smallest grid dimension. The smallest f_k a grid can support at a given location is thus:

$$f_k(x) = \frac{1}{\sqrt{C_\mu}} \left(\frac{\Delta}{\Lambda} \right)^{\frac{2}{3}} \quad (2.84)$$

Chapter 2. Turbulence models for wind loads: a critical review

In the first phase of PANS model development, simulations were carried out considering a fixed f_k value throughout the domain. This type of approach was considered to be preferable for assessing the effects of the filter-width parameters on the model prediction. This approach was followed, for example, by Girimaji for the calculation of the flow past a square cylinder, for the flow past circular cylinder and for a three-dimensional cavity; by Girimaji, Tosh and Frendi [56] for the calculation of flow past a backwards-facing step, Lasksmipathy [69] for the calculation of the flow past a circular cylinder.

The control parameter f_k , which is the ratio of the unresolved turbulent kinetic energy to the total turbulent kinetic energy, can be defined to be variable over space and time. In fact it is shown in that the adoption of a fixed filter parameter f_k is not reasonable and may lead to unphysical solutions. More recently, the adoption of a space- and time-variable f_k has emerged. In 2008, Basara [49] used the original formulation for the lower bound of f_k to calculate a space and time-varying f_k for the calculation of the flow around a bluff body (Ahmed body). With the same formulation, Basara et al. [120] proposed the variable-resolution formulation for the $\zeta - f$ PANS model, which was then also adopted by Mirzaei et al. [129] for the calculation of the flow around two bluff bodies.

Foroutan et al. [124] proposed a new formulation which was stated to have two major advantages compared to the original disequation proposed by Girimaji.

In Foroutan formulation, the control filter parameter f_k is initialized using the equation 2.85 defined by Foroutan et al.

$$f_K = 1 - \left[\frac{\left(\frac{\Delta}{\Lambda}\right)^{\frac{2}{3}}}{0.23 + \left(\frac{\Delta}{\Lambda}\right)^{\frac{2}{3}}} \right]^{4.5} \quad (2.85)$$

where $\Delta = (\Delta_x \Delta_y \Delta_z)^{\frac{1}{3}}$ is the grid length scale and $\Lambda = k^{3/2}/\varepsilon$ is the turbulence integral length scale.

With a variable f_k , a two-stage PANS should be performed. First, the solution is initialized using a steady RANS calculation. This solution allows to define the total turbulent kinetic energy field and to initialize the simulation, in order to avoid numerical instabilities that could emerge by starting the PANS calculation without initialization. Equation 2.85 is then utilized at every time-step to update the value of f_k , on the basis of the averaged fields.

In 2018 [51], the research group of Basara proposed an original PANS formulation to

2.2. Atmospheric wind turbulence reproduction in Wind Tunnel tests

overcome the need of a two-stage approach such as the one proposed by Foroutan. With the new formulation a "scale supplying variable" was introduced as a closure equation for the resolved kinetic energy, avoiding the need for the calculation of the averaged fields and allowing for more efficient and effective time-varying solutions.

The high and recent interest in the PANS approach, together with the encouraging results obtained in the literature, are symptomatic of the potential of a method that could be widely adopted in the coming years also in the industrial field.

2.2 Atmospheric wind turbulence reproduction in Wind Tunnel tests

Wind tunnel testing on small rigid models is now the most common approach for simulating wind loading on complex structures that do not fall within the specific types specified by Standards such as EN 1991-1-4:2005 [100]. The wind tunnel has the ability to create flows that simulate the basic characteristics of natural wind at a certain site. These are associated with flow approaching the site (approaching flow), flow over nearby buildings, and significant topographical features (modifications of near-field flow). Wind tunnels designed to develop this type of flow are classified as boundary-layer wind tunnels (BLWT); an example is reported in Fig. 2.1 representing the BLWT of the Politecnico di Milano.

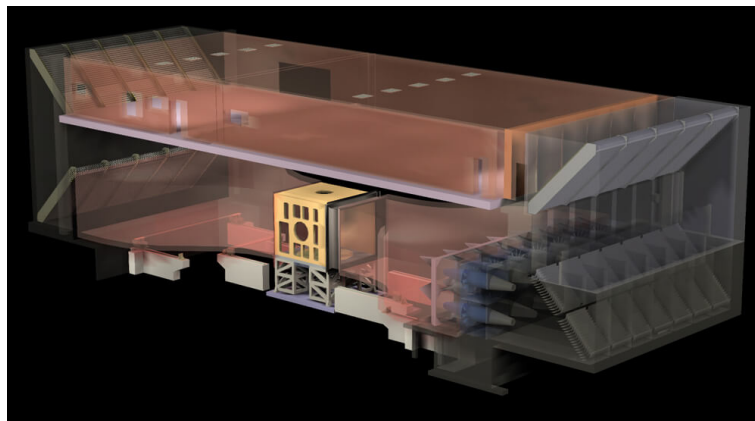


Figure 2.1: *Politecnico di Milano Wind Tunnel facility*

These tunnels are typically 2 to 5 m wide, have a working section of 15 to 30 m long, use air at atmospheric pressure, and usually operate at maximum wind speeds of 10 to 50 m/s. The reproduction of the characteristics of the Atmospheric Boundary Layer (ABL) is usually carried out with the use of various devices, such as spires placed at the entrance of the test section (to obtain the mean velocity and turbulence

Chapter 2. Turbulence models for wind loads: a critical review

profiles), and various obstacles and scaled buildings to accurately reproduce the flow over nearby buildings and surroundings. Strong winds are usually of primary concern to provide the designers with the wind loads corresponding to Ultimate Limit State (ULS) requirements. The approaching flow is generally an isothermal boundary layer for moderate and high wind speeds, i.e. locally stationary conditions persist because the mixing turbulence forces the atmosphere towards neutrality. Hence, WTTs are performed with this assumption in most of the cases. An additional modeling criterion for thermally stratified ABL flows is that for full- and model-scale approach flows, the bulk Richardson number, which reflects the ratio of buoyancy forces to inertia forces, is equivalent. An alternative simulation criterion is that z_g/Lm_0 is equivalent for design and prototype, where z_g is the boundary layer's gradient wind height and Lm_0 is the stability duration of Monin-Obukhov. The influence of the assumption of an isothermal boundary layer on the evaluation of the wind induced fatigue has been investigated by Repetto and Solari [73], who proposed a model of the mean wind speed profile, power spectral density functions and the coherence functions of the turbulence field, based on the Monin-Obukhov length. In general, in the case of neutral atmospheric condition, the mean wind speed increases in stable condition, while in unstable atmosphere it remains almost unchanged; vice versa, the turbulence intensities decrease in stable atmosphere and increase in unstable conditions. Referring to the case of a steel chimney, the author concludes that the effect on the fatigue damage of stable and unstable conditions can compensate each other, and their role only becomes relevant to structures that are sensitive to vortex shedding excitations due to variations in critical wind speed. Further research should be performed for determining the effects of unstable conditions in relation to more complex types of structures.

In the following, the models adopted by the Eurocode 1991-1-4 [100] for the mean wind profile and turbulence in neutral atmospheric conditions are shown. As concerns the mean wind speed profile $V(z)$, the Eurocode provides the following logarithmic expressions based on the definition of the roughness length z_0 :

$$V(z) = V_b k_r \ln \left(\frac{z}{z_0} \right) \quad z_{min} \leq z \leq 200m \quad (2.86)$$

$$V(z) = V(z_{min}) \quad z \leq z_{min} \quad (2.87)$$

where:

- V_b is the basic wind velocity evaluated at 10 m above the ground of terrain category II;

2.2. Atmospheric wind turbulence reproduction in Wind Tunnel tests

- K_r is the terrain factor, given by $k_r = 0.19 \left(\frac{z_0}{z_{0,II}} \right)^{0.07}$;
- $z_{0,II} = 0.05$ is the terrain roughness for terrain of category *II*, as defined by EN-1991-1-4, Clause 4.2;
- z_{min} is the height below which the profile is assumed to be constant.

As far as turbulence modeling is concerned, its description is based on statistical approaches. Relevant parameters are the standard deviation σ_i , the power spectral densities S_i , and the integral scales L_{χ_i} for the i -th velocity component. Based on the definition of turbulence intensities $I_i(z) = \frac{\sigma_i(z)}{V(z)}$, the Eurocode provides the following expression for the longitudinal component I_V :

$$I_V(z) = \frac{1}{\ln(z/z_0)} \quad z_{min} \leq z \leq 200m \quad (2.88)$$

$$I_V(z) = I_V(z_{min}) \quad z \leq z_{min} \quad (2.89)$$

while it suggests to obtain the remaining two components by reducing the vertical one of 25%. The expression of the turbulence intensity of the incoming flow is integrated with the distribution of its frequency energy content through its Power Spectral density (PSD). Starting from the normalized PSD $S_i^* = \frac{f S_i}{\sigma_i^2}$ and the reduced frequency $f_i^* = \frac{f L_{\chi_i}}{V}$, the Eurocode provides the following expression for the normalized PSD of the longitudinal component:

$$S_L^*(z, f) = \frac{6.8 f_L^*(z, f)}{[1 + 10.2 f_L^*(z, f)]^{5/3}} \quad (2.90)$$

The consistent reproduction of the atmospheric boundary layer (ABL) at the wind tunnel scale (model scale) requires a suitable geometric scale choice $\lambda_L = \frac{L_p}{L_m}$, where L_p and L_m represent the characteristic dimension of the roof structure, respectively, at the prototype scale (full scale) and at the model scale. The geometric scale is usually chosen to maintain model equality and prototype ratios of overall structure dimensions as close as possible to the approaching wind's significant meteorological lengths. The latter is usually represented by the z_0 terrain's roughness length, so the geometric scale is chosen to maintain the equality of the Jensen number L_b/z_0 :

$$\left(\frac{L}{z_0} \right)_m = \left(\frac{L}{z_0} \right)_p \quad (2.91)$$

Due to the large size of the structures whose effects of wind are to be studied, a typical

Chapter 2. Turbulence models for wind loads: a critical review

geometric scale is in the order of 1:100, although the scale may be further increased in the case of particularly large structures. The choice results as a compromise between a reasonable simulation of small-scale turbulence and blockage considerations, i.e. the flow speed and distortion effects induced by a high design dimension ratio to the wind tunnel cross section. If the appropriate geometric scale selection is required to ensure consistent ABL modeling, the velocity scale is relatively arbitrary as long as the model and full-scale flows remain aerodynamically similar, i.e. independent of the number of Reynolds. The velocity scale in such situations is determined by practical considerations and instrumentation limitations. In order to discuss this aspect, the governing parameters represented by the reduced frequency f^* (Strouhal number) and the Reynolds number Re are made explicit:

$$f^* = \frac{f \cdot L}{V} \quad (2.92)$$

$$Re = \frac{\rho V \cdot L}{\mu} = \frac{V \cdot L}{\nu} \quad (2.93)$$

where ρ is the air density, and $\nu = \mu/\rho$ is the kinematic viscosity of the fluid.

The scale factor for the frequency λ_f is obtained by applying the equality in the Strouhal number between model and prototype:

$$\lambda_f = \frac{\lambda_L}{\lambda_V} \quad (2.94)$$

being $\lambda_V = \frac{V_p}{V_m}$ the velocity scale. The velocity scale factor can be obtained by imposing the equality in Reynolds number:

$$\lambda_V = \frac{1}{\lambda_L} \quad (2.95)$$

If a geometric scale $\lambda_L = 1 : 100$ is assumed, according to the last equation, it should be $\lambda_V = 100 : 1$. Hence, the mean wind speed in the wind tunnel test should be a hundred times time the full-scale one. As it is not feasible, the Re is not correctly reproduced. However, this does not invalidate the test if the approach flow is Reynolds independent; for this purpose, an additional simulation at a lower wind speed is usually performed. In general, the independence is assured if:

$$\frac{u^* z_0}{\nu} > 2.5 \quad (2.96)$$

where $u^* = \tau_0/\rho$ is the friction velocity and τ_0 is the surface shear stress. Flow correc-

tions for differences between model and full-scale structures Re are sometimes required for curved structures. In general, to improve local flow similarity, curved surfaces of models are roughened. As anticipated above, the velocity scale is usually not determined upon Reynolds number effect, but more often upon considerations of convenience and limitations of the instrumentations. However, its choice is a critical aspect in a fatigue analysis perspective, as it will be discussed in the next chapters.

2.3 Critical review

This review has shown that CFD approach is now able to respond to the needs of wind engineers: there are many studies in literature that have shown good adherence between the turbulent features obtained with CFD models and the one obtained experimentally. In literature, many LES models have been coupled with custom inflow turbulence generators which were able to introduce in computational wind field a natural wind which well describes Von Karman spectrum and which provides appropriate spatial correlation. The ability of these models to correctly describe the turbulent eddies in the inertial subrange is of great significance as turbulent eddies in the inertial subrange have relevant effect on wind-induced fluctuating loads on buildings and structures. Although its use has increased in recent years, LES remains difficult to apply in industrial context due to the high cost and the need to analyze its results carefully.

While in LES only the small, isotropic turbulent scales are modelled, RANS models the entire spectrum. On the other side, RANS models have been the only computational tool available for assessing mean wind forces for many years, but they do not find direct applicability in evaluating complex fluctuating phenomena.

As an alternative to LES, bridging models such as PANS are obtaining more and more approval. PANS models resolve analytically only a predefined part of the fluctuating scales by tuning the parameters of the unresolved-to-total turbulent kinetic energy and dissipation (or specific dissipation, in case of $k - \omega$ PANS models) and they reduce computational efforts while providing good results in time-dependent analyses. As PANS models can be developed on the basis of particular RANS turbulence models, multiple choices can be made about the choice of used turbulence model for the development of a PANS model suitable for an application in large steel structures. The adoption of standard $k - \varepsilon$ as a basis for a PANS model is certainly the simplest from a modelling point of view but the filter parameter f_k should be as small as possible in order to reduce the intrinsic errors of the model; since modified $k - \varepsilon$ models like LK, MMK, Realizable $k - \varepsilon, v^2 - f, \zeta - f$ or $k - \omega$ SST are able to provide generally better

Reference

results in cases of interest for external separated flows, they represent a better choice. In literature, some analyses have already been carried out with such improved models showing positive results as expected. Further research shall be performed for PANS models regarding the description of natural wind turbulence and its utilization for wind engineering application.

For an industrial overview of CFD it is necessary to observe that almost all CFD studies in literature involve simple structural geometry such as, standard tall buildings with rectangular section, low-rise buildings modelled as cubes, cylinders. The introduction of complex geometries of engineering interest does not only require a larger operative effort, but also increases the complexity of the flow phenomena, introducing the need to perform wind tunnel tests or high-resolution CFD studies. In general, the use of CFD methods for the calculation of wind-induced fatigue loads in buildings with the methods currently available appears to be already potentially achievable, if advanced LES models with inflow turbulence generators are coupled to FEA and with fatigue methods that allow to use coarse meshes; in order to adopt it as an autonomous tool for industrial and complex applications as well, it requires further efforts for future development, focusing in particular on the development and validation of stable and accurate hybrid methods like PANS.

2.4 Reference

- [46] Haitham Aboshosha, Ahmed Elshaer, Girma T. Bitsuamlak, and Ashraf El Damatty. Consistent inflow turbulence generator for LES evaluation of wind-induced responses for tall buildings. *Journal of Wind Engineering and Industrial Aerodynamics*, 142:198–216, 2015.
- [47] C. D. Argyropoulos and N. C. Markatos. Recent advances on the numerical modelling of turbulent flows. *Applied Mathematical Modelling*, 39(2):693–732, 2015.
- [48] B. Basara. PANS method as a computational framework from an industrial perspective. *Notes on Numerical Fluid Mechanics and Multidisciplinary Design*, 130:3–17, 2015.
- [49] Branislav Basara, Sinisa Krajnovic, and Sharath Girimaji. Pans Vs. Les for Computations of the Flow Around a 3D Bluff Body. “7th International ERCOFTAC Symposium on “Engineering Turbulence Modelling and Measurements”, June 4-6, 2008, Limassol, Cyprus., (October 2016), 2008.

- [50] Branislav Basara, Siniša Krajnovic, Sharath Girimaji, and Zoran Pavlovic. Near-Wall Formulation of the Partially Averaged Navier Stokes Turbulence Model. *AIAA Journal*, 49(12):2627–2636, 2011.
- [51] Branislav Basara, Zoran Pavlovic, and Sharath Girimaji. A new approach for the calculation of the cut-off resolution parameter in bridging methods for turbulent flow simulation. *International Journal of Heat and Fluid Flow*, 74(April):76–88, 2018.
- [52] Agerneh K. Dagneu and Girma T. Bitsuamlak. Computational evaluation of wind loads on buildings : a review. *Wind and Structures*, 16(July):629–660, 2013.
- [53] P. A. Durbin. Near-wall turbulence closure modeling without "damping functions". *Theoretical and Computational Fluid Dynamics*, 3(1):1–13, 1991.
- [54] Eurocode. Eurocode 1: Actions on structures -Part 1-4: General actions -Wind actions. *European Committee for Standardization*, 2005.
- [55] J. Franke, C. Hirsch, A. G. Jensen, H.W. Krus, M. Schatzmann, P. S. Westbury Miles, S. D., J. A. Wisse, and N. G. Wright. Recommendations on the Use of CFD in Wind Engineering. *Cost Action C*, (January):1–11, 2004.
- [56] Abdelkader Frendi, Abhijit Tosh, and Sharath Girimaji. Flow Past a Backward-Facing Step: Comparison of PANS, DES and URANS Results with Experiments. *International Journal for Computational Methods in Engineering Science and Mechanics*, 8(1):23–38, 2006.
- [57] Jochen Fröhlich and Dominic von Terzi. Hybrid LES/RANS methods for the simulation of turbulent flows. *Progress in Aerospace Sciences*, 44(5):349–377, 2008.
- [58] M. Germano. Turbulence the filtering approach. *Journal of Fluid Mechanics*, 238(325):325–336, 1992.
- [59] Sharath Girimaji and Khaled Abdol-Hamid. Partially-Averaged Navier Stokes Model for Turbulence: Implementation and Validation. *43rd AIAA Aerospace Sciences Meeting and Exhibit*, (January):1–14, 2005.
- [60] Sharath S. Girimaji. Partially-Averaged Navier-Stokes Model for Turbulence: A Reynolds-Averaged Navier-Stokes to Direct Numerical Simulation Bridging Method. *Journal of Applied Mechanics*, 73(3):413, 2006.

Reference

- [61] K. Hanjalic. Closure Models for Incompressible Turbulent Flows. pages 1–75.
- [62] K. Hanjalic. Will RANS Survive LES? A View of Perspectives. *Journal of Fluids Engineering*, 127(5):831, 2005.
- [63] K. Hanjalić, M. Popovac, and M. Hadžiabdić. A robust near-wall elliptic-relaxation eddy-viscosity turbulence model for CFD. *International Journal of Heat and Fluid Flow*, 25(6):1047–1051, dec 2004.
- [64] S. H. Huang, Q. S. Li, and J. R. Wu. A general inflow turbulence generator for large eddy simulation. *Journal of Wind Engineering and Industrial Aerodynamics*, 98(10-11):600–617, 2010.
- [65] Shenghong Huang, Q. S. Li, and Shengli Xu. Numerical evaluation of wind effects on a tall steel building by CFD. *Journal of Constructional Steel Research*, 63(5):612–627, 2007.
- [66] Stein T. Johansen, Jiongyang Wu, and Wei Shyy. Filter-based unsteady RANS computations. *International Journal of Heat and Fluid Flow*, 25(1):10–21, 2004.
- [67] M. Kato and B.E Launder. The modeling of turbulent flow around stationary and vibrating square cylinders. *Ninth Symposium on Turbulent Shear Flows*, (January 1993):10.4.1–10.4.6, 1993.
- [68] K Suresh Kumar and T Stathopoulos. Fatigue analysis of roof cladding under simulated wind loading. *Journal of Wind Engineering and Industrial Aerodynamics*, 77-78:171–183, 1998.
- [69] Sunil Lakshmi pathy and SS Girimaji. Partially-averaged Navier–Stokes method for turbulent flows: k-omega model implementation. *AIAA paper*, (January):1–15, 2006.
- [70] C. L. Lu, Q. S. Li, S. H. Huang, F. B. Chen, and X. Y. Fu. Large eddy simulation of wind effects on a long-span complex roof structure. *Journal of Wind Engineering and Industrial Aerodynamics*, 100(1):1–18, 2012.
- [71] J M Ma, S. H. Peng, L Davidson, and F J Wang. A low Reynolds number variant of partially-averaged Navier-Stokes model for turbulence. *International Journal of Heat and Fluid Flow*, 32(3):652–669, 2011.

- [72] Guglielmo Minelli, Branislav Basara, and Siniša Krajnovi. Partially-averaged Navier – Stokes simulations of two bluff body flows. *Applied Mathematics and Computation*, 272:692–706, 2016.
- [73] M P Repetto and G Solari. Wind-induced fatigue of structures under neutral and non-neutral atmospheric conditions. *Journal of Wind Engineering and Industrial Aerodynamics*, 95(9-11):1364–1383, 2007.
- [74] M. W. Sarwar, T. Ishihara, K. Shimada, Y. Yamasaki, and T. Ikeda. Prediction of aerodynamic characteristics of a box girder bridge section using the LES turbulence model. *Journal of Wind Engineering and Industrial Aerodynamics*, 96(10-11):1895–1911, 2008.
- [75] Tsan-Hsing Shih, William W Liou, Aamir Shabbir, Zhigang Yang, and Jiang Zhu. A new k-epsilon eddy viscosity model for high reynolds number turbulent flows - model development and validation. *Computers & Fluids*, 24(3):227–238, 1995.
- [76] Chi-su Song and Seung-O Park. Numerical simulation of flow past a square cylinder using Partially-Averaged Navier–Stokes model. *Journal of Wind Engineering and Industrial Aerodynamics*, 97(1):37–47, 2009.
- [77] Philippe R. Spalart. Detached-Eddy Simulation. *Annual Review of Fluid Mechanics*, 41(1):181–202, 2009.
- [78] Speziale G. Analytical methods for the developement of Reynolds stress closures in turbulence. *Annual Review of Fluid Mechanics*, 23(90):107–157, 1991.
- [79] Tetsuro Tamura. Towards practical use of LES in wind engineering. *Journal of Wind Engineering and Industrial Aerodynamics*, 96(10-11):1451–1471, 2008.
- [80] Tetsuro Tamura, Kojiro Nozawa, and Koji Kondo. AIJ guide for numerical prediction of wind loads on buildings. In *2The Fourth International Symposium on Computational Wind Engineering (CWE2006), Yokohama*, pages 161–164, 2006.
- [81] Tetsuro Tamura, Kojiro Nozawa, and Koji Kondo. AIJ guide for numerical prediction of wind loads on buildings. *Journal of Wind Engineering and Industrial Aerodynamics*, 96(10-11):1974–1984, 2008.
- [82] M. Tsuchiya, S. Murakami, A. Mochida, K. Kondo, and Y. Ishida. Development of a new k–epsilon model for flow and pressure fields around bluff body. *Journal of Wind Engineering and Industrial Aerodynamics*, 67-68:169–182, 1997.

Reference

- [83] Shigeru Watanabe and Koichiro Fumoto. Aerodynamic study of slotted box girder using computational fluid dynamics. *Journal of Wind Engineering and Industrial Aerodynamics*, 96(10-11):1885–1894, 2008.
- [84] David C. Wilcox. *Turbulence Modeling for CFD (Third Edition)*. Number 1. 2006.
- [85] Yi Yang, Ming Gu, Suqin Chen, and Xinyang Jin. New inflow boundary conditions for modelling the neutral equilibrium atmospheric boundary layer in computational wind engineering. *Journal of Wind Engineering and Industrial Aerodynamics*, 97(2):88–95, 2009.
- [86] Yue Zhang, Wagdi G. Habashi, and Rooh A. Khurram. Predicting wind-induced vibrations of high-rise buildings using unsteady CFD and modal analysis. *Journal of Wind Engineering and Industrial Aerodynamics*, 136:165–179, 2015.

CHAPTER 3

The problem of wind-induced fatigue

3.1 Wind-induced fatigue

3.1.1 Cycle counting procedure

In recent decades, numerous studies have been conducted to determine a general approach to the calculation of wind-induced load distributions. Two main approaches can be distinguished:

- Time domain procedures, carried out by directly processing deterministic stress time histories obtained from wind simulation [102, 109];
- Frequency domain analytical counting methods, based on the stochastic properties of the response [112, 114].

In general, frequency-domain approaches provide elegant solutions but they are usually applied for simple structures; on the other hand, time-domain approaches provide reliable results on complex structures as well, but require considerable computational efforts. The latter are commonly used as benchmark against which frequency-domain approaches are measured.

Chapter 3. The problem of wind-induced fatigue

Depending on how the cycles are evaluated, in the time or frequency domain, the counting procedures are very different and are discussed in the following paragraphs.

Time domain procedures: the Rainflow Cycle Counting

Several time domain cycle counting methods are present in literature, such as:

- Level Crossing counting;
- Peak Counting;
- Simple Range Counting;
- Rainflow Cycle Counting.

Between them, the latter is the most common and reliable method, so the following describes only this algorithm.

The method was originally proposed by Matsuiski and Endo [99] based on the stress-strain behavior of metallic materials. The procedure can be easily visualized using the description of Lee and Tjhung [110]:

1. Rotate the loading history 90 degrees such that the time axis is vertically downward and the load time history resembles a pagoda roof.
2. Imagine a flow of rain starting at each successive extremum point.
3. Define a loading reversal (half-cycle) by allowing each rainflow to continue to drip down these roofs until:
 - It falls opposite a larger maximum (or smaller minimum) point.
 - It meets a previous flow falling from above.
 - It falls below the roof.
4. Identify each cycle by pairing up the same counted reversals.

The loop closure is rather complex as the loop tips can be formed from points in the signal separated by many intermediate points, particularly in the case of random signal. Therefore, an algorithm is necessary to evaluate it correctly.

A practical implementation of the algorithm can be illustrated according to the ASTM E-1049 - Standard Practices for Cycle Counting in Fatigue Analysis [88]. In the following we denote X as the cycle range under consideration, Y as the previous range adjacent to X , and S as the starting point. The algorithm is further defined:

3.1. Wind-induced fatigue

1. Read next peak or valley. If out of data, go to step 6;
2. If there are less than three points, go to step 1. Form ranges X and Y using the three most recent peaks and valleys that have not been discarded;
3. Compare the absolute values of ranges X and Y :
 - If $X < Y$, go to step 1;
 - If $X \geq Y$, go to step 4;
4. If range Y contains the starting point S , go to step 5; otherwise, count range Y as one cycle, discard the peak and valley of Y , and go to step 2;
5. Count range Y as one-half cycle and discard the first point (peak or valley) in range Y . Move the starting point to the second point in the range Y , and go to Step 2;
6. Count each range that has not been previously counted as one-half cycle.

A sample application of the algorithm provided in [88] is shown in Fig.3.1 and Tab. 3.1.

Chapter 3. The problem of wind-induced fatigue

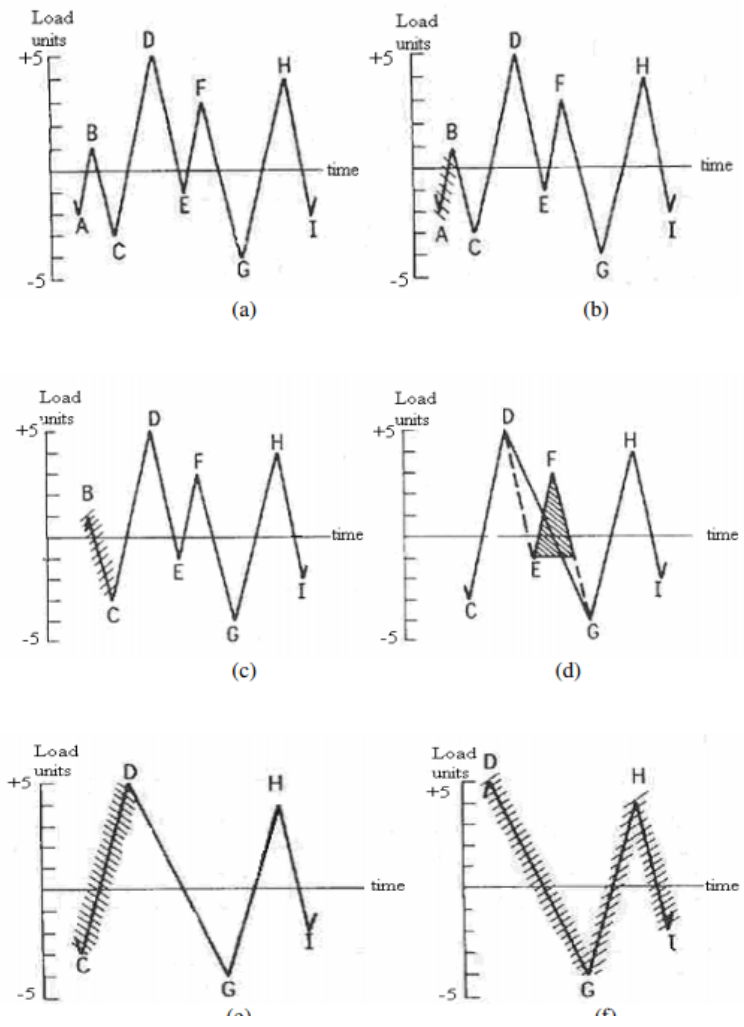


Figure 3.1: Sample application of the Rainflow algorithm [88]

Range	Cycle Counts	Events
10	0	-
9	0	-
8	1	C-D
7	0	-
6	1	H-I
5	0	-
4	1	E-F
3	1	A-B
2	0	-
1	0	-

Table 3.1: Sample application of the Rainflow algorithm [88]

The results of the Rainflow cycle analysis of a signal can be displayed as a stress

3.1. Wind-induced fatigue

cycle density distribution, as shown in Fig. 3.2, left. If integrated from the right hand side, the diagram produces a stress cycle exceedance distribution where the horizontal axis shows the number of cycles that exceed a given range, as shown in Fig. 3.2, right.

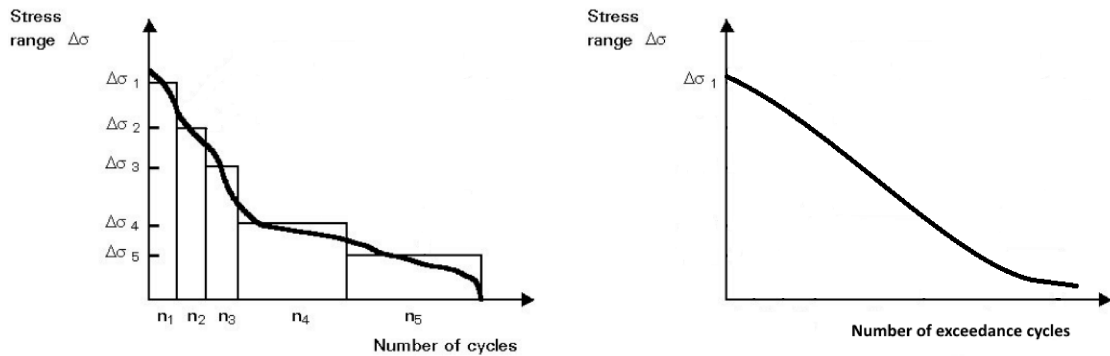


Figure 3.2: *Stress cycle density distribution (left) and stress cycle exceedance distribution (right)*

The cycle range and mean may also be used to form a range-mean histogram of cycle distribution, as shown in Fig. 3.3.

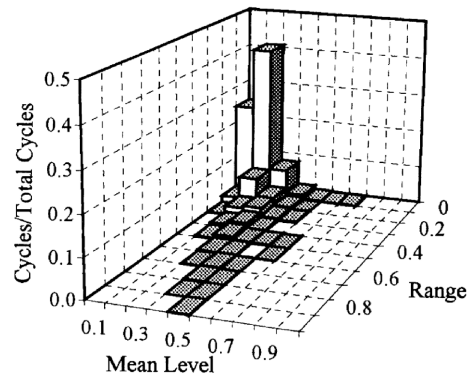


Figure 3.3: *Mean-amplitude stress cycles distribution [109]*

Frequency domain procedures: narrow-band responses

The cycle counting procedures based on the PSD of a stress differentiate whether the response is narrow-band or a broad band signal. Frequency domain methods have origin from Davenport's work [95]. Davenport developed an equation to estimate the expected (mean) peak factor for the largest value of the random response, based on the work of Cartwright and Longuet-Higgins [90], where the response is considered as Gaussian

Chapter 3. The problem of wind-induced fatigue

narrow band random process [94]:

$$g = \sqrt{2 \ln \nu T} + \frac{1}{\sqrt{2 \ln \nu T}} \quad (3.1)$$

where T is the time period in which the extreme value occurs and ν is the cycling rate (mean crossing rate for a Gaussian process) according to Rice [117], derived from the zero-order and second-order spectral moments m_0 and m_2 :

$$\nu = \sqrt{\frac{m_2}{m_0}} \quad (3.2)$$

with $m_k = \int_0^\infty f^k S_{YY}(f) df$. Based on this expression, the extreme value of the stochastic process Y_{max} is predicted as follows:

$$Y_{max} = Y_m + g\sigma_Y \quad (3.3)$$

where Y_m is the average value and σ_Y the standard deviation. The latter can be obtained from the PSD of the process:

$$\sigma_Y = \sqrt{\int_0^\infty S_{YY}(f) df} \quad (3.4)$$

The expected maximum stress amplitude $\Delta\sigma_{max}$ is evaluated by considering Y as the response process of the level of stress at a critical structural detail, and by assuming a symmetric distribution of maxima around the average value:

$$\Delta\sigma_{max} = 2g\sigma_Y \quad (3.5)$$

In narrow band process hypothesis, due to the introduction of Rice equation (Eq. 3.2), the peak distribution is of Rayleigh type [93]:

$$p(Y) = e^{-\left[\frac{Y^2}{2\sigma(Y)^2}\right]} \quad (3.6)$$

For the case that Y is a response process, the probability distribution of the stresses is:

$$p(Y) = e^{-\left[\frac{\Delta\sigma^2}{8\sigma^2}\right]} \quad (3.7)$$

3.1. Wind-induced fatigue

By assuming a power law relation between the standard deviation of the stresses and the mean wind speed of the type:

$$\sigma(V) = A \cdot V^n \quad (3.8)$$

the probability distribution of stress can be written as a function of the mean wind speed V :

$$p_{\Delta\sigma}(V) = e^{-\left[\frac{\Delta\sigma^2}{8A^2V^{2n}}\right]} \quad (3.9)$$

The exponent n has a value of 2 for a quasi-static response of the structure, while it increases up to about 2.5 in case of significant dynamic amplification [105]. The range of power values leads to great uncertainties greatly affecting the estimation of fatigue damage [115], since the latter increase with the exponent n on a power of 3 or 5.

The main advantage of assuming a narrow band process is that the total number of stress cycles at a given stress level during the design life T can be directly linked to the peak distribution as follows:

$$N(\Delta\sigma) = \nu \cdot T \sum_{V=1}^{V_{max}} p_{\Delta\sigma}(V)p(V) = \nu \cdot T \cdot \frac{k}{c^k} \sum_{V=1}^{V_{max}} V^{k-1} \cdot e^{-\left(\frac{V}{c}\right)^k} \cdot e^{-\left[\frac{\Delta\sigma^2}{8A^2V^{2n}}\right]} \quad (3.10)$$

in which the probability of the expected wind speed $p(V)$ is considered of Weibull type. The equation can be easily extended to take the directional effect into account by replacing the distribution of wind speeds with the conditional distribution of probability relative to wind speed in the j – th region:

$$N(\Delta\sigma) = \nu \cdot T \sum_{V=1}^{V_{max}} \sum_j P_j \cdot c_j^b \cdot \frac{k_j}{c_j^{k_j}} \cdot V^{k_j-1} \cdot e^{-\left(\frac{V_j}{c_j}\right)^{k_j}} \cdot e^{-\left[\frac{\Delta\sigma^2}{8A^2V_j^{2n}}\right]} \quad (3.11)$$

where P_j is the probability of occurrence of wind speed from the j – th sector.

Davenport's formulation contains some critical assumptions:

- The assumption of a symmetrical distribution of peaks around the average value and the doubling of the peak factor to estimate the amplitude of stress are not suitable for all structural cases;
- Although for simple structures the wind velocity can be normally distributed, as assumed by peak factor defined by Cartwright and Lounget-Higgins [90], the mechanical response is usually not normally distributed, depending on the structure's mechanical admittance. The non-normality usually substantially increases

Chapter 3. The problem of wind-induced fatigue

the fatigue damage [111];

- The use of the method is limited to narrow band responses, which is the case with low natural frequency lightly damped structures or vibrations induced by vortex-shedding. In general, narrow-band assumption provides an upper-bound value of the fatigue damage.

Frequency domain procedures: wide-band responses

Responses to wind loading typically show a broad range of frequencies, with large background components. Wide-band cycle counting methods follow the approach adopted for narrow-band processes and modify it properly based on the response's PSD properties. A first methodology is proposed in [90], where the peak factor (Eq. 3.1) is modified considering the bandwidth of the response:

$$g = \sqrt{2 \cdot \ln [(1 - \varepsilon^2)^{0.5} \cdot \nu \cdot T]} + \frac{1}{\sqrt{2 \cdot \ln [(1 - \varepsilon^2)^{0.5} \cdot \nu \cdot T]}} \quad (3.12)$$

where ε is the bandwidth factor, representing the ratio of the number of zero-crossing to the number of peaks:

$$\varepsilon = \sqrt{1 - \frac{m_2^2}{m_0 m_4}} \quad (3.13)$$

Compared to the Davenport formulation, this corrected peak factor leads to decreasing value for responses with a bandwidth factor tending to zero. However, the response processes is still assumed to be normally distributed. To overcome the problem, Wirsching and Light [119] proposed to directly modify the fatigue damage D_{nb} evaluated with the narrow-band assumption with same standard deviation σ :

$$D = \lambda D_{nb} \quad (3.14)$$

λ is an empirical parameter defined as:

$$\lambda = a + (1 - a)(a - \varepsilon)^b \quad (3.15)$$

where a and b are functions of the S-N fatigue curve exponent m :

$$a = 0.926 - 0.333m \quad (3.16)$$

3.1. Wind-induced fatigue

This approach evaluates the expected fatigue life by setting the expected damage equal to its failure value in constant amplitude tests, and correcting this value by an empirical bandwidth correction factor λ .

$$b = 1.587m - 2.323 \quad (3.17)$$

$\lambda = 1$ is the special case of narrow-band response, obtained with $\varepsilon = 0$, while the case $\lambda = a$, obtained with $\lambda = 0$ is the case of an uniformly distributed wide-band response and represents a lower-bound in fatigue damage.

While this method has the advantage of being very simple to apply, it may lead to incorrect evaluation of damage compared to the Rainflow Counting. A reliable empirical method to the cycle counting of process with any bandwidth was proposed by Dirlik [96], which proposed an empirical relationship between the PSD of the response and the Rainflow distribution. With Dirlik's approach, the total number of stress cycles at a given stress level during the design life T is equal to:

$$N(\Delta\sigma) = \nu \cdot T \cdot f_D(\Delta\sigma) \quad (3.18)$$

where $\nu = \sqrt{m_4/m_2}$ is the cycling rate, $f_D(\Delta\sigma)$ is the probability density function of the cycle count, obtained as a weighted sum of an exponential distribution and a Rayleigh distribution, which represents the counterpart in the frequency domain of the Rainflow counting procedure. Its expression is the following:

$$f_D(\Delta\sigma) = \frac{\frac{D_1}{Q} e^{-\left(\frac{Z(\Delta\sigma)}{Q}\right)} + \frac{D_2 Z(\Delta\sigma)}{R^2} e^{-\left(\frac{Z(\Delta\sigma)^2}{2R^2}\right)} + D_3 Z(\Delta\sigma) e^{-\left(\frac{Z(\Delta\sigma)^2}{2}\right)}}{2\sqrt{m_0}} \quad (3.19)$$

where:

- $Z = \frac{\Delta\sigma}{2\sqrt{m_0}}$
- $D_1 = \frac{2(x_m - \gamma^2)}{1 + \gamma^2}$
- $D_2 = \frac{1 - \gamma - D_1 + D_1^2}{1 - R}$
- $D_3 = 1 - D_1 - D_2$
- $Q = \frac{1.25(\gamma - D_2 R - D_3)}{D_1}$
- $R = \frac{\gamma - \chi_m - D_1^2}{1 - \gamma - D_1 + D_1^2}$

Chapter 3. The problem of wind-induced fatigue

- $\gamma = \frac{m_2}{\sqrt{m_0 m_4}}$
- $\chi_m = \frac{m_1}{m_0} \sqrt{\frac{m_2}{m_4}}$

The accuracy of the method has been validated analytically by Bishop and Sherratt [89], and later by Kemper and Feldmann [107] by comparing the results to corresponding time domain transient simulations. This method allows also to include the structural geometrical nonlinearity in the analysis.

However, although Dirlik approach can be applied to random stress response with any bandwidth, it still contains some limitations:

- No information on the cycle mean values is extracted, and therefore this approach is best suited to the analysis of welded joints;
- Phase information on the PSD is not evaluated, so it is not possible to correlate the PSDs of two independent principal stresses. Therefore, the method can be applied to uniaxial stresses, or to biaxial stresses provided that the principal stresses are proportional and do not change their orientation during the loading.

In the current European wind standard Eurocode 1 (Part 1-4, Annex B.3) [100], for the determination of the stress-range spectra, a relation between the amplitude of a gust response and the frequency of its occurrence is provided, as shown in Fig. 3.4. Based on the effect due to a 50 years return period wind action S_k , the relation between lower gust effect ΔS and the number of gust cycles N_g in which ΔS is reached or exceeded is given by the a logarithmic polynomial 2nd order:

$$\frac{\Delta\sigma}{S_k}(N_g) = 0.7 (\log^2(N_g) - 17.4 \log(N_g)) + 100 \quad (3.20)$$

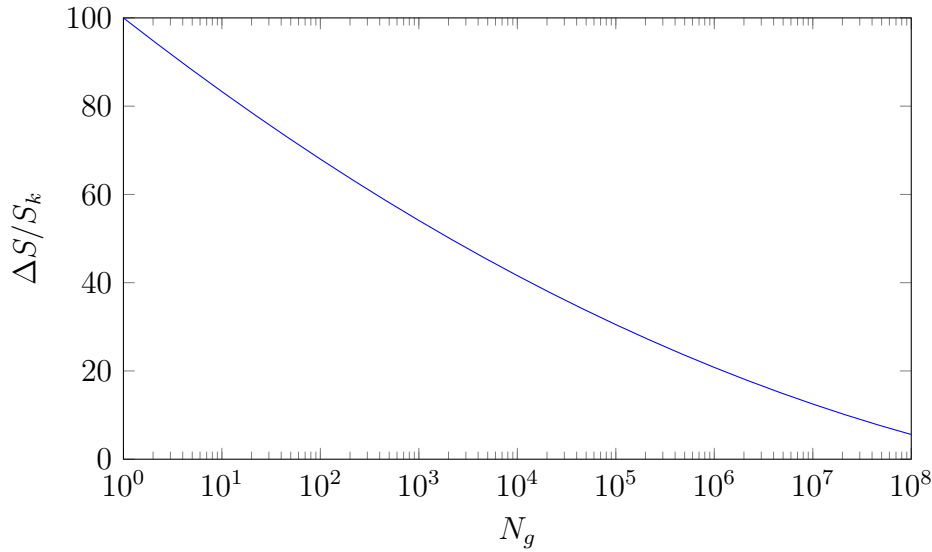


Figure 3.4: Number of gust loads N_g for an effect $\Delta S/S_k$ during a 50 years period

Both the structural dynamic amplification and the individual aerodynamic properties are thereby implied in the characteristic effect S_k . Nevertheless, the frequency of occurrence N_g is independent of all individual characteristics such as the site-dependent wind velocity frequency, the structure's natural frequency and damping behavior. An unconfined use of the Eurocode guideline can therefore lead to an imprecise analysis of wind-induced cycles. A recent sensitivity analysis by Kemper and Holmes [108] described the role of several parameters that influence damage accumulation. The author simulated the loading conditions at each wind speed based on power law relation $\sigma(V) = A \cdot V^n$, and by computed the stress cycles distribution with the use of the Dirlik approach. The first natural frequency f of structure and the shape parameter k of the Weibull curve was found to have much greater influence than both the logarithmic damping decrement δ (especially when the first frequency is lower than 1 Hz) and the scale parameter c . The results are reported in the Fig. 3.5. As expected, the more the Weibull distribution is of Rayleigh type, the larger is the overestimation of the Eurocode formulation.

Chapter 3. The problem of wind-induced fatigue

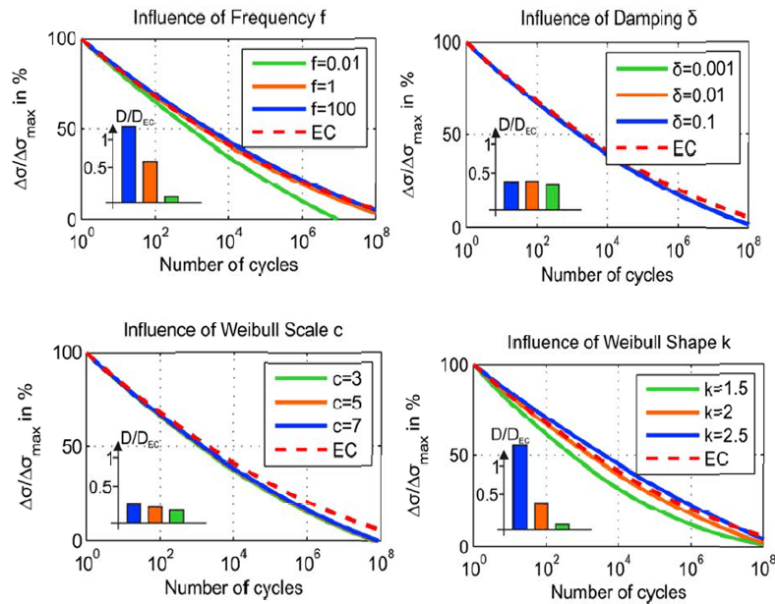


Figure 3.5: Sensitivity of the fatigue damage on the main relevant parameters [108]

In the same study, the directionality effects were evaluated by assuming, respectively, a uniformly, unfavourable and favourable distribution for a certain structural detail. The results, reported in Fig. 3.6, evidence how a consideration of directionality effects can lead to a significant damage reduction with respect to EN 1991-1-4 B.3 formulation.

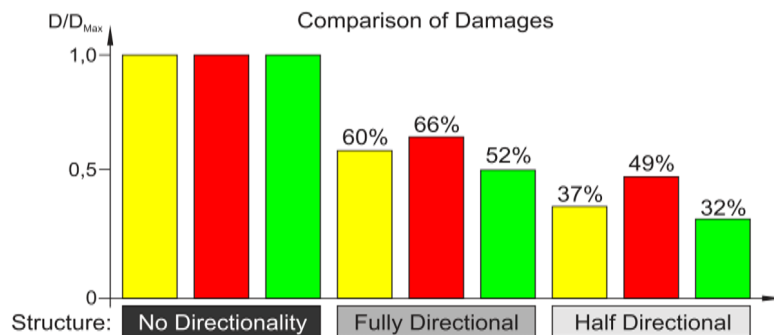


Figure 3.6: Directionality effect on the fatigue damage [108]

Recently, the new CNR DT-207 R1/2018 "Instructions for the evaluation of wind actions and effects on buildings" were released by Italian CNR (Consiglio Nazionale delle Ricerche, National Research Council) [91]. These instructions do not have the status of Standard, however, they represent a document of proven reliability widely used by structural designers for the sizing of structures against the wind. In this last revision, as reported in the introductory chapter, a treatment of the calculation of wind

3.2. Fatigue calculation

induced fatigue has been introduced, based on the research of Repetto and Solari. This advanced method, however, is still subject to the strict hypothesis at its foundation, which limit its applicability in case of complex megastructures (Table 3.2).

Hypotesis	CNR-DT 207 R1/2018	Case of megastructures
Wind loads	Along-wind	Along-wind and Cross-wind
Wind directionality	Does not consider	Needs to consider
Dynamic response	Simple	Complex
Structural response	Linear	Linear or non-linear by geometry
Fatigue evaluation	Nominal stress with global methods	Modified nominal stress with local methods

Table 3.2: Hypothesis of wind-induced fatigue approach in CNR-DT 207 R1/2018 compared to requirements of wind-induced fatigue in megastructures

In general, it is observed that the calculation of wind-induced fatigue in complex structures is a topic which is not entirely covered by Standards and codes, particularly when FE models are involved.

3.2 Fatigue calculation

The section is aimed at a brief review of the commonly used methodology for the assessment of fatigue resistance of welded components, i.e. the nominal stress approach as a method of fatigue assessment and the Palmgren-Miner criterion for estimating fatigue damage. In literature, there are several alternative approaches to the nominal stress method, namely structural hot spot and notch stress method, but the nominal stress method is still the most widely used by major industries and is recommended by numerous national and international codes and standards [87, 103]. Since the research is not focused on investigating the reliability of the methods of fatigue assessment, the alternative methods of fatigue assessment will be only presented briefly.

In modern design offices most of the analysis of steel connections is carried out by means of local finite elements. The topic of how the results of local FEA are related to the nominal stress approach will be discussed in the further sections.

3.2.1 Nominal stress method

Starting with Wohler's studies, the fatigue phenomenon was studied closely using numerous experiments which produced criteria to determine the damage accumulation of structural elements at constant amplitude under cyclic loads. Usually, the results of fatigue tests are expressed as an S-N curve, where S is the amplitude of stress, and N is the number of cycles until failure. For many materials, the S-N curve is well approximated

Chapter 3. The problem of wind-induced fatigue

by a straight line in a log-log scale, or equally with equations in the form:

$$NS^m = K \quad (3.21)$$

where K and m are constants depending on the material, on the structural component and on the level of stress. Eurocode 1993-1-9 [87] incorporates the above approach by providing S-N curves for typical detail categories, as the one shown in Fig. 3.7.

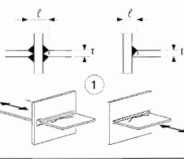
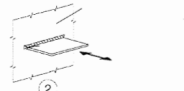

Detail category	Constructional detail		Description	Requirements
80	$t < 50$ mm	all t		1) Inspected and found free from discontinuities and misalignments outside the tolerances of EN 1090. 2) For computing $\Delta\sigma$, use modified nominal stress. 3) In partial penetration joints two fatigue assessments are required. Firstly, root cracking evaluated according to stresses defined in section 5, using category 36* for $\Delta\sigma_r$ and category 80 for $\Delta\sigma_c$. Secondly, toe cracking is evaluated by determining $\Delta\sigma$ in the load-carrying plate.
71	$50 < t \leq 80$	all t		
63	$80 < t \leq 100$	all t		
56	$100 < t \leq 120$	all t		
50	$t > 120$	$r \leq 20$		
45	$200 < t \leq 300$	$r > 30$		
40	$t > 300$	$r > 50$	2) Toe failure from edge of attachment to plate, with stress peaks at weld ends due to local plate deformations.	Details 1) to 3): The misalignment of the load-carrying plates should not exceed 15% of the thickness of the intermediate plate.
As detail 1 in Table 8.5			2) Toe failure from edge of attachment to plate, with stress peaks at weld ends due to local plate deformations.	
36*			3) Root failure in partial penetration Tee-but joints or fillet welded joint and in Tee-but weld, according to Figure 4.6 in EN 1993-1-8:2005.	

Figure 3.7: Example of fatigue details according to the Eurocode 1-9

The S-N curves are based on constant amplitude nominal stress, i.e. the elastic stress calculated in the sectional area under consideration disregarding the local stress-raising effects of the welded joint, but including the component's geometric shape near the joint. Each fatigue detail is associated to a different reference value of fatigue strength $\Delta\sigma_c$ and $\Delta\tau_c$ at 2 millions of cycles. For constant amplitude nominal stress ranges, Eurocode provides the well-known following expressions for the fatigue strength:

$$\Delta\sigma_R^3 N_R = \Delta\sigma_c^3 \cdot 2 \cdot 10^6 \quad N \leq 5 \cdot 10^6 \quad (3.22)$$

$$\Delta\tau_R^5 N = \Delta\tau_c^5 \cdot 2 \cdot 10^6 \quad N \leq 5 \cdot 10^6 \quad (3.23)$$

The constant amplitude fatigue limit is defined as:

$$\Delta\sigma_D = 0.737\Delta\sigma_c \quad (3.24)$$

When stress ranges are above and below the constant amplitude fatigue limit $\Delta\sigma_D$, the fatigue strength is based on the extended fatigue strength curves as follows:

$$\Delta\sigma_R^m N_r = \Delta\sigma_D^m \cdot 5 \cdot 10^6 \quad m = 5 \quad \text{for} \quad 5 \times 10^6 \leq N \leq 10^8 \quad (3.25)$$

3.2. Fatigue calculation

Eurocode introduces a cut-off limit, below which cycles do not generate any damage:

$$\Delta\sigma_L = 0.549\Delta\sigma_D \quad (3.26)$$

$$\Delta\tau_L = 0.457\Delta\tau_c \quad (3.27)$$

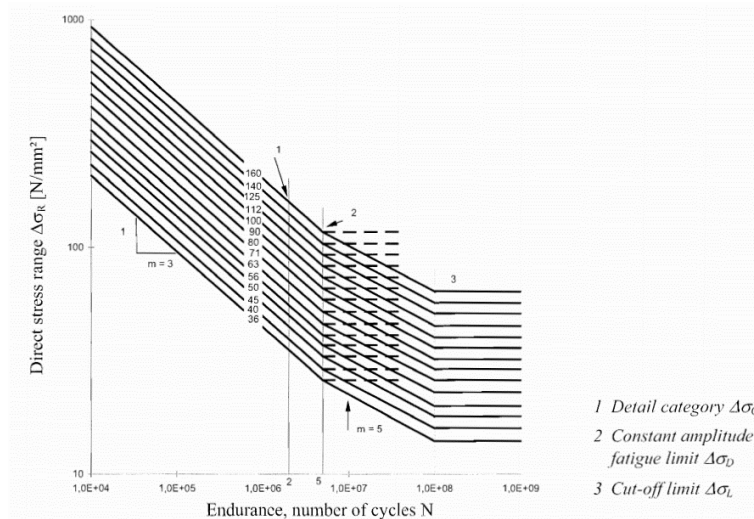


Figure 3.8: Fatigue strength curves for direct stress ranges according to the Eurocode 1-9

Not all the specific fatigue data for a structural detail, such as its size, shape and quality, are covered by the fatigue curves provided by the Eurocode. Consequently, a reduction of information that might give rise to a scatter in the results coming from the application of the nominal stress method can emerge [104]. The new recommendations of the IIW (International Institute of Welding) [106] provides a more exhaustive classification of fatigue details, with 81 structural details that include all the following effects:

- structural hot spot stress concentrations due to the detail;
- local stress concentrations due to the weld geometry;
- weld imperfections consistent with normal fabrication standards;
- direction of loading;
- metallurgical conditions;
- welding process;

Chapter 3. The problem of wind-induced fatigue

- inspection procedure (if specified);
- post weld treatment (if specified).

The individual structural details are inserted in S-N curves slightly modified compared to those provided by the Eurocode. The knee point for direct stress ranges has been raised from 5×10^6 to 10^7 . Supported by recent experimental data, which indicate the absence of an effective fatigue limit, the fatigue limit is substituted by a curve with a slope $m = 22$ for both direct and shear stresses (Fig. 3.9). This difference from the Eurocode can become relevant for the case of wind actions because of the high number of cycles associated to low-intensity wind actions.

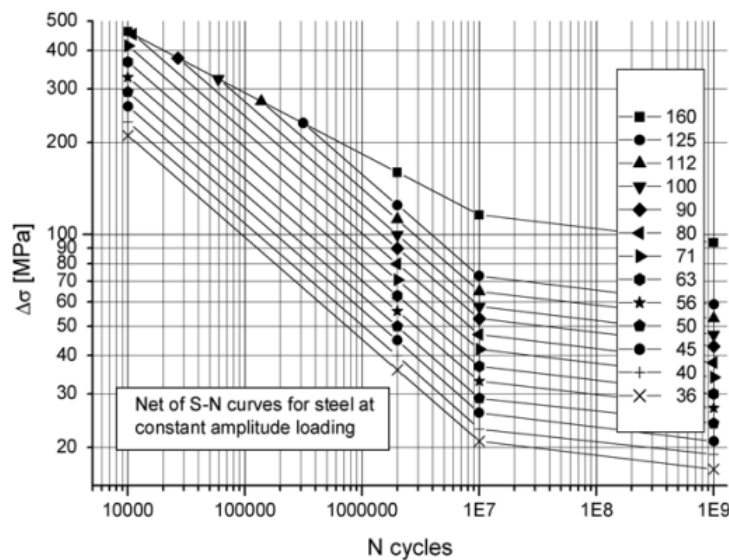


Figure 3.9: Fatigue strength curves for direct stress ranges according to the IIW

It is necessary to underline that most of the real loading condition are not related to zero mean stress ranges. For base material, signal with tensile mean stress is recognized as generating a fatigue life as shorter as the tensile mean stress is higher; on the contrary, compressive mean stress results in increased fatigue life. Several methods for applying fatigue S-N curves obtained at zero mean stress to cycles with nominal tensile mean stress have been proposed. This typically reduce the strength of fatigue relative to the ratio between the average σ_m tensile stress and the ultimate tensile stress σ_u :

$$\frac{\Delta\sigma_L}{\Delta\sigma_{L0}} + \left(\frac{\sigma_m}{\sigma_u}\right)^k = 1 \quad (3.28)$$

where $\Delta\sigma_{L0}$ is the fatigue strength for a non-zero mean stress. In the case of $k = 1$

(modified Goodman relation) and $k = 2$ (Gerber relation), the relationship is respectively linear and hyperbolic. Most fatigue test results fall between the Goodman and Gerber curves. These relationships can also be applied to the compressive mean pressure zone, but their beneficial effect is often neglected.

3.2.2 Modified nominal stress

While the nominal stress method covers a wide range of applicability, in case of complex stress states and/or structural details not included in the codes classification it is still not accurate. In these cases, other fatigue assessment procedures than the nominal stress need to be employed (modified nominal stress methods).

In Colussi's work [92], a local approach based on SED theory was presented to improve the classical nominal stress approach for welded structures. This approach was specifically developed with the purpose of its application for the calculation of fatigue of welded joints of megastructures by means of a finite element analysis. The context, in this case, is fundamental because the solution of complex problems, such as fatigue, requires an approach that takes into account the problem of massiveness generated by the large quantities and complexities typical of these structures. The method presented in [92] allows, for this reason, the use of calculation grids with coarse and unstructured plate elements. The concepts underlying this approach are described below.

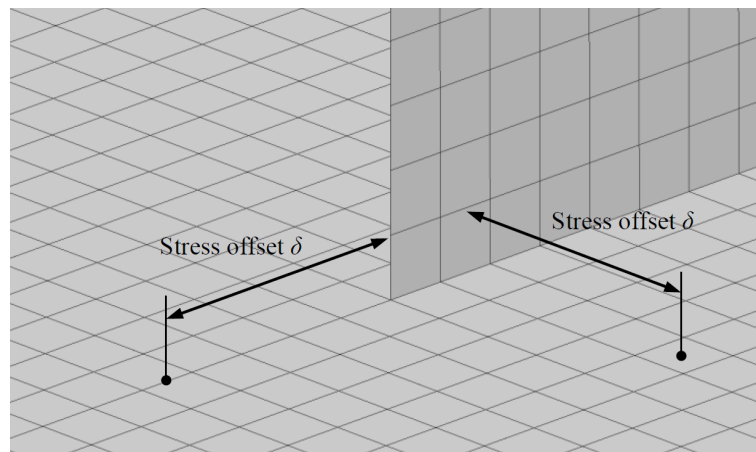


Figure 3.10: Example of shell finite element mesh and stress offsets to compute “local” nominal stress components. [92]

Once the nominal stress is retrieved at an offset $\delta = 1.5$ times the plate thickness (Fig. 3.10), as suggested by the DVS technical code [98], it needs to be corrected to take into consideration the bending effect. The approach introduces a correction in the nominal stresses at the toe of the weld $\sigma_{n,toe}$ and at the root computed from

Chapter 3. The problem of wind-induced fatigue

the coarse shell FE model by introducing two nominal stress correctors $k_{b,toe}(r_b)$ and $k_{b,root}(r_b)$. The correction leads to the modified nominal stress for weld toe and weld root assessment:

$$\sigma_{n,toe} = \frac{\sigma_n}{k_{b,toe}(r_b)} \quad (3.29)$$

$$\sigma_{n,root} = \frac{\sigma_n}{k_{b,root}(r_b)} \quad (3.30)$$

The correction allows to take into account the fact that welded joints have different fatigue strength properties under tensile and pure bending loads. r_b is the bending ratio, defined as:

$$r_b = \frac{|\Delta\sigma_b + \delta \cdot \frac{6}{t} \cdot \Delta\tau_{av}|}{|\Delta\sigma_m| + |\Delta\sigma_b + \delta \cdot \frac{6}{t} \cdot \Delta\tau_{av}|} \quad (3.31)$$

where the stress and geometric components are defined as in Fig. 3.11.

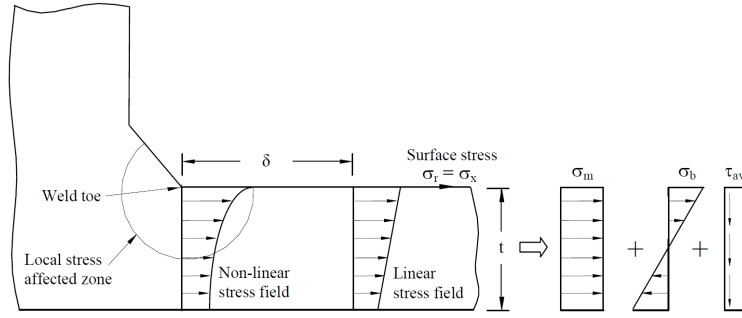


Figure 3.11: Stress fields near a weld toe under linear elastic hypothesis [92]

The correction for considering the bending ratio effect can be expressed by means of the ratio of the w_1 and w_{eq} parameters, which are the non-dimensional parameters representative of the local stress concentrating capacity of a weld geometry.

If the reference detail has been tested under pure membrane condition, two correcting coefficients are respectively defined as:

$$k_{b,toe}(r_b) = \frac{w_{1,m}}{w_1(r_b)} \quad (3.32)$$

$$k_{b,root}(r_b) = \frac{w_{eq,m}}{w_{eq}(r_b)} \quad (3.33)$$

If the reference detail has been tested under pure bending condition, the coefficients are defined as:

$$k_{b,toe}(r_b) = \frac{w_{1,b}}{w_1(r_b)} \quad (3.34)$$

3.2. Fatigue calculation

$$k_{b,root}(r_b) = \frac{w_{eq,b}}{w_{eq}(r_b)} \quad (3.35)$$

One of the major advantages of this approach is that the definition of parameters w_1 and w_{eq} can be parametrized in order to take into account the bending ratio effect on fatigue strength for any type of joint. A series of fitting equations has thus been provided in [92] to calculate their values for the following types of joints:

- load-carrying joints;
- non-load carrying joints;
- cruciform joints;
- T-joints;
- double-fillet joints;
- full-penetrated joints.

3.2.3 Estimation of the fatigue damage

Wind loading on a structure does not produce a constant amplitude loading like those considered for material testing in laboratories experiments. In the general situation of a variable loading, the effects of all stress range occurrences during the service life of the structure accumulate over time, leading to the fatigue damage D . This is the ratio between the number of cycles n at a particular stress amplitude $\Delta\sigma$ and the number of cycles to failure N at the same stress amplitude:

$$D = \frac{n}{N} \quad (3.36)$$

Therefore the fatigue failure occurs when $D = D_{max}$ where D_{max} is the maximum damage, usually equal to 1.

A stress load history can always be decomposed in several blocks of constant amplitude stress $\Delta\sigma_i$, as shown in the Fig. 3.12, each associated to its number of occurrence n_i .

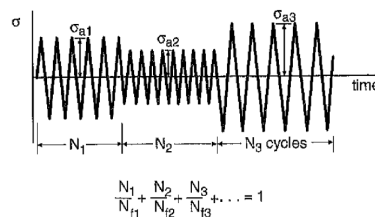


Figure 3.12: Example of block loading with three stress amplitudes [97]

Chapter 3. The problem of wind-induced fatigue

The prediction of the fatigue life is usually performed with the use of the Palmgren-Miner criterion. This allow to evaluate the cumulated damage D as:

$$D = \sum \frac{n_i}{N_i} \quad (3.37)$$

Therefore, when the sum of the fractional damage $\frac{n_i}{N_i}$ for all stress levels reaches D_{max} , the crack initiation is expected.

The evaluation of the wind-induced fatigue damage accumulation requires the knowledge of the stress-cycle historigram as well as the knowledge of the wind climate at the building site. The macro- and micro-meteorological components, which are associated to the mean wind speed an turbulence, relatively, are treated independently to one another. The concept of this superposition is called *state-approach* [116] and is represented in Fig. 3.13.

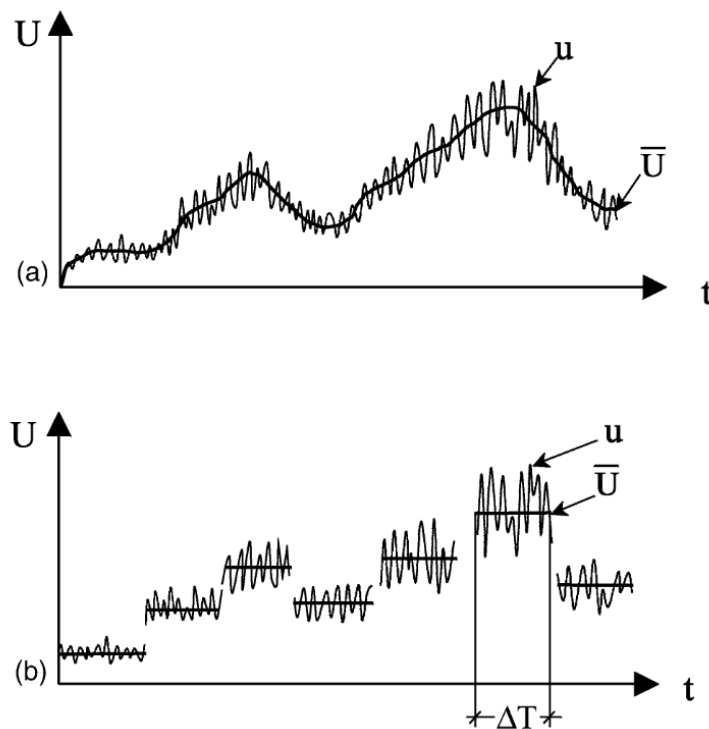


Figure 3.13: Temporal representation of wind velocity: (a) real; (b) simplified [116]

The cumulative damage principle is consistent with the assumption that the damage increases linearly with time when the stress is a stationary stochastic process i.e. the damage in any cycle is only a function of the stress in that cycle, with no constraint on the order in which the different stress amplitudes are applied. While many nonlinear rules on accumulated fatigue damage have been proposed to address the simplification

3.2. Fatigue calculation

of a linear expectation of damage the Palmgren-Miner criterion remains the most commonly used method to predicting fatigue life and, in fact, it is the approach suggested by the Eurocode. In particular, the fatigue check has the following expression:

$$\sum \frac{n_i(\gamma_{Ff}\Delta\sigma_i)}{N_i \frac{\Delta\sigma_c}{\gamma_{Mf}}} < \frac{1}{\gamma_D} \quad (3.38)$$

Where:

- γ_{Ff} is the partial factor that deals with the uncertainties in the load and response model;
- γ_{Mf} is the partial factor that deals with the uncertainties in the material model;
- γ_D is the partial factor that deals with the uncertainties in the fatigue resistance data and fatigue damage accumulation rule.

The level of partial factors depends on the consequence of failure and relative cost of safety measures, and on the uncertainties and sensitivities of all the random variables involved in the fatigue assessment (including uncertainty due to inadequate knowledge). Using reliability approaches, a systematic method to calibrating partial factors can be employed, allowing the risk of failure to be reduced to a target value. In industrial practice, generally, the partial safety coefficients are used which already intrinsically contain the choice of the reliability level. For the partial factor γ_{Mf} , Eurocode provides the values in Fig. 3.14:

Assessment method	Consequence of failure	
	Low consequence	High consequence
Damage tolerant	1,00	1,15
Safe life	1,15	1,35

Figure 3.14: Recommended values of the Eurocode 1-9 for the partial factor γ_{Mf}

The Eurocode provides a comprehensive design strategy for the determination of partial safety factors, which depends, mainly, of the consequence level of the failure and on the inspectability of the part. Two design approaches can be adopted alternatively, or together in different parts of the structures, namely safe-life or damage tolerant assessment methods.

- The damage-tolerant method, as the name suggests, integrates the fatigue design of the structural element with regular inspection and maintenance, thus accepting the local formation of cracks whereas they will be readily detected before they

Chapter 3. The problem of wind-induced fatigue

become critical and corrective action can be taken. A damage tolerant method requires details associated to low rate of crack propagation, redundancy, the presence of crack-arresting details and inspectability of the details.

- The safe-life approach is used in situations when no regular in-service inspection can be performed, and local formation of cracks in one component could rapidly lead to the failure of the structural element or the structure; consequently, a higher survival probability is required, and a higher value of safety factor is addressed compared to the damage-tolerant method.

The difference between the two approaches is clearly described in Fig. 3.15 from ECCS's Eurocode Design Manual "Fatigue Design of Steel and Composite Structures" [113].

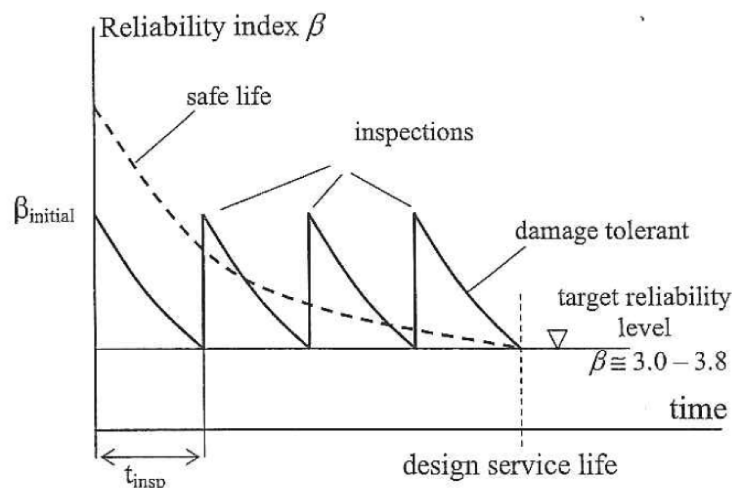


Figure 3.15: Schematic of fatigue reliability assuming damage tolerant and safe life methods and a failure with high consequence [113]

On the classification of the EN1990:2002 (Annex B) [101], megastructures like stadium roofs are usually associated to high consequence of failure (consequence class CC3) due to the necessity to reduce the vulnerability of people and environment to an acceptable residual risk. However, the choice of these approaches could be combined within the same structure. Consider the case of the car: some parts, such as the chassis, are never subject to inspection and replacement during its lifetime, as the manufacturer expects their fatigue life to be much longer than the service period, as it is impossible to detect any cracks when they emerge and as the consequences of a failure of the chassis are unacceptable. On the other hand, other parts are periodically inspected and maintained to ensure that no replacement is required. In a megastructure composed by

an extreme high quantity of fatigue-prone details, not all failures would have the same effect, for example, some parts that can be easily inspected could be designed according to the damage tolerant approach, while other inaccessible or highly important structural parts could be designed using the safe life approach.

It is also important to point out that for steel megastructures and, in general, in civil engineering field, the damage calculation is generally carried out conservatively, by considering a damage $D = 1$ as the moment of the crack initiation, in accordance with the principles of the nominal stress method proposed by the Eurocode [87]. The duration of the propagation phase is neglected, as it would require in-depth analysis with respect to the structural detail adopted and, often represents only a fraction of the number of cycles required to open the crack.

The fact of considering as the fatigue lifetime of the structure the time within which no crack has yet been initiated, makes it admissible to consider that the structure maintains the same structural behavior during its life. This hypothesis has a limit, however, when we consider the possibility of extreme events in the course of life, such as an earthquake or an exceptional wind event, that should bring it into the plastic field changing the response. However, there is no way, at present, to consider a temporal history of events in such a deterministic a-priori approach.

3.3 Reference

- [87] *EN 1993-1-9 Eurocode 3: Design of steel structures - Part 1-9: Fatigue*. European Committee for Standardization, Brussels, 2005.
- [88] ASTM. E1049-85: Standard practices for cycle counting in fatigue analysis. *Annual Book of ASTM Standards West Conshohocken, PA*, 2011.
- [89] N. W.M. Bishop and Frank Sherratt. A Theoretical Solution for the Estimation of "Rainflow" Ranges from Power Spectral Density Data. *Fatigue & Fracture of Engineering Materials & Structures*, 1990.
- [90] D. E. Cartwright and M. S. Longuet-Higgins. The Statistical Distribution of the Maxima of a Random Function. *Proceedings of the Royal Society A: Mathematical, Physical and Engineering Sciences*, 1956.
- [91] CNR. CNR DT 207 R1/2018 Istruzioni per la valutazione delle azioni e degli effetti del vento sulle costruzioni, 2018.

Reference

- [92] Marco Colussi. *Massive Fatigue Assessment of Welded Megastructures by Advanced Methods*. Ph.d. thesis, University of Padua, 2017.
- [93] S.H Crandall and W.D. Mark. *Random Vibrattion in Mechanical Systems*. 1963.
- [94] A. G. Davenport. Note on the distribution of the largest value of a random function with application to gust loading. *Proceedings of the Institution of Civil Engineers*, 1964.
- [95] A. G. Davenport. The Estimation of Load Repetitions on Structures with Application to Wind Induced Fatigue and Overload. In *RILEM International Symposium*, 1966.
- [96] T. Dirlik. Application of computers to fatigue analysis. *Ph.D. thesis, Warwick University, Warwick*, 1985.
- [97] N.E. Dowling. *Mechanical Behavior of Materials: Engineering Methods for Deformation, Fracture, and Fatigue*. Pearson Prentice Hall, 2007.
- [98] DVS. DVS 1612 - Design and endurance strength assessment of welded joints with steels in rail vehicle construction. 49(August), 2009.
- [99] T. et al Endo. Damage Evaluation of Metals for Random of varying loading. *The Society of material Science, Proc 1974*, 1974.
- [100] Eurocode. Eurocode 1: Actions on structures -Part 1-4: General actions -Wind actions. *European Committee for Standardization*, 2005.
- [101] European Standard. BS EN 1990:2002+A1:2005: Eurocode - Basis of structural design. 2005.
- [102] O. Flamand, J. Bietry, C. Barre, E. Germain, and P. Bourcier. Fatigue calculation on the roof sustaining cables of a large stadium in Paris. *Journal of Wind Engineering and Industrial Aerodynamics*, 64(2-3):127–134, 1996.
- [103] A. F. Hobbacher. *Recommendations for Fatigue Design of Welded Joints and Components*. 2016.
- [104] Adolf F. Hobbacher. New developments at the recent update of the IIW recommendations for fatigue of welded joints and components. *Steel Construction*, 3(4):231–242, 2010.

- [105] John D Holmes. *Wind Loading of Structures*. CRC Press, Taylor & Francis Group, 2015.
- [106] Bertil Jonsson, Gerd Dobmann, Adolf Hobbacher, M Kassner, and Gary Marquis. *IIW guidelines on weld quality in relationship to fatigue strength*. 2016.
- [107] Frank H. Kemper and Markus Feldmann. Fatigue life prognosis for structural elements under stochastic wind loading based on Spectral Methods, Part II: Non-linear Structures. *Proceedings of the 8th International Conference on Structural Dynamics, EURO DYN 2011*, (June):1636–1643, 2011.
- [108] Frank H Kemper and John D Holmes. Gust-induced fatigue cycle counts - sensitivity to dynamic response, wind climate and direction. *Advances in Civil Environmental and Materials Research*, 2014.
- [109] K Suresh Kumar and T Stathopoulos. Fatigue analysis of roof cladding under simulated wind loading. *Journal of Wind Engineering and Industrial Aerodynamics*, 77-78:171–183, 1998.
- [110] Yung-Li Lee and Tana Tjhung. Chapter 3 - Rainflow Cycle Counting Techniques. In Yung-Li Lee, Mark E Barkey, and Hong-Tae Kang, editors, *Metal Fatigue Analysis Handbook*, pages 89–114. Butterworth-Heinemann, Boston, 2012.
- [111] Loren D. Lutes, Miguel Corazao, Sau Lon James Hu, and James Zimmerman. Stochastic fatigue damage accumulation. *Journal of Structural Engineering (United States)*, 110(11):2585–2601, 1984.
- [112] M. A. Mikitarenko and A. V. Perelmuter. Safe fatigue life of steel towers under the action of wind vibrations. *Journal of Wind Engineering and Industrial Aerodynamics*, 1998.
- [113] Alain Nussbaumer, Luis Borges, and Laurence Davaine. *Fatigue design of steel and composite structures: Eurocode 3: Design of steel structures, part 1-9 fatigue; Eurocode 4: Design of composite steel and concrete structures*. John Wiley & Sons, 2012.
- [114] Albert A. Petrov. Dynamic response and life prediction of steel structures under wind loading. *Journal of Wind Engineering and Industrial Aerodynamics*, 74-76:1057–1065, 1998.

Reference

- [115] Maria Pia Repetto and Giovanni Solari. Closed form solution of the alongwind-induced fatigue damage to structures. *Engineering Structures*, 2009.
- [116] Maria Pia Repetto and Alessio Torrielli. Long term simulation of wind-induced fatigue loadings. *Engineering Structures*, 132:551–561, 2017.
- [117] S. O. Rice. Mathematical Analysis of Random Noise. *Bell System Technical Journal*, 1945.
- [118] Waloddi Weibull. A Statistical Distribution Function of Wide Applicability. *Journal of Applied Mechanics*, pages 293–297, 1951.
- [119] P. H. Wirsching. Fatigue under wide band random stresses. *Journal of Structural Division ASCE*, 1980.

CHAPTER 4

Simulation-based approach for wind-induced fatigue calculation of megastructures

4.1 Complete procedure

An original procedure for the calculation of wind-induced fatigue is here proposed. The procedure is defined to be "simulation-based" since all the steps involve simulation in order to accurately describe the considered phenomena, thus permitting the maximum flexibility on the structural type, or the response type or the type of wind excitation. A key aspect of the procedure is that, at the end, a detailed fatigue calculation is performed using local approaches on every structural detail, enabling a detailed fatigue design of the component and, eventually, of all the structure. This approach is in fact intended to provide the engineer with a comprehensive design tool that allows him to design a megastructure with respect to the fatigue induced by wind down to the highest level of detail, but also giving him the opportunity to develop an understanding of the phenomenon of wind that generates it.

The main blocks are:

Chapter 4. Simulation-based approach for wind-induced fatigue calculation of megastructures

1. Simulation of wind loading: for each independent loading condition, a transient wind loading simulation must be performed both using wind tunnel tests, computational fluid dynamics simulation, or a combination of the two approaches.
2. Global modal analysis: the time histories of pressures measured from the wind simulation are applied to a global FE model and time histories of displacements at all nodes are computed.
3. Statistical analysis of wind data: the fatigue cycles measured during the test are projected to the lifetime of the structure using Weibull distribution of climatic data;
4. Cycle counting: because of the complexity of the structural joints of large roof steel structures, a method that combine global and local response is proposed. This allows computing the stress time history acting on a detail for each loading condition introducing the concept of *Virtual Strain Gauge*. Stress time histories are then processed using the Rainflow counting method;
5. Loading of local models: the stress cycle distributions, measured on all Virtual Strain Gauges, are discretized into blocks, each of which is represented by a deformation state of the connection. These deformative states are thus applied as a boundary condition of a local shell model, defining the fatigue spectrum of the connection.
6. Local fatigue calculation: the calculation of fatigue damage is performed using a local shell FE model adopting *Modified Nominal Stress* approach which implements Strain Energy Density (SED) method to correct the calculated stress.

The workflow for the procedure is further highlighted in Fig. 4.1.

4.2. Wind simulation

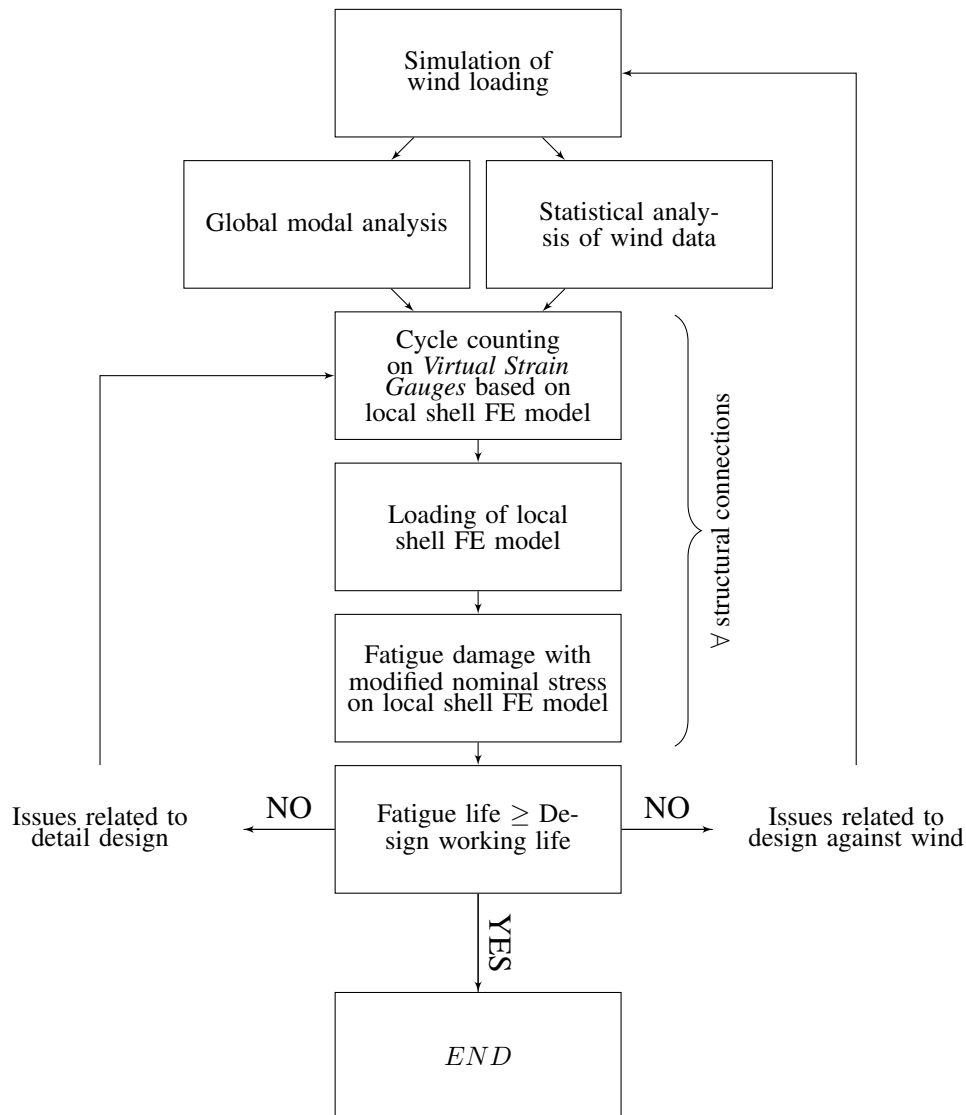


Figure 4.1: Wind-induced fatigue calculation

4.2 Wind simulation

As shown in section 2, the simulation of the wind loading for megastructures be only performed in a deterministic environment with the use of Wind Tunnel Tests or by performing a CFD simulation. Due to the complexity of the fluid-dynamic problem, this part of the procedure is currently impossible to standardize and it is highly dependent on the experience of the simulation engineer and on the available equipment and resources. Some macroscopic blocks, which are common to the all wind simulations, can still be identified and are shown in Fig. 4.2.

Chapter 4. Simulation-based approach for wind-induced fatigue calculation of megastructures

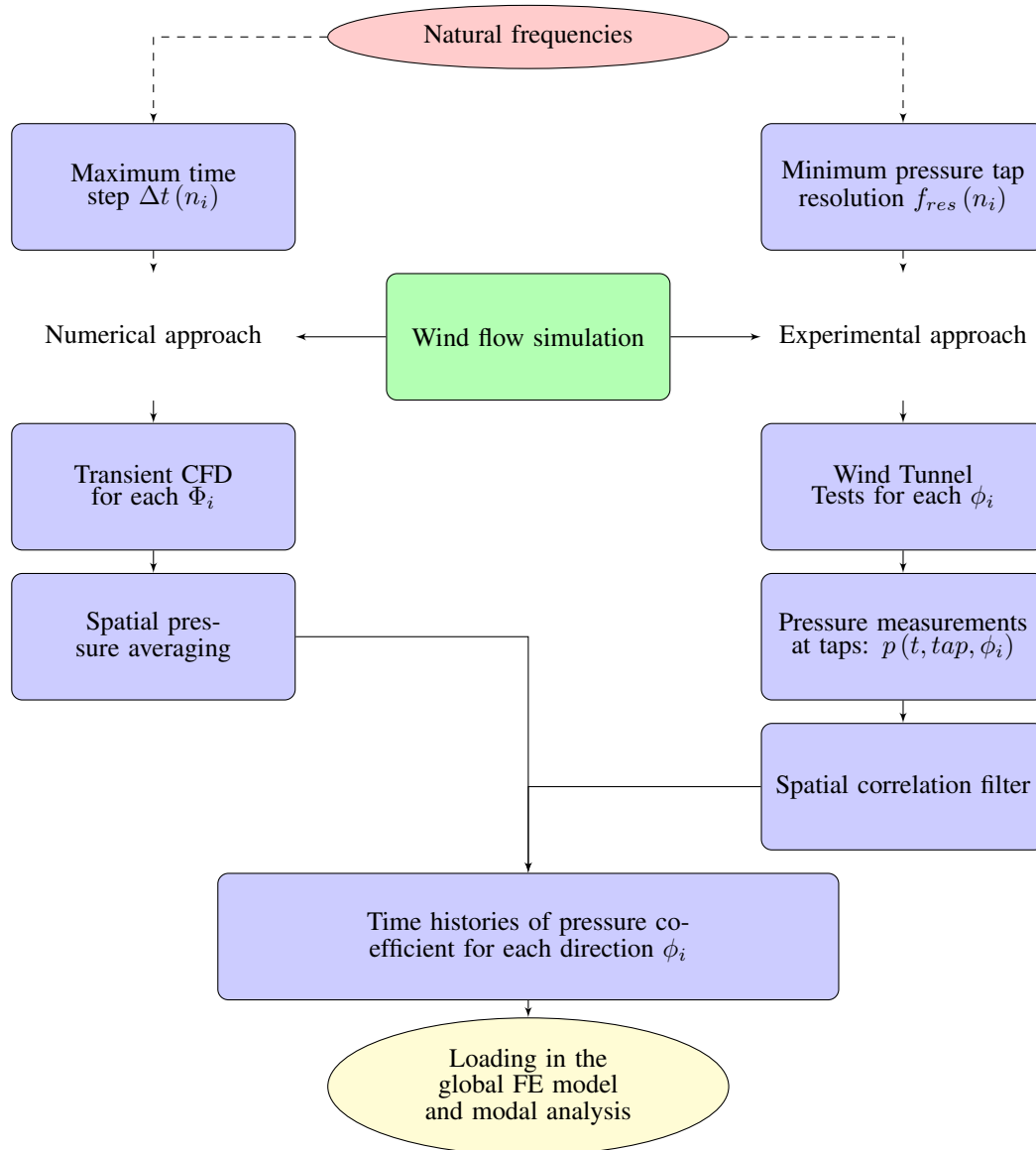


Figure 4.2: Wind simulation flow chart

This block produces as an output the time histories of the pressure coefficients along the whole surface of the structure for all relevant wind conditions. The loads are fragmented into "load areas" which must be sufficiently small to reproduce the spatial distribution of the load. In case of a CFD study, the values of pressure on the load areas are directly obtained by spatial averaging of the pressure in all the finite-volume faces over each load area, while a preliminary filtering process is required in the case of WTTs.

Wind tunnel tests produce as an output the recorded time histories of pressure coefficients $C_{pkj}(t)$ for each pressure tap k and direction j with a time step $\Delta_{tm} = 1/f_{res}$, where f_{res} is the frequency of data acquisition. For the sake of simplicity, the same sub-

4.2. Wind simulation

script j has been used for the representation of the statistical directional sectors and the simulating directions. The scaling of the pressure coefficient and of the corresponding time steps depends on the simulated wind speed V at the building reference height; by considering first the design wind speed V_d , the time history of the pressure associated to the direction j and acting on the tributary area, measured by the $k - th$ pressure tap is:

$$p_{jk,V_d}(t) = Cp_{jk}(t) \left(\frac{1}{2} \rho V_d^2 \right) \quad (4.1)$$

$Cp_{jk}(t)$ is the pressure coefficient where:

- i is the velocity level index;
- j is the index of wind direction Φ ;
- k is the grid position.

The corresponding time step is:

$$\Delta t_{V_d} = \Delta t_m \frac{\lambda_L}{\lambda_{V_d}} \quad (4.2)$$

where λ_L and λ_{V_d} are, respectively, the length scale and the velocity scale.

The pressure coefficient leads to the calculation of pressure for each grid position. By considering a generic mean wind speed V_i , under the hypothesis of no Reynolds number effects, the scaling becomes:

$$p_{ijk}(t) = Cp_{jk}(t) \left(\frac{1}{2} \rho V_i^2 \right) \quad (4.3)$$

where $p_{ijk}(t)$ is the pressure at position k , for block j and velocity i and $\Delta t_{vi} = \Delta t_m \frac{\lambda_L}{\lambda_{vi}}$ is the time step at prototype scale associated with $i - th$ velocity, where Δt_m is the time step of the model, λ_L is the geometric scale and λ_v is the velocity scale.

$$\Delta t_{V_i} = \Delta t_m \frac{\lambda_L}{\lambda_{V_i}} = \frac{\Delta t_{V_d}}{\alpha} \quad (4.4)$$

where $\alpha = V_i/V_d (< 1)$. From a physical point of view, starting from the pressure time histories at the design wind speed, as the wind speed becomes lower (and so α decreases), the intensity and the frequency of the fluctuating pressure reduces, respectively, quadratically and linearly with α .

Chapter 4. Simulation-based approach for wind-induced fatigue calculation of megastructures

The raw pressure time history interpolated over the $k - th$ tributary area from the measures of the pressure taps nearby still contains high frequency energy content that it is not representative of the whole loading area. A filtering process that takes into account the non-full spatial coherence of the pressure fluctuations must therefore be performed. The filtering process is very sensitive to the frequency content acquired by the pressure taps. As mean velocity is scaled down to lower values, the signal is stretched in time and reduces in magnitude. Higher frequency components, which have negligible effects at high velocities, become relevant as they start interacting with lower structural modes. Since pressure taps have a limited frequency sensitivity, it must be assured that they are able to provide sufficient spectral content even at higher frequencies and thus, high-resolution pressure taps should be employed for this type of studies.

4.3 Modal analysis

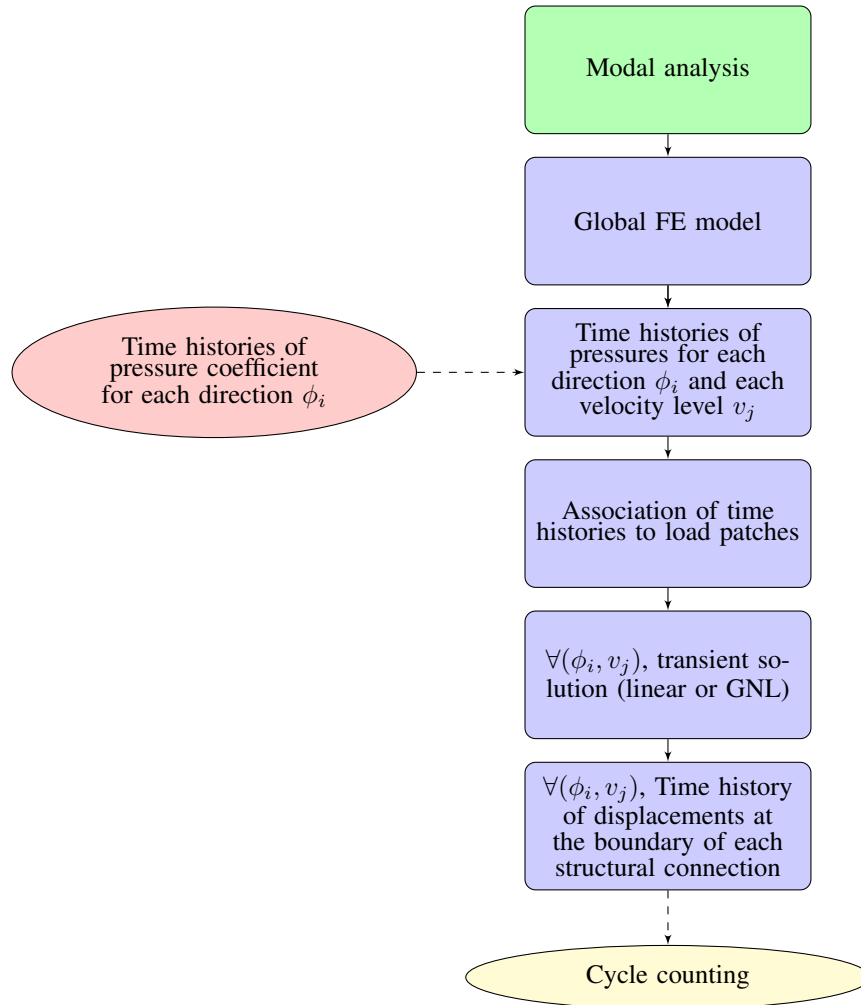


Figure 4.3: *Modal analysis*

The set of pressures acting on the roof surface has then to be transferred to the structural frame. As a simple approach to transfer the forces applied on surfaces to the structural frame, loads on surfaces can be transferred as linearly distributed forces in the beams by area weighting. This methodology is usually implemented in most of the commercial softwares; as an example, the software Straus7 provides this tool by defining a plate element with no stiffness and mass, called *Load Patch*. To use this approach, the layout of the tributary areas must be conveniently arranged such that the load areas edges match with the beams of the FE model of the structural frame.

The relation between the pressures acting on the roof surface and the distributed forces $q_{j,v_i}(t)[N_b \times 1]$ acting on the N_b beams of the structural frame can be written as: $q(t) =$

Chapter 4. Simulation-based approach for wind-induced fatigue calculation of megastructures

$Ap(t)$ where A is a matrix $[N_b \times N_k]$ depending on the choice of the area weighting. Finally, the time histories of the distributed forces are converted into equivalent nodal forces p_{ijn} .

For each $ij - th$ couple (i.e., for each couple of wind velocity and direction), a dynamic simulation is performed through modal analysis. In case of a linear transient modal analysis, the dynamic equilibrium equation is shown in the following:

$$\ddot{q}_n(t) + 2\zeta\omega\dot{q}_n(t) + \omega_n^2q_n(t) = \phi_n^T A_n p_{ijn}(t) \quad (4.5)$$

where:

- $q_n(t)$ is the $n - th$ modal coordinate;
- n is the considered structural mode;
- t is time;
- $\omega_n = 2\pi f_n$ is the circular natural frequency $[rad/s]$ with f_n the natural frequency $[Hz]$;
- ζ_n is the $n - th$ damping ratio;
- ϕ_n is the $n - th$ vibrational shape for each node normalized with unitary mass.

q_{ijn} is the time history of displacements of all the nodes of the frame structure for $i - th$ wind velocity and $j - th$ block, obtained by numerical solution. q_{ijn} is a vector with 6 components, corresponding to the six degrees of freedom of displacement for each node.

4.4 Statistical analysis of wind data

The current block flow chart is summarized in figure 4.4.

4.4. Statistical analysis of wind data

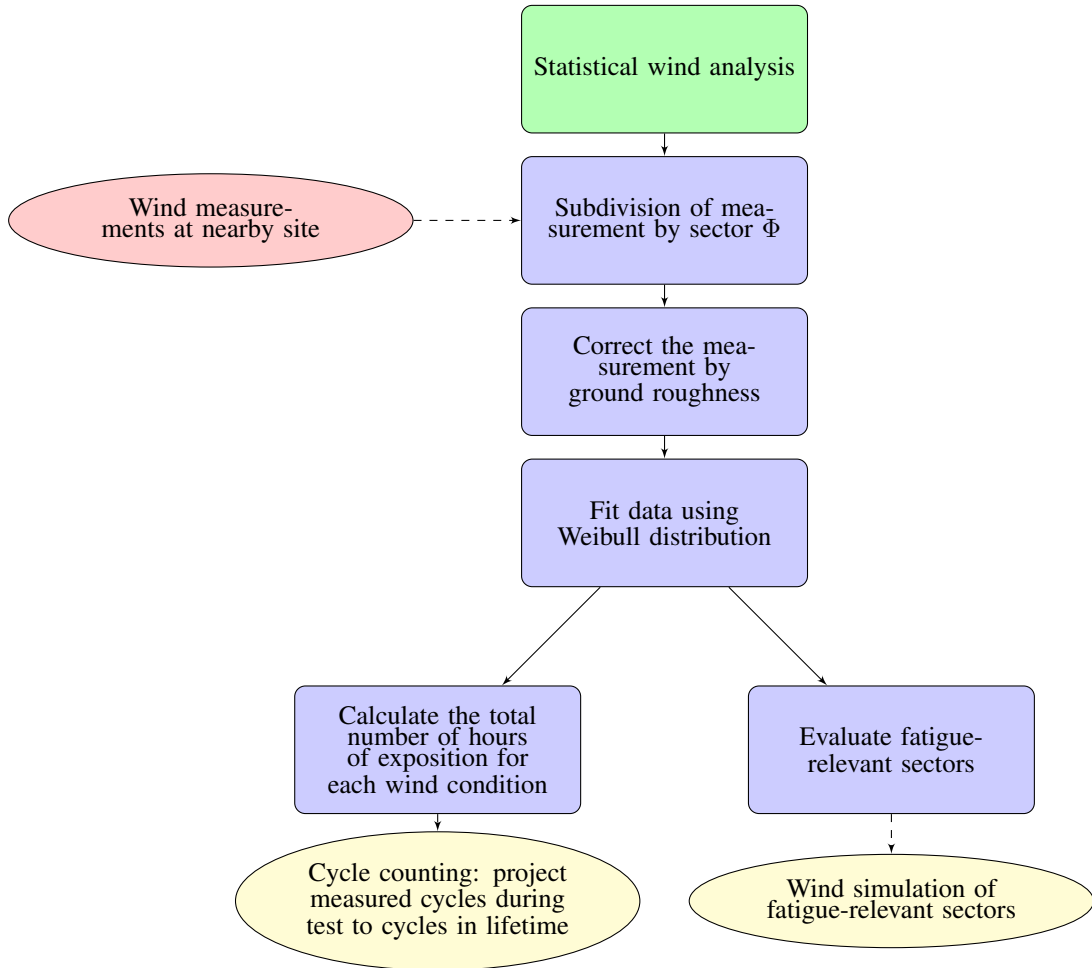


Figure 4.4: *Statistical wind analysis*

The measurements obtained by the anemometer placed near the building site are the reference input for carrying out the statistical analysis. The measurements should span as many years as possible, and include information on the mean wind speed V , collected at a given resolution, which might be $\tau = 1min, 10min, 1h...$ and on the corresponding directional sector Φ .

As the measured mean wind speeds depend on the ground roughness z_0 in the surroundings of the station site, they need to be converted to the equivalent mean wind speed V_b related to a reference roughness, which for the Eurocode EN 1991-1-4 is a ground of Category II. A correction factor $k(\Phi)$ is therefore introduced for each sector. Its expression is defined following the mean wind profile expression provided by EN 1991-1-4:

$$k(\Phi) = \frac{V_b(\bar{z}, \Phi)}{V(\bar{z}, \Phi)} = \frac{C_{r,II}(\bar{z})}{C_r(\bar{z}, \Phi)} = \left(\frac{z_{0,II}}{z_0(\Phi)} \right)^{0.07} \left[\frac{\ln \bar{z}/z_{0,II}}{\ln \bar{z}/z_0(\Phi)} \right] \quad (4.6)$$

Chapter 4. Simulation-based approach for wind-induced fatigue calculation of megastructures

where \bar{z} is the anemometer elevation (usually 10 m), $z_{0,II}$ is the roughness length associated to a ground of category II ($z_{0,II} = 0.05$) and c_r is the roughness factor. The higher is the roughness length of the station site with respect to the one associated to a ground of category II, the lower are the mean wind speeds measured at the station site, and therefore the higher is the correction factor $k(\Phi)$.

Before the wind data population is fitted by a probabilistic Weibull curve, the population of mean wind speed V_b must be converted at the reference height of 10 m to the corresponding mean wind speed V_r at the reference height of the building h , by using the mean wind speed profile:

$$V_r(\Phi) = V_b(\bar{z}, \Phi) k_r \ln \left(\frac{h}{z_{0,s}(\Phi)} \right) \quad (4.7)$$

where $z_{0,s}$ is the roughness length at the building site. The population of mean wind speeds V_r is then fitted using a probabilistic Weibull curve. By considering the following parameters:

- N_t : the number of couples of mean wind speed and direction data (V_r, Φ) constituting the basis of the population of data;
- N_0 : the number of occurrence of calm wind, i.e. conventionally associated to $V_b < 0.5m/s$;
- $P_0 = N_0/N_t$: the probability of occurrence of calm wind;
- N_j : the number of occurrence of all wind speeds, in case $V_b > 0.5m/s$, associated to the $j - th$ sector ($j = 1, 2, \dots, S$). The latter has amplitude $\Delta\Phi = 360/S$ and it is centered on the angle $\Phi_j = \frac{1}{2}(2j - 1) \Delta\Phi$
- $P_j = N_j / (N_t - N_0)$: the directional probability of $j - th$ sector.

A Hybrid Weibull model describes the joint probability density function of wind speeds and directions [118]:

$$p_j(V) = (1 - P_0) P_j f_j(V) = \left(1 - \frac{N_0}{N_t} \right) \frac{N_j k_j}{N_t c_j} \left(\frac{V}{c_j} \right)^{k_j-1} e^{-\left[\left(\frac{V}{c_j} \right)^{k_j} \right]} \quad (4.8)$$

where c_j and k_j are respectively the scale factor and the shape factors of the Weibull distribution, obtained through a fitting algorithm. The probability density function can be also converted in terms of hours of joint occurrence of a wind speed V_i and a sector

j during the lifetime of the structure T , expressed as:

$$N_j(V_i) = Tp_j(V_i) \quad (4.9)$$

Equation 4.9 defines the total number of hours in which the structure is subject to a particular condition of wind, coming from the sector j – th with a mean velocity V_i and allows to project the total number of fatigue cycles measured in this particular condition during the test to the lifetime of the structure.

By plotting the joint probabilities into a polar diagram (V_m, Φ) or by observing the total hours of exposition to each wind direction, it is possible to evaluate the *fatigue-relevant sectors*. It is often the case that the wind directions with higher probability of occurrence are also the ones associated to stronger wind speeds. Each of these sector must be evaluated against fatigue as, potentially, it could lead to accumulation of damage. On the contrary, some wind directions might be associated to low probability and low wind speed and it is highly unlikely that wind coming from these directions can cause any fatigue damage. If the wind simulation is carried out through CFD tests, the identification of *fatigue-relevant sectors* allows the simulation engineer to reduce the number of unneeded simulations with, possibly, a dramatic reduction in computational effort or to increase the number of simulations for most relevant directions. In addition, as it will be shown in Chapter 6 with reference to the case study, the identification of the fatigue-relevant directions allows a better understanding of the fatigue behaviour of a structure and the identification of potential critical details.

4.5 Cycle-counting

The cycle-counting procedure allows to actually define the fatigue load spectrum in a part of the structure. The term *fatigue load spectrum* is here intended to represent a discrete distribution of cycles as cross-joint function of the stress range $\Delta\sigma$ and of the mean stress $\bar{\sigma}$. As the computational resources usually do not allow to perform a full transient analysis on a detailed shell FE model, beam models are employed to obtain a robust representation of the time history of displacements of all nodes of a frame structure. However, being fatigue a local phenomena, it is necessary to evaluate the fatigue load spectrum at *local* level, which means, near the details that need to be investigated. In fact, in complex frame structures, several beams usually concur into a connection, and each beam may be excited by different dynamic components of the flow, causing the connection to respond to different frequencies asynchronously in different points. Also, the connection itself has details which may alter the internal

Chapter 4. Simulation-based approach for wind-induced fatigue calculation of megastructures

distribution of stresses.

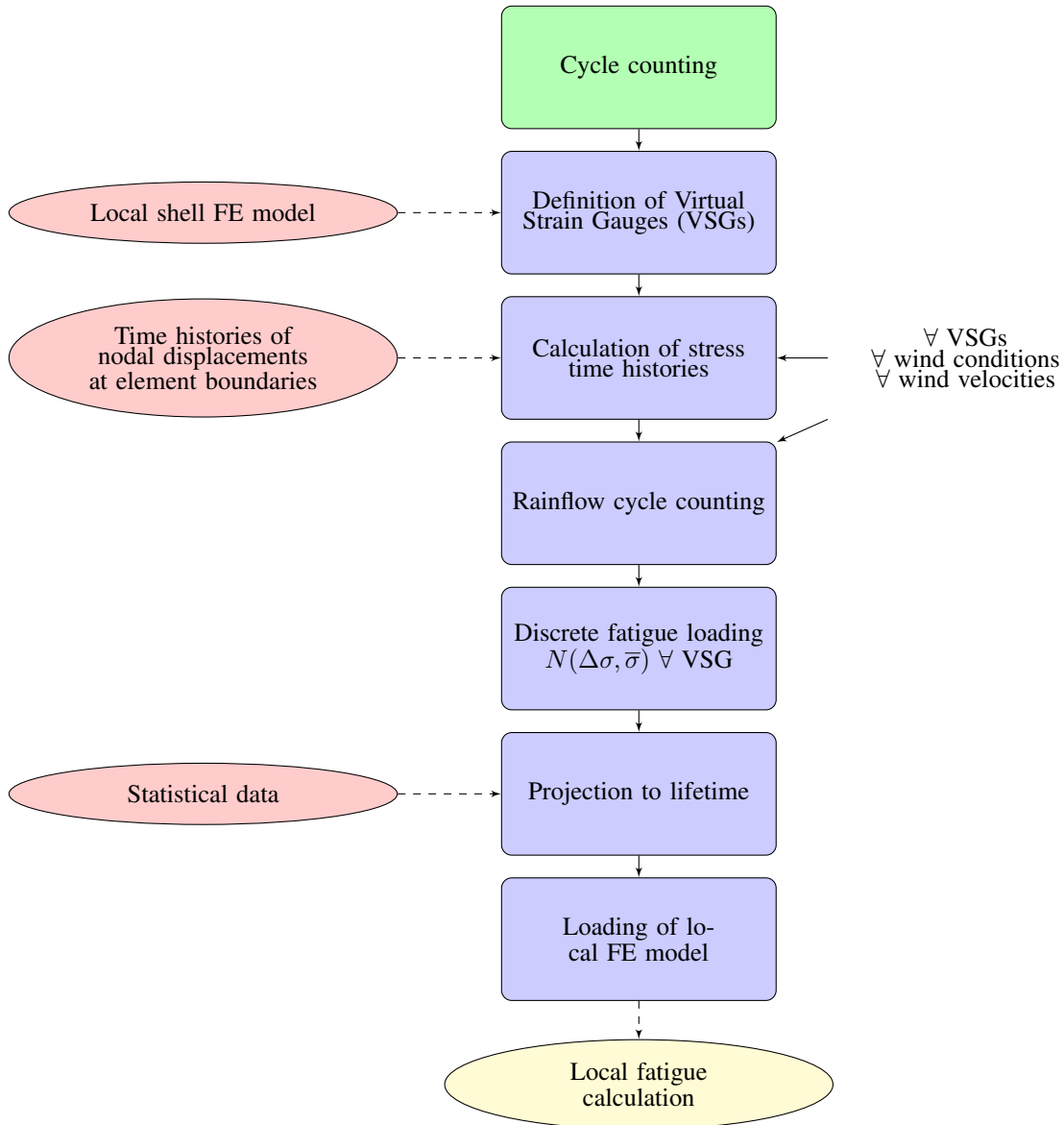


Figure 4.5: *Cycle counting flow chart*

Also, calculation time does not permit to just apply the displacements calculated from the modal analysis to the local model and to perform rainflow cycle counting in each spot of the model as this would lead to an excessive computational demand. In fact, for one velocity only, and considering only 10 minutes of time history, with a time step of 0.02 s, the calculation for 8 wind directions would require to perform 8×30000 time steps = 720000 solutions of shell FE model, which would be an excessively demanding burden. In conclusion, the application of complete time histories of

4.5. Cycle-counting

displacements directly to shell FE model appears to be unfeasible.

Starting from the the time histories of all nodal (with nodes denoted with subscript n) displacements obtained from modal analyses of all ij wind conditions $q_{ijn}(t)$ (so, on the global beam FE model), a simple method for calculating the local time history of stress at particular points is therefore proposed. This method introduces the concept of *virtual strain gauges* (in the following, often referred to as VSGs), or, more appropriately, it borrows it from Freight wagons Standards (such as EN 12663-2:2010) or experimental tests (Fig. 4.6). Before the actual cycle-counting procedure is described,

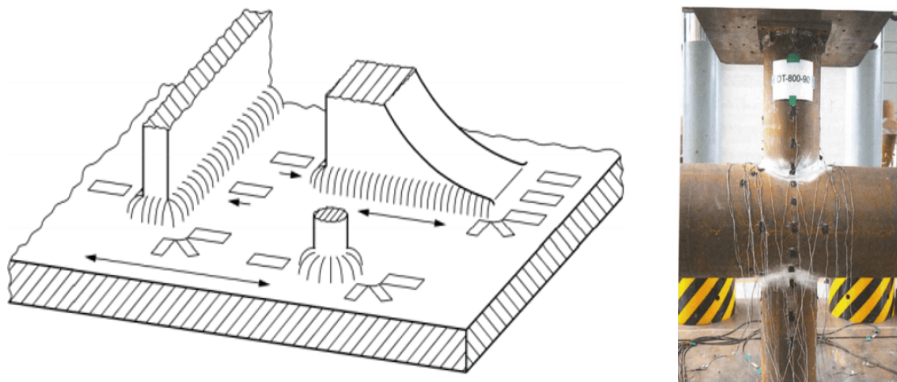


Figure 4.6: *Strain gauges in literature and in experimental tests*

a brief description of the concept of virtual strain gauge is further provided.

A *virtual strain gauge* is a control shell finite-element chosen among the available elements of a shell FE model (Fig. 4.7) to define the behavior of a wider correlated area. For this control element, a function that allows to calculate its stress starting from the displacements at the boundary conditions of the connection, called *Influence vector*, is built.

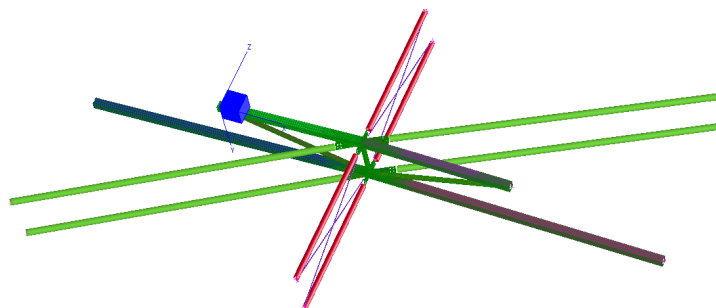


Figure 4.7: *Local shell FE model of a connection*

By using the Influence Vector it is possible to calculate the stress time history in the VSG without solving the complete time history in the local shell FE model, thus

Chapter 4. Simulation-based approach for wind-induced fatigue calculation of megastructures

avoiding extremely burdensome computations. The time history is then treated with the Rainflow Cycle Counting algorithm to calculate the cycles related to a particular ij wind condition. Summarizing, the process for the definition of the VSG is the following:

1. Interaction solution

- A displacement equal to 1 is imposed for one DOF at only one interface node, while all other nodes and DOFs are fixed.
- This boundary condition is repeated for all DOFs of all interface nodes.
- A linear static solution (here referred to as *Interaction solution*) of the local shell FE model is performed.

2. Creation of VSGs:

- One or multiple plates are selected in the local FE model (Fig. 6.36). Each of the selected plates is chosen as VSG.

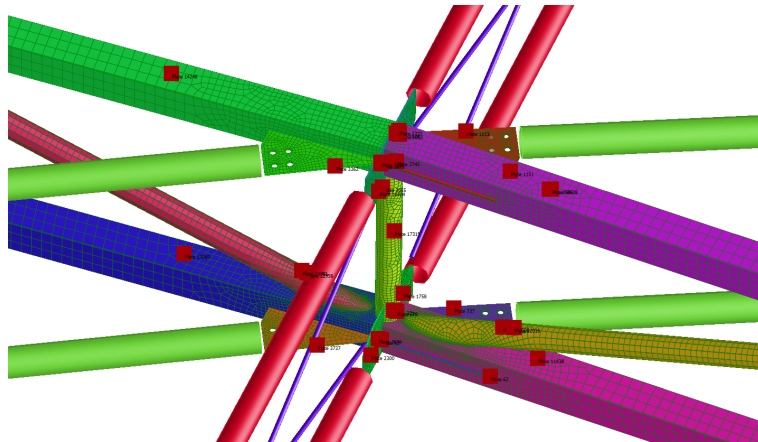


Figure 4.8: *Sample VSGs*

- The VSG is placed at the +z, -z or mid surface of the plate.
- The *Influence Vector* is built for each VSG by reading the σ_{xx} and σ_{yy} stresses from the interaction solution of point 1. and storing them as an array IV_r for the r -th VSG. Each vector component is the stress caused on the centroid of the finite shell element by a unitary displacement at a single DOF in a boundary node. In fact, for a n-way connection, a stress component σ at a plate element generated from a general boundary condition $[DX_1, DY_1, \dots, DX_i, DY_i, \dots, RY_n, RZ_n]$ could be expressed as the

contribution of each connection DOF ($6 \times n$):

$$\begin{aligned}
 \sigma_{DX,1} &= DX_1[a_{dx1}, 0, 0, 0, 0, 0, \dots, 0, 0, 0, 0, 0, 0, \dots, 0, 0, 0, 0, 0, 0] + \\
 \sigma_{DY,1} &= DY_1[0, a_{dy1}, 0, 0, 0, 0, \dots, 0, 0, 0, 0, 0, 0, \dots, 0, 0, 0, 0, 0, 0] + \\
 &\dots \\
 \sigma_{RX,1} &= RX_1[0, 0, 0, a_{rx1}, 0, 0, \dots, 0, 0, 0, 0, 0, 0, \dots, 0, 0, 0, 0, 0, 0] + \\
 &\dots \\
 \sigma_{RZ,n} &= DY_1[0, 0, 0, 0, 0, 0, \dots, 0, 0, 0, 0, 0, 0, \dots, 0, 0, 0, 0, 0, a_{rzn}]
 \end{aligned} \tag{4.10}$$

The coefficients a_i constitute the Influence Vector that multiplies the boundary conditions displacements to obtain the stress at the location of the plate where the VSG is defined.

- The following VSG information are then stored:
 - the influence vector IV ;
 - the position of the VSG in the local FE model;
 - the face of the plate ($+z, mid, -z$);
 - the extracted stress component σ_{xx} or σ_{yy} .

This approach requires to impose the hypothesis that the stress field remains in elastic behaviour so that linear superposition is possible.

As already stated, the VSG is representative of the behavior of a wider correlated area. Within a steel connection located in a much more complex steel structure frame subject to transient wind action, wide zones move synchronously, since they are excited by structural elements which are interested by the same dynamic modes. This means that, within such a correlated area, a stress cycle in a plate element is proportional to a stress cycle in another plate element and thus, if the the time instants of start and end of a cycle are stored, they represent a cycle for both plates. This concept has the following implication: the VSG is not used for actually performing a fatigue check; on the contrary, it must be intended as a *control element* useful to find the time instants of start and end for all the cycles. Since these time instants are related to a set of displacements at the boundary of the connection, these displacements can be imposed at its boundary recreating the stress state in all the plates of the correlated area, thus permitting the detailed fatigue check of the base material and of the welds by means of advanced local fatigue methods.

The counting procedure is further described in major detail using mathematical terms. Let $N_r = \{n_1, n_2, \dots, n_m\}$ the list of nodes at the boundary of the $r - th$ joint.

Chapter 4. Simulation-based approach for wind-induced fatigue calculation of megastructures

$q_{ijn}(t)$ with $n \subseteq N_r$, in the following $q_{ijnr}(t)$. Let $IV_r = \{iv_1, iv_2, \dots, iv_m\}$ where iv_1 is a vector with 6 components, corresponding to the six degrees of freedom of displacement for each node. Each component determines the effect in terms of stress at the $r - th$ VSG.

For each VSG, the stress time history is computed:

$$s_{ijr}(t) = q_{ijnr}(t) \cdot IV_r \quad (4.11)$$

s_{ijr} is the time history of stress at the $r - th$ VSG for $i - th$ wind velocity and for $j - th$ block. $s_{ijr}(t)$ is then subjected to a rainflow cycle counting. The cycle counting is performed for each ijr time history independently.

$$Rainflow(S_{ijr}(t)) \rightarrow N'_{ijr}(\Delta\sigma, \bar{\sigma}) \quad (4.12)$$

where:

- $N'_{ijr}(\Delta\sigma, \bar{\sigma})$ is the number of cycles measured during the test in the VSG;
- Discrete stress range $\Delta\sigma$ bins;
- Discrete stress mean $\bar{\sigma}$ bins.

The number of cycles, here calculated in reference to the duration of the test, is then projected to the lifetime of the structure by multiplying a scalar α_{ij} to each number of cycles inside each bin:

$$N_{ijr}(\Delta\sigma, \bar{\sigma}) = \alpha_{ij} N'_{ijr}(\Delta\sigma, \bar{\sigma}) \quad (4.13)$$

where α_{ij} is the ratio between the total time in the lifetime of the structure in which the wind condition ij is expected and the total time of simulation for the case ij :

$$\alpha_{ij} = T_{50,ij} / T_{sim,ij} \quad (4.14)$$

The number of cycles considered for all the conditions ij for a VSG are then summed to obtain the wind-induced fatigue spectrum at the point:

$$N_r(\Delta\sigma, \bar{\sigma}) = \sum_i \sum_j N_{ijr}(\Delta\sigma, \bar{\sigma}) \quad (4.15)$$

At this point it is possible to impose the stress field related to the cycle measured in the VSG on the local shell FE model.

4.6 Loading of local shell FE model

For each $(\Delta\sigma, \bar{\sigma})$ of N_{rst} , a $\Delta q_{nr}(t)$ is selected, where $\Delta q_{nr}(t)$ is the difference between displacements at start and end of a cycle representative of a bin.

For each VSG there is a set of $N_{bins} \times N_{bins}$ of $\Delta q_{nrst}, N_{rst}$. Δq_{nrst} imposes the boundary conditions that introduce the load $\Delta\sigma_s$ in position of r -th VSG, related to the mean value $\bar{\sigma}$, thus obtaining the wind-induced fatigue spectrum in the area correlated to the VSG.

The subdivision of cycles is performed over the mean value of stress, and not only to the range, with the purpose to obtain a more representative boundary condition for all the shell elements inside the correlated area.

The local shell FE model is then used to calculate fatigue on base material and on welds in the zones correlated with r - th VSG. The number of VSGs must be high enough to cover spatially all the surface of the structure.

4.7 Detailed fatigue calculation

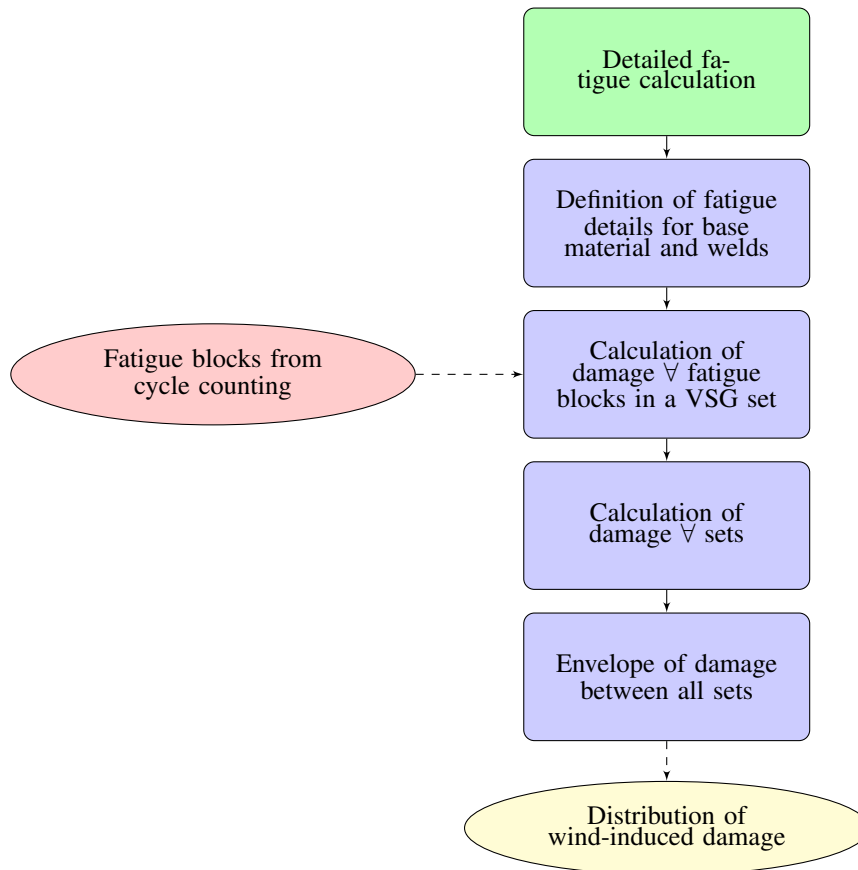


Figure 4.9: *Detailed fatigue calculation*

4.7.1 Base material checks

Base material can be subdivided in free edges and plate material. For the internal material, Table 8.1 detail 1 corresponding to FAT160 can be assigned for direct stress ranges ($\Delta\sigma$) and Table 8.1 detail 6, corresponding to FAT100 can be assigned for shear stress ranges ($\Delta\tau$). The combined effects are taken into account by summing each damage contribution according to EN 1993-1-9 §8(8.3).

On the other side, each finite element representing the free edge of a plate can be assigned with Table 8.1, detail 5, corresponding to FAT125 for direct stress ranges ($\Delta\sigma$).

An example an assigned fatigue details map is shown in Fig. 4.10, where edges are coloured in blue.

4.7. Detailed fatigue calculation

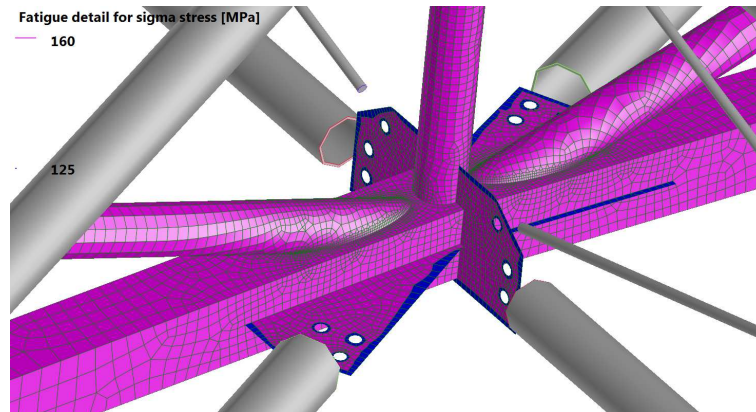


Figure 4.10: *Visualuzation of free edes (blue) and base material (purple)*

For each shell surface, both + or - z, the damage has been calculated in the following manner:

- Stresses are extracted from the element centroid, reading $\Delta\sigma_x$, $\Delta\sigma_y$, $\Delta\sigma_{xy}$ in the local coordinate system;
- The first failure mode considered is the presence of a defect perpendicular to $\Delta\sigma_y$. The damage contribution of $\Delta\sigma_x$ and $\Delta\tau_{xy}$ is summed for each block spectrum;
- The second failure mode considered is the presence of a defect perpendicular to $\Delta\sigma_x$. The damage contribution of $\Delta\sigma_y$ and $\Delta\tau_{xy}$ is summed for each block spectrum.

Only the worst failure mode is conserved for each element to present the results.

4.7.2 Welded joints checks

The assessment of fatigue resistance can be performed according to the modified nominal stress method of EN 1993-1-9, Clause 6.1, detailed in Chapter 3. For the most general case of a double fillet weld all-around a total of 28 check are performed utilizing the corresponding details of EN 1993-1-9 contained in the tables from 8.1 to 8.10. Of these 28 checks, 14 are at the start (7) and finish (7) of the weld and, for the others 14, the maximum check is found along the weld.

Toe checks

Toe failure along the weld are schematized in Fig. 4.11

Chapter 4. Simulation-based approach for wind-induced fatigue calculation of megastructures

Check	Stress component	Detail
<i>b</i>	$\Delta\sigma_{\perp}$	Tab. 8.5 - Det.1
<i>c</i>	$\Delta\sigma_{\parallel}$	Tab. 8.2 - Det.5
<i>d</i>	$\Delta\sigma_{\perp}$	Tab. 8.4 - Det.6
<i>e</i>	$\Delta\sigma_{\parallel}$	Tab. 8.2 - Det.5

Table 4.1: Toe checks to be performed along the weld

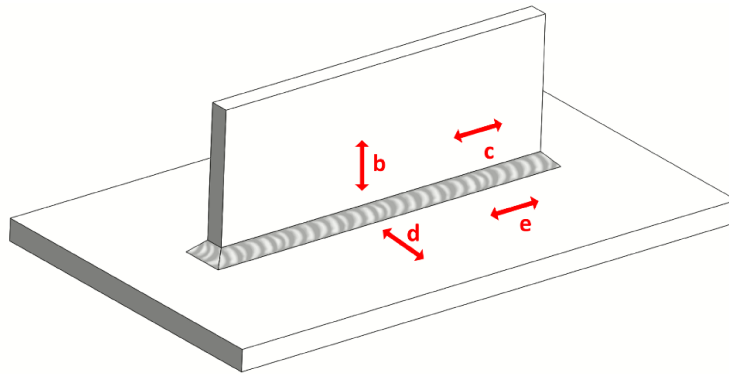


Figure 4.11: Toe checks to be performed along the weld

For each check, the Eurocode details shown in Table 4.1 are utilized.

In the all around zone the following checks need to be performed (Fig. 4.12):

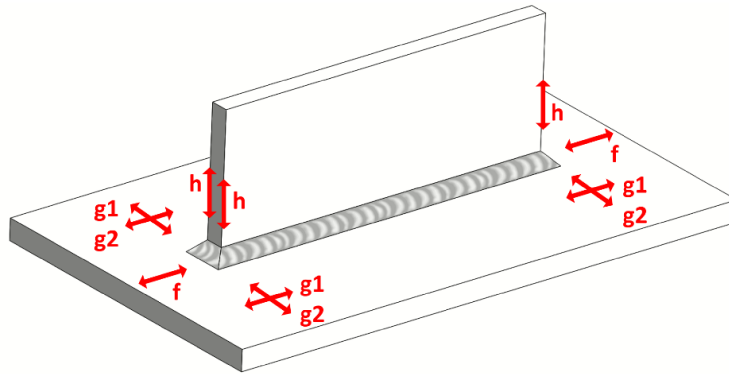


Figure 4.12: Toe checks to be performed at the start and finish of the weld

For each check, the Eurocode details shown in Table 4.2 are utilized.

For the *g1* and *g2* checks, a principal stress is employed:

$$\Delta\sigma_{eq,\perp} = \frac{1}{2} \left(\Delta\sigma_{\perp} + \sqrt{\Delta\sigma_{\perp}^2 + 4\Delta\sigma_{\parallel}^2} \right) \quad (4.16)$$

$$\Delta\sigma_{eq,\parallel} = \frac{1}{2} \left(\Delta\sigma_{\parallel} + \sqrt{\Delta\sigma_{\parallel}^2 + 4\Delta\sigma_{\perp}^2} \right) \quad (4.17)$$

4.7. Detailed fatigue calculation

Check	Stress component	Detail
<i>f</i>	$\Delta\sigma_{\parallel}$	Tab. 8.4 - Det.1
<i>g1</i>	$\Delta\sigma_{eq\perp}$	Tab. 8.9 - Det. 2
<i>g2</i>	$\Delta\sigma_{eq\parallel}$	Tab. 8.9 - Det. 2
<i>h</i>	$\Delta\sigma_{\perp}$	Tab. 8.9 - Det. 1

Table 4.2: Toe checks to be performed at the start and finish of the weld

Check	Stress component	Detail
<i>a1</i>	$\Delta\sigma_{wf}$	Tab. 8.5 - Det.3
<i>a2</i>	$\Delta\tau_{wf}$	Tab. 8.5 - Det.8
<i>a</i>	$\Delta\sigma_{wf}, \Delta\tau_{wf}$	EN 1993-1-9, Clause 8.3

Table 4.3: Root checks to be performed along the weld

Root checks

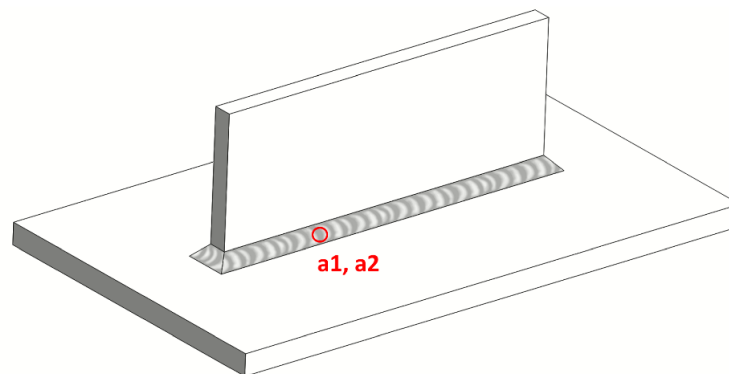


Figure 4.13: Root checks to be performed along the weld

For each check, the Eurocode details shown in Table 4.3 are utilized. Root failure is conducted utilizing relevant stresses calculated along the weld for each weld bead as indicated in EN 1993-1-9, Clause 5, as shown in Fig. 4.14.

Root checks

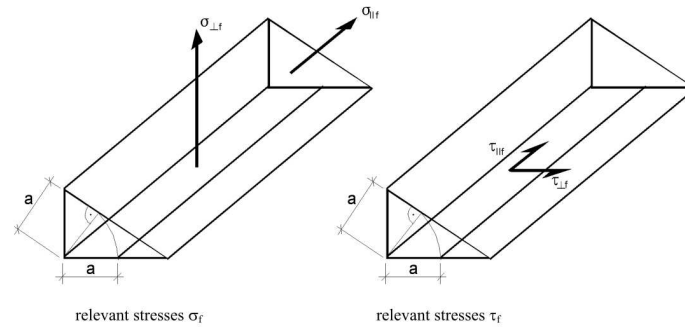


Figure 4.14: *Relevant stresses considered for the check*

The stress components for the $a1$, $a2$ and a checks are calculated from Equations 4.7.2, 4.7.2:

$$\Delta\sigma_{wf} = \sqrt{\Delta\sigma_{\perp}^2 + \Delta\tau_{\perp}^2} \quad (4.18)$$

$$\Delta\tau_{wf} = \Delta\tau_{\parallel} \quad (4.19)$$

Both checks $a1$ and $a2$ are then combined in check a summing each damage contribution as indicated in EN 1993-1-9, Clause 8.3. The worst point along the weld determines the maximum root damage.

Size effect

The FAT class is modified by means of the size effect as indicated in EN 1993-1-9 Tab. 8.3, to consider an increased quantity of defects in large volumes. According to IIW “Recommendations for Fatigue Design of Welded Joints and Components”, in the same way a benign thinness effect might be considered for thickness values lower than the reference.

Modified Nominal Stress

As discussed in Section 3.2, stresses read at shell elements intersection are affected by a stress raising effect that is already included in the FAT category. Modified nominal stresses are thus read at a distance δ from the weld to exclude stress concentrations effects, as shown in Fig. 4.15.

4.7. Detailed fatigue calculation

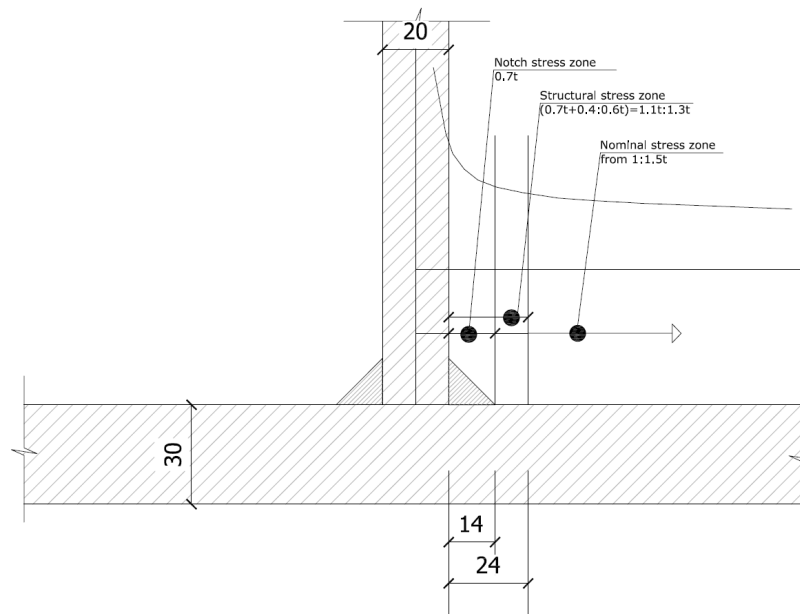


Figure 4.15: *Stress concentrations effects*

The stress concentration factor K_f to take account of the local stress magnification in relation to detail geometry not included in the reference S-N curve has been calculated by appropriate finite element calculations (EN 1993-1-9, clause 6.3). In literature and in the industrial practise, one of the most generalized, flexible and numerically performing method to calculate the correction factor is the Strain Energy Density method, discussed in Section 3.2.2.

CHAPTER 5

New Partially Averaged Navier Stokes model development and validation

5.1 Highlights

In this chapter the equations of the original PANS models are obtained. The motivation for the development of these two original PANS models lies in the necessity of improving models in the $k - \varepsilon$ framework to achieve a more accurate result even at higher f_k filter values compared to the Standard $k - \varepsilon$. The first developed model is the Realizable $k - \varepsilon$ PANS and is based on the Shih Realizable $k - \varepsilon$ [132], which is proven to be an efficient model for the assessment of flow phenomena such as separation and secondary flows. This model is conceived as a high-Reynolds model and it suitable for cases where mesh requirements are particularly high.

The second original model is called $v^2 - f$ with variable C_μ PANS, and combines the variable formulation of the coefficient C_μ of the Realizable $k - \varepsilon$ model, which provides a better representation of the phenomena of separation and recirculation with the improved wall modeling of the $v^2 - f$ model and is brought into the formulation PANS to release the maximum number of turbulent scales allowed by the computational

Chapter 5. New Partially Averaged Navier Stokes model development and validation

grid and filter-width parameters. The latter model is a higher resolution model, which requires a thicker wall mesh than the former, however it has the advantage of integrating the flow field up to the wall without requiring wall functions, and thus it doesn't set a lower limit to wall discretization making the process of generating the mesh easier.

Both models are validated on a typical case such as the backwards facing step, in which both models show an improvement compared to the literature available Standard $k - \varepsilon$ PANS model, in predicting the medium and fluctuating fluid motion field along the domain. In particular, it is shown that the model $v^2 - f$ exhibits better results than the others for all the values of the filter f_k PANS, thanks to the superiority of its formulation.

The Realizable $k - \varepsilon$ PANS model is also compared to the $k - \varepsilon$ PANS and to LES in the literature case of the square cylinder. Again, the original model shows good results compared to existing literature and models.

5.2 Realizable $k - \varepsilon$ PANS equations

The Realizable $k - \varepsilon$ PANS model derivation is developed with the same approach shown for the Standard $k - \varepsilon$ PANS in Section 2.1.8 and starts from the Realizable $k - \varepsilon$ model, described in 2.1.4, as parent RANS formulation. As defined by Girimaji [125], the PANS development:

"involves three important steps: (i) identification of the PANS filter-control parameters; (ii) development of the SFS stress constitutive relationship; (iii) derivation of the unresolved kinetic energy and dissipation evolution equations."

First, the PANS filter-control parameter are defined in accordance to the original paper of Girimaji, f_k and f_ε with:

$$f_k = \frac{K_u}{k}, f_\varepsilon = \frac{\varepsilon_u}{\varepsilon} \quad (5.1)$$

The parameters f_k and f_ε are assumed to be constant in time.

The second step involves the development of the SFS stress constitutive relationship. The Boussinesq constitutive approximation is defined by:

$$\tau (V_i, V_j) = -\nu_u S_{ij} \quad (5.2)$$

$$\nu_u = C_\mu \frac{K_u^2}{\varepsilon_u} \quad (5.3)$$

5.2. Realizable $k - \varepsilon$ PANS equations

The constant C_μ is expressed in function of the unresolved components:

$$C_\mu = \frac{1}{A_0 + A_s U^* \frac{K_u f_\varepsilon}{\varepsilon_u f_k}} \quad (5.4)$$

The choice of the SFS stress constitutive equation is done in accordance to the original paper by Girimaji and does not reduce the value of C_μ from the RANS formulation to avoid a lower dissipation which would lead to higher-than-desired levels of unresolved kinetic energy. As in Realizable formulation the C_μ parameter is not constant, but it is dependent on k and ε , its formulation is rewritten in function of the unresolved components. The transport equations of k and ε are written in respect to their unresolved components. The PANS transport equation for the unresolved turbulent kinetic energy K_u is

$$\frac{\partial K_u}{\partial t} + U_j \frac{\partial K_u}{\partial x_j} = \frac{\partial}{\partial x_j} \left(\frac{\nu_u}{\sigma_{ku}} \frac{\partial K_u}{\partial x_j} \right) + P_u - \frac{f_k}{f_\varepsilon} \varepsilon_u \quad (5.5)$$

where

$$P_u = \nu_u \frac{f_\varepsilon}{f_k} \left(\frac{\partial U_i}{\partial x_j} + \frac{\partial U_j}{\partial x_i} \right) \frac{\partial U_i}{\partial x_j} - \frac{2}{3} K_u \delta_{xj} \frac{\partial U_i}{\partial x_j} \quad (5.6)$$

The zero-transport hypothesis [56] assumes that resolved fluctuations do not contribute to sub-filter-stress (SFS) energy transport. Since this model is developed specifically for high-Reynolds flows, these hypothesis are reasonable and lead to the following Prandtl number:

$$\sigma_{ku} = \sigma_k \frac{f_k^2}{f_\varepsilon} \quad (5.7)$$

The equation of the source-sink terms between the transport equation of the unresolved turbulent kinetic energy K_u and of the RANS equation of k is:

$$P = \frac{1}{f_k} (P_u - \varepsilon_u) + \varepsilon_u \quad (5.8)$$

The transport equation of the unresolved dissipation equation is:

$$\frac{\partial \varepsilon_u}{\partial t} + U_j \frac{\partial \varepsilon_u}{\partial x_j} = \frac{\partial}{\partial x_j} \left(\frac{\nu_u}{\sigma_{\varepsilon u}} \frac{\partial \varepsilon_u}{\partial x_j} \right) + C_1 S \varepsilon_u - C_2 \frac{\varepsilon_u^2}{\frac{f_\varepsilon}{f_k} K_u + f_\varepsilon \sqrt{\nu \frac{\varepsilon_u}{f_\varepsilon}}} \quad (5.9)$$

where

$$C_1 = \max \left\{ 0.43, \frac{\eta}{5 + \eta} \right\} \quad (5.10)$$

$$\eta = S \frac{K_u f_\varepsilon}{\varepsilon_u f_k} \quad (5.11)$$

Chapter 5. New Partially Averaged Navier Stokes model development and validation

Under zero-transport hypothesis, the Prandtl number for unresolved dissipation is:

$$\sigma_{\varepsilon u} = \sigma_{\varepsilon} \frac{f_k^2}{f_{\varepsilon}} \quad (5.12)$$

The other parameters of the model are those of the parent RANS (see equations 2.20, 2.21, 2.22, 2.23, 2.24, 2.25).

5.3 $\overline{v^2} - f$ with variable C_{μ} PANS equations

The second original model starts from the Durbin's $v^2 - f$ modified by Lien and Kalitzin [127] and by Davidson, Nielsen and Sveningsson [123] presented in Section 2.1.6. The variable C_{μ} coefficient from [132] is then introduced in this model to improve the calculation of the turbulent viscosity, especially in separated zones. Finally, the model is transformed to PANS formulation using the approach proposed by [60] similarly to the implementation of the $\zeta - f$ PANS model proposed by Basara et al. [120].

The purpose of this model is to put together the strengths of the two starting models, the Realizable $k - \varepsilon$, which has excellent behavior in separate areas, and the $v^2 - f$, which has excellent behavior near the wall, and to rewrite this new model according to the PANS approach developed by Girimaji to liberate as much as possible of turbulent scales of motion.

The first modification of the model consists in the introduction of the variable C_{μ} coefficient from the Realizable $k - \varepsilon$ model of Shih. This modification allows to take into account that experimental data suggests that on inertial sublayer of a channel or in boundary layer flow C_{μ} shall be considered equal to 0.09, while, for a homogeneous shear flow, $C_{\mu} = \frac{\overline{uv}}{k} / \frac{k}{\varepsilon} \frac{\partial U}{\partial y}$ is about 0.05. This consideration led Reynolds and Shih to the proposal of the variable formulation of C_{μ} , already shown in Eq. 2.19, which is here called $C_{\mu, RKE}$.

The definition of the variable coefficient C_{μ} is introduced into the equation of the turbulent viscosity in proportion to the constant value of $C_{\mu, SKE} = 0.09$ used by the model $k - \varepsilon$ Standard. In this way, the turbulent viscosity is defined as follows:

$$\nu_t = \min \left[C_{\mu, RKE} \frac{k^2}{\varepsilon}, C_{\mu} \frac{C_{\mu, RKE}}{C_{\mu, SKE}} \overline{v'^2 T} \right] \quad (5.13)$$

The model is then treated using Partially Averaging approach, following the procedure presented by Girimaji [60]. The filter-width parameters are further introduced:

5.3. $\overline{v^2} - f$ with variable C_μ PANS equations

- $f_k = K_u/k$ is the filter-width parameter of turbulent kinetic energy;
- $f_\varepsilon = \varepsilon/\varepsilon_u$ is the filter-width parameter of dissipation;
- $f_{v'^2} = \overline{v_u'^2}/\overline{v'^2}$ is the filter-width parameter of normal wall stress;

The unresolved turbulent viscosity is defined in relation to unresolved fields as:

$$\nu_u = \min \left[C_{\mu,RKE} \frac{K_u^2}{\varepsilon_u}, C_\mu \frac{C_{\mu,RKE}}{C_{\mu,SKE}} \overline{v_u'^2} T_u \right] \quad (5.14)$$

Where $T_u = \frac{f_k}{f_\varepsilon} T$ is the unresolved turbulent time-scale.

The equation of the unresolved turbulent kinetic energy k_u is the same of the Standard $k - \varepsilon$ PANS model, as the equation of k is not changed from Standard model. The equation is derived by equating source-sink terms:

$$\frac{\partial K_u}{\partial t} + U_j \frac{\partial K_u}{\partial x_j} = P_u - \varepsilon_u + \frac{\partial}{\partial x_j} \left(\frac{\nu_u}{\sigma_{ku}} \frac{\partial K_u}{\partial x_j} \right) \quad (5.15)$$

where Prandtl unresolved coefficient is $\sigma_{ku} = \sigma_k \frac{f_k^2}{f_\varepsilon}$. The PANS unresolved dissipation transport equation ε_u is derived similarly to the dissipation of the Standard $k - \varepsilon$ model, with the difference that the turbulent time scale appears in the current equation. Since the filter-width parameter f_ε is defined as the ratio of ε and ε_u ,

$$\frac{\partial}{\partial t} \left(\frac{\varepsilon_u}{\varepsilon} \right) + \overline{U}_j \frac{\partial}{\partial x_j} \left(\frac{\varepsilon_u}{\varepsilon} \right) = 0 \quad (5.16)$$

which leads to:

$$\frac{\partial \varepsilon_u}{\partial t} + U_j \frac{\partial \varepsilon_u}{\partial x_j} = \frac{C_{\varepsilon 1} P_k f_\varepsilon}{T} - \frac{C_{\varepsilon 2} \varepsilon_u f_k}{T_u f_\varepsilon} + \frac{\partial}{\partial x_j} \left(\left(\nu + \frac{\nu_t}{\sigma_\varepsilon} \right) \frac{\partial \varepsilon_u}{\partial x_j} \right) + (U_j - \overline{U}_j) \frac{\partial \varepsilon_u}{\partial x_j} \quad (5.17)$$

In the Zero-Transport model hypothesis, which assume that the resolved fluctuation do not contribute to sub-filter-stress energy transport,

$$\frac{\partial}{\partial x_j} \left(\left(\nu + \frac{\nu_t}{\sigma_\varepsilon} \right) \frac{\partial \varepsilon_u}{\partial x_j} \right) + (U_j - \overline{U}_j) \frac{\partial \varepsilon_u}{\partial x_j} = \frac{\partial}{\partial x_j} \left(\left(\nu + \frac{\nu_u}{\sigma_{\varepsilon u}} \right) \frac{\partial \varepsilon_u}{\partial x_j} \right) \quad (5.18)$$

A new coefficient which depends on the filter-width parameters f_k and f_ε is introduced to rewrite the equation more efficiently:

$$C_{\varepsilon 2}^* = C_{\varepsilon 1} + \frac{f_k}{f_\varepsilon} (C_{\varepsilon 2} - C_{\varepsilon 1}) \quad (5.19)$$

Chapter 5. New Partially Averaged Navier Stokes model development and validation

The transport equation of the unresolved dissipation becomes:

$$\frac{\partial \varepsilon_u}{\partial t} + U_j \frac{\partial \varepsilon_u}{\partial x_j} = C_{\varepsilon 1} \frac{P_u}{T_u} - C_{\varepsilon 2}^* \frac{\varepsilon_u}{T_u} + \frac{\partial}{\partial x_j} \left(\left(\nu + \frac{\nu_u}{\sigma_{\varepsilon u}} \right) \frac{\partial \varepsilon_u}{\partial x_j} \right) \quad (5.20)$$

The transport equation of $\overline{v_u'^2}$ is further derived. Starting from the definition of the filter-width parameter $f_{v'^2} = \overline{v_u'^2} / \overline{v'^2}$:

$$\frac{\partial}{\partial t} \left(\frac{\overline{v_u'^2}}{\overline{v'^2}} \right) + \overline{U}_j \frac{\partial}{\partial x_j} \left(\frac{\overline{v_u'^2}}{\overline{v'^2}} \right) = 0 \quad (5.21)$$

which leads to:

$$\frac{\partial \overline{v_u'^2}}{\partial t} + \overline{U}_j \frac{\partial \overline{v_u'^2}}{\partial x_j} = f_{v'^2} \left\{ \overline{v'^2}_{source} - 6 \overline{v'^2} \frac{\varepsilon}{k} + \frac{\partial}{\partial x_j} \left[\left(\nu + \frac{\nu_t}{\sigma_k} \right) \frac{\partial \overline{v'^2}}{\partial x_j} \right] \right\} \quad (5.22)$$

Since $\overline{v'^2}$ and k are both related to a squared velocity, it is further assumed that $f_{v'^2} \simeq f_k$. This is reasonable as f is a relaxation function which does not actually model a physical quantity of the flow.

A coefficient $f_u = \left(\frac{f_k}{f_{v'^2}} \right) f$ is also introduced for the elliptic relaxation function. With the previous hypothesis it is clear that $f_u = 1$. By considering, from the equation of the source-sink terms in the K_u equation, that $P_k = \frac{1}{f_k} (P_u - \varepsilon_u) + \frac{\varepsilon_u}{f_\varepsilon}$, the unresolved source term is further derived:

$$\begin{aligned} \overline{v_u'^2}_{source} = \min \left\{ k_u f_u, \frac{f_k}{T_u f_\varepsilon} \left[(C_1 - 6) \overline{v_u'^2} - \frac{2}{3} K_u (C_1 - 1) \right] \right. \\ \left. + C_2 \left[P_u + \varepsilon_u \left(\frac{f_k}{f_\varepsilon} \right) \right] \right\} \end{aligned} \quad (5.23)$$

By imposing the zero-transport hypothesis:

$$\frac{\partial}{\partial x_j} \left(\left(\nu + \frac{\nu_t}{\sigma_{v'^2}} \right) \frac{\partial \overline{v_u'^2}}{\partial x_j} \right) + (U_j - \overline{U}_j) \frac{\partial \overline{v_u'^2}}{\partial x_j} = \frac{\partial}{\partial x_j} \left(\left(\nu + \frac{\nu_u}{\sigma_{v'^2 u}} \right) \frac{\partial \overline{v_u'^2}}{\partial x_j} \right) \quad (5.24)$$

Where $\sigma_{v'^2 u} = \sigma_{k u}$. It is now possible to obtain the final derivation of the $\overline{v_u'^2}$ transport equation:

$$\frac{\partial \overline{v_u'^2}}{\partial t} + U_j \frac{\partial \overline{v_u'^2}}{\partial x_j} = \overline{v_u'^2}_{source} - 6 \overline{v_u'^2} \frac{\varepsilon_u}{k_u} \frac{f_k}{f_\varepsilon} + \frac{\partial}{\partial x_j} \left[\left(\nu + \frac{\nu_u}{\sigma_k} \right) \frac{\partial \overline{v_u'^2}}{\partial x_j} \right] \quad (5.25)$$

Finally, the equation of the elliptic relaxation function is simply rewritten for the

unresolved variables:

$$L_u^2 \nabla^2 f_u = \frac{1}{T_u} \left[(C_1 - 6) \frac{\overline{v_u'^2}}{K_u} - \frac{2}{3} (C_1 - 1) \right] - C_2 \frac{P_u}{K_u} \quad (5.26)$$

where the turbulent unresolved length scale L_u is defined as:

$$L_u = C_L \max \left[\frac{K_u^{3/2}}{\varepsilon_u}, C_\eta \frac{\nu^{3/4}}{\varepsilon_u^{1/4}} \right] \quad (5.27)$$

5.4 Model validation

5.4.1 Flow around square cylinder

Case description

A new turbulence model must be tested against a number of validation cases relevant to the specific applications. In the following, the flow around a square cylinder of diameter $D = 0.04$ at $Re_D = 22000$ is computed (ERCOFTAC classic database, Case C.43). For structural design and wind engineering, the analysis of fluctuating surface pressure distribution and of wind loads acting on bluff bodies is a recurring practical necessity. The case of the square cylinder at high-Reynolds numbers is a particularly interesting validation case as it superimposes three-dimensional turbulent coherent structures to the two-dimensional periodic vortex-shedding structures that generate on the wake of the cylinder [130]. The instantaneous flow quantities $\Phi(t)$ resolved in the numerical calculation can be seen as the superposition of three components: a time-mean component $\overline{\Phi}$, a periodic component $\tilde{\Phi}(t)$ and a turbulent fluctuating component Φ' :

$$\Phi(t) = \overline{\Phi} + \tilde{\Phi}(t) + \Phi' \quad (5.28)$$

The triple decomposition is shown in figure 5.1.

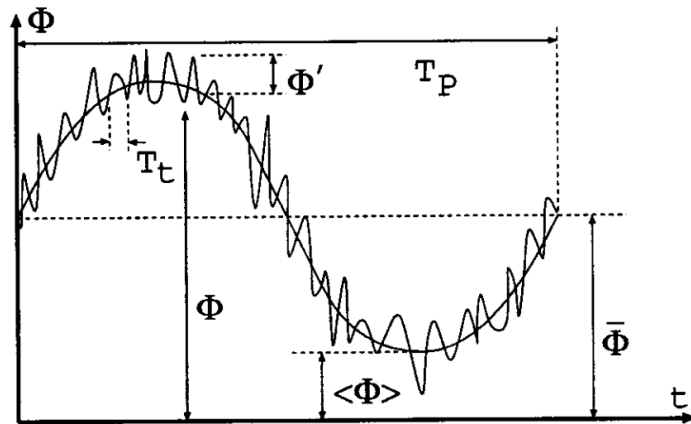


Figure 5.1: Triple decomposition of a turbulent, unsteady signal

Due to the simplicity of the case setup and to the availability of detailed experimental data, flow past a square cylinder is a typical benchmark problem widely adopted for testing turbulence models and LES sub-grid scale models. Here, the calculation is performed at $Re_D = 22000$ in accordance to experimental data of Lyn [128] and to many validation studies on CFD models [122, 130] including Partially Averaged Navier Stokes models [125, 133]. RANS formulation is not able to predict the fluctuating nature of the unsteady turbulent flow [122] and Large Eddy Simulation (LES) have been found to provide results which are more adherent to experimental data. In this case, it will be shown how in the case of the model Realizable $k - \varepsilon$, the formulation PANS allows to improve the prediction obtaining results close to the LES.

The computational domain is shown in Fig. 5.2. The domain is discretized using a $(160 \times 120 \times 30)$ structured grid.

5.4. Model validation

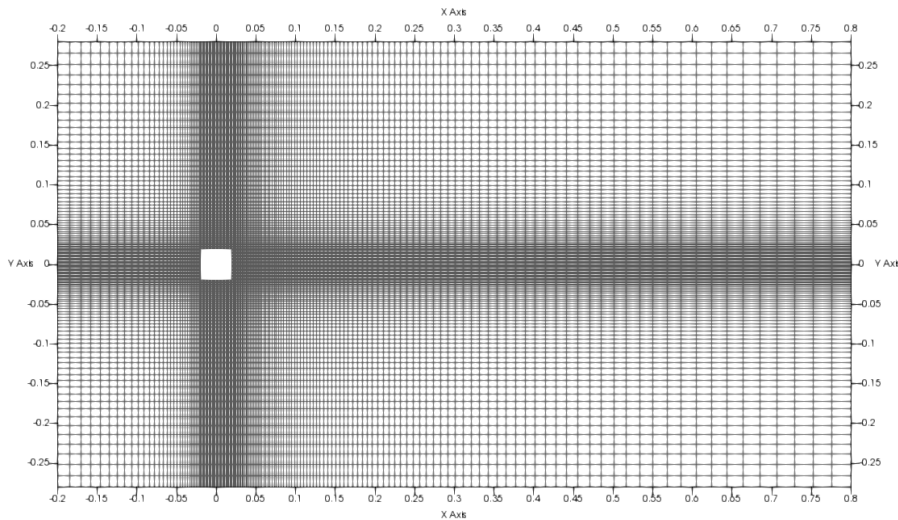


Figure 5.2: *Square cylinder: computational domain*

The first layer near-wall is kept equal to $\Delta y/D = 0.03$ for all computations in order to guarantee the same behaviour at the wall.

Results

The results of the Realizable $k - \varepsilon$ PANS model at different levels of f_K are compared with URANS, LES and experimental data.

In table 5.1, the Strouhal number, mean coefficient of drag, rms (root-mean square) of drag, rms of lift are provided, together with the length of the recirculation bubble for various cases.

In the following, the model names are shortened as follows:

- **RKE** is the Realizable $k - \varepsilon$ PANS;
- **SKE** is the Standard $k - \varepsilon$ PANS.

In Fig. 5.3, it is possible to observe that the original model Realizable $k - \varepsilon$ PANS produces an improved prediction of the averaged velocity in the recirculation zone, compared to the literature model Standard $k - \varepsilon$ PANS. For lower values of f_k , results are found to be much closer to literature.

Chapter 5. New Partially Averaged Navier Stokes model development and validation

Case	$\frac{Re}{10^3}$	St	$(C_D)_{mean}$	$(C_D)_{rms}$	$(C_L)_{rms}$	l_R/D
$k - \varepsilon$ PANS (fixed $f_k = 0.4$) Girimaji [125]	22	0.130	1.97	0.216	1.19	0.81
$k - \omega$ SST PANS Song and Park [133] A1 case	22	0.133	2.09	0.23	1.19	0.83
EXP Lyn et al. [128]	22	0.132	2.10	-	-	0.88
LES	22	0.126 - 0.132	2.03 - 2.32	0.16 - 0.20	1.23 - 1.54	0.58
Current RKE 160x120, $f_k = 0.4$	22	0.140	2.28	0.33	1.49	0.90
Current RKE 160x120, $f_k = 0.7$	22	0.124	2.23	0.19	1.51	0.69
Current RKE 160x120, $f_k = 1.0$	22	0.135	2.14	0.03	1.19	0.94
Current LES Smagorinsky 160x120	22	0.135	2.14	0.24	1.24	0.92
Current SKE 160x120, $f_k =$ 0.4	22	tbd	2.32	0.27	1.28	0.85

Table 5.1: Results on square cylinder for various cases

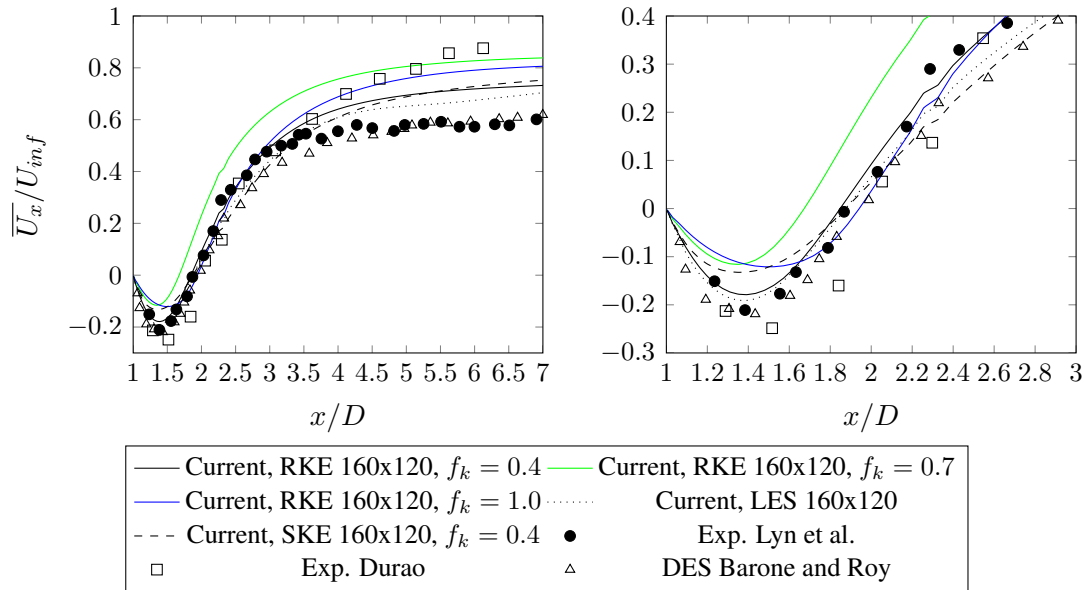


Figure 5.3: Streamwise mean velocity along the center line. Left: wake region, right: recirculation region

5.4. Model validation

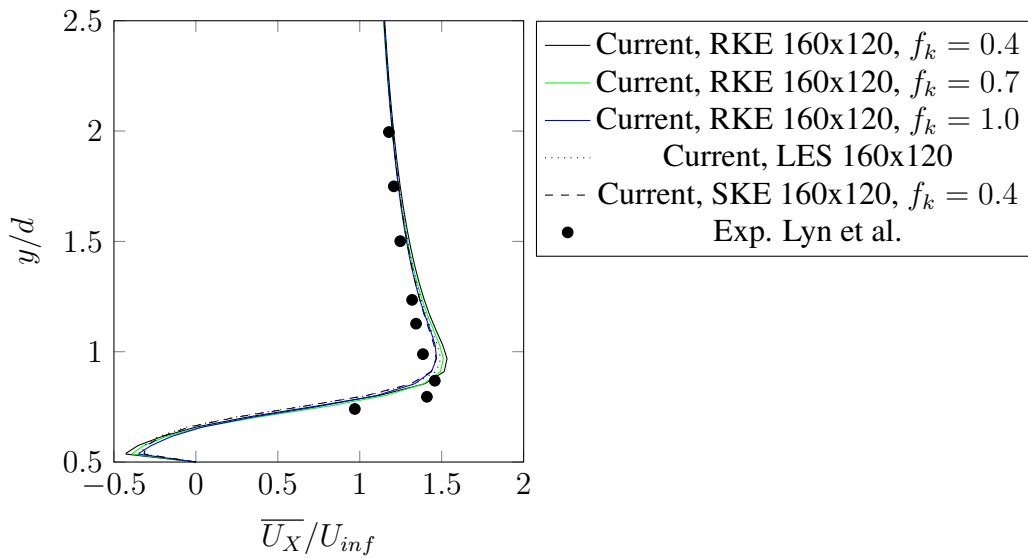


Figure 5.4: Streamwise mean velocity along vertical line at $x/D = 0.5$.

The same considerations can be done in relation to the prediction of the fluctuating rms component of the velocities, shown in Fig. 5.5 and 5.6 for the two components $u'u'$ and $v'v'$: the original model improves the prediction of the rms components compared to the Standard formulation. High values of the filter-width parameter f_k do not allow to capture the velocity fluctuations accurately, whereas lower values of f_k do.

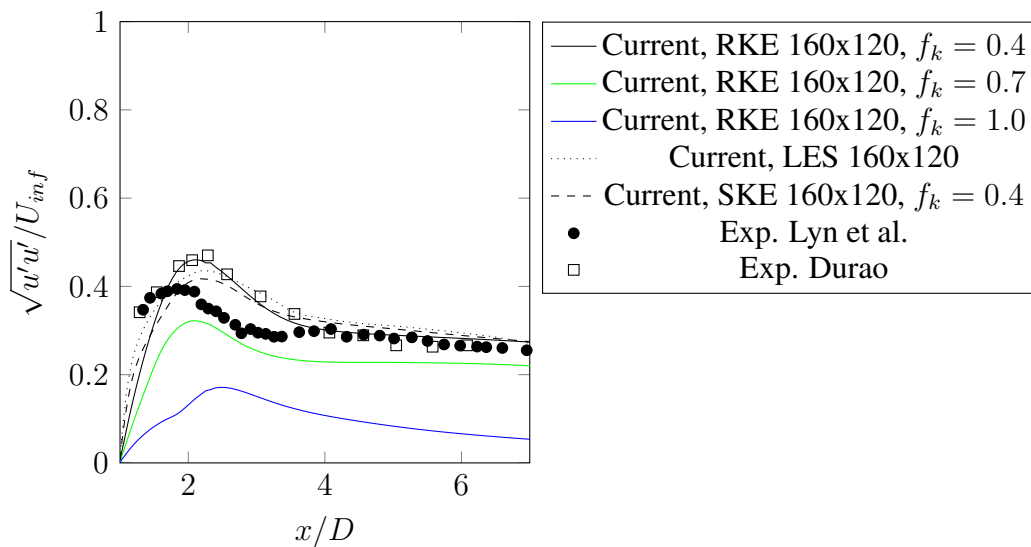


Figure 5.5: Comparison of streamwise Reynolds stress profile for different turbulence models

Chapter 5. New Partially Averaged Navier Stokes model development and validation

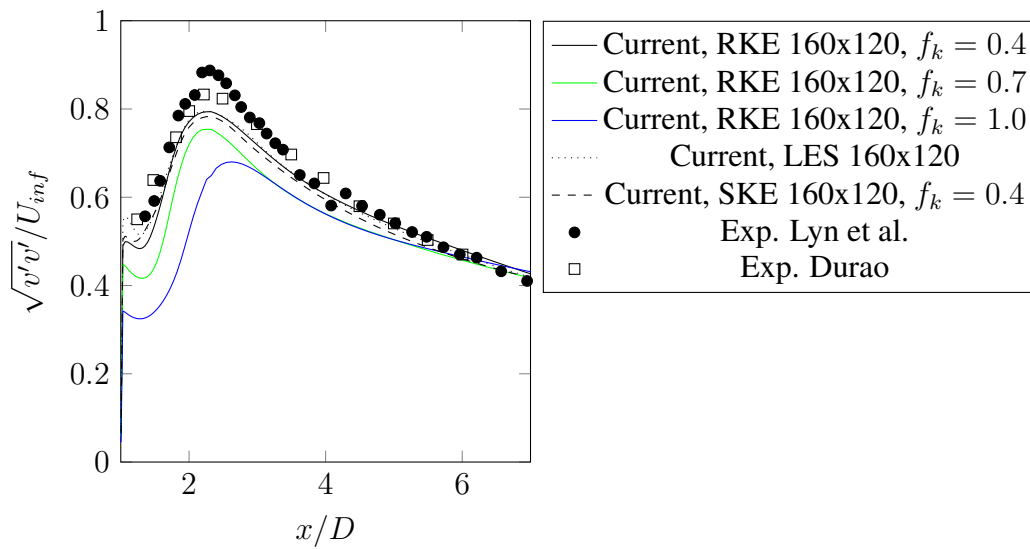


Figure 5.6: Comparison of streamwise Reynolds stress profile for different turbulence models

The comparison of the pressure coefficients along the cylinder surface is compared with the experimental data of Bearman and Obasaju [121] in Fig. 5.7.

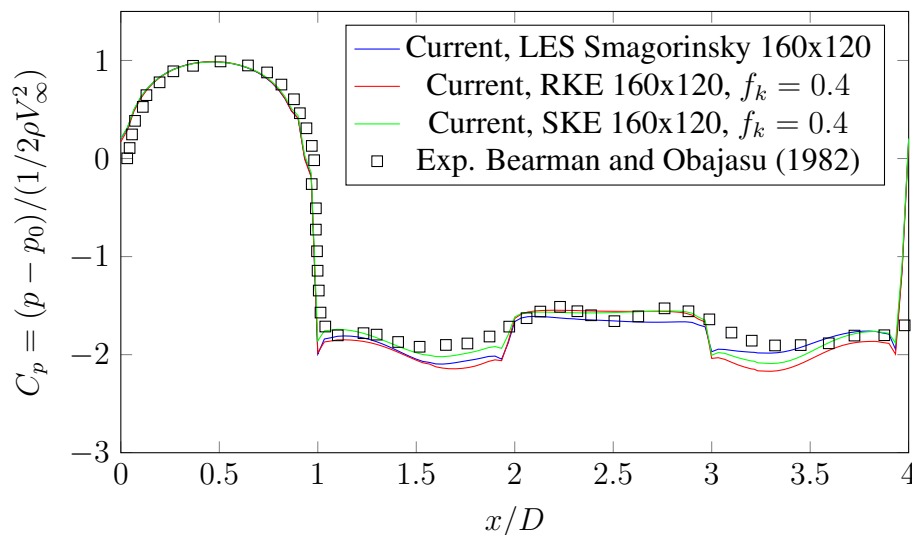


Figure 5.7: Comparison of pressure coefficients for different turbulence models

For the qualitative description of the instantaneous coherent structures, the established technique of the Q-criterion [126] is utilized. The Q-criterion defines the coherent vortical structures as the regions where the second invariant of velocity is positive.

Q is defined as:

$$Q = (\Omega_{ij}\Omega_{ij} - S_{ij}S_{ij}) / 2 > 0 \quad (5.29)$$

where $S_{ij} = (u_{i,j} + u_{j,i}) / 2$ and $\Omega_{ij} = (u_{i,j} - u_{j,i}) / 2$.

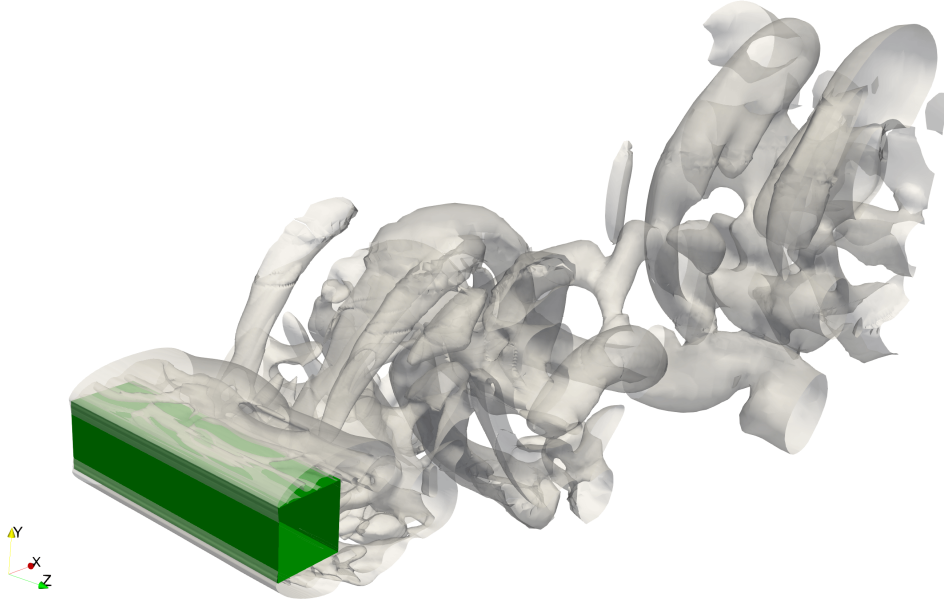


Figure 5.8: Coherent structures calculated using Q -criterion with $Q = 0.05$

In Fig. 5.8 it is possible to observe that the turbulence model is able to reproduce both the main coherent structures due to vortex-shedding (which are also identified using URANS models) and the smaller recirculation vortices, calculated by PANS thanks to the liberation of motion scales.

5.4.2 Backwards facing step

Case description

In continuation of the assessment of the $k - \varepsilon$ Realizable PANS model for complex flows, the flow past a backwards facing step is performed. The comparison is done between Realizable $k - \varepsilon$ PANS, Standard $k - \varepsilon$ PANS and experimental data. This case is chosen as a validation case for the original model $v^2 - f$ with variable C_μ PANS.

The case is based on the setup by Pitz and Daily [131] of a backwards facing step at a Reynolds number of $Re_H = U_0 H / \nu = 22000$ with $U_0 = 13.3 m/s$ and $H = 0.0254 m$. This type of flow has been analysed extensively, both numerically and experimentally.

Chapter 5. New Partially Averaged Navier Stokes model development and validation

The case of the backwards facing step is, in fact, one of the most interesting for the validation of a turbulence model as, despite its geometrical simplicity, it gives rise to many complex flow phenomena, including boundary layers, mixing layer, reattachment, flow reversal and recovery in the presence of a strong adverse pressure gradient. The case of Pitz and Daily is here studied in reference to the case of the non-reacting flow.

The computational grid is shown in Fig. 5.9.

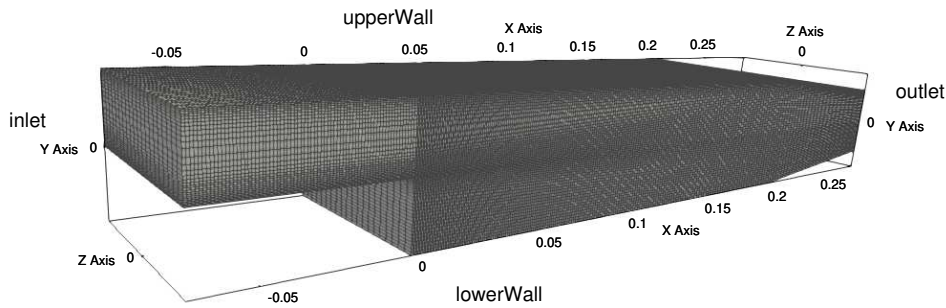


Figure 5.9: Backwards facing step computational domain

The grid is realized using a structured approach with OpenFOAM *blockMesh* tool and results in a total number of 275700 cells, which was found to be adequate for the other numerical studies for this benchmark case. At the inlet, Dirichlet conditions are applied for all variables except for pressure, for which a Neumann condition is applied with a fixed value of $p = 0$. The inlet velocity is subject to a random variation superimposed in the three directions, equal to 0.02 streamwise, and to 0.04 spanwise and normal to the flow. A no-slip condition is applied to velocity at the lower and upper walls. For the Standard $k - \varepsilon$ PANS model and the Realizable $k - \varepsilon$ PANS models the Spalding wall function is adopted, which has the following definition:

$$y^+ = u^+ \frac{1}{E} \left[\exp(\kappa u^+) - 1 - \kappa u^+ - 0.5(\kappa u^+)^2 - \frac{1}{6}(\kappa u^+)^3 \right] \quad (5.30)$$

where y^+ is the non-dimensional position, u^+ is the non-dimensional velocity, $\kappa = 0.41$ is the Von Karman constant and $E = 9.8$ is a constant. Since the $v^2 - f$ with variable C_μ is a low-Reynolds model, 10 inflation layers are added near the wall, in order to achieve a non-dimensional wall distance $y^+ \simeq 1$ in most of the walls.

The solution is performed using an incompressible segregated *PISO* (Pressure Implicit with Splitting of Operators) algorithm with second order *QUICK* divergence scheme

5.4. Model validation

for the flow variables.

The non-dimensional time-step is chosen equal to $tU/H = 0.013$, which is found to be sufficient to capture the unsteady features of the flow.

Results

The vertical profiles of mean velocity and rms velocity for Realizable $k - \varepsilon$ PANS model, $v^2 - f$ with variable C_μ PANS and the Standard $k - \varepsilon$ model are shown in figures 5.16, 5.14, 5.12.

The maximum reverse velocity is calculated accurately for most values of f_k when the PANS formulation is used, while the URANS models are not able to predict a correct value. Results are shown in Table 5.2.

Turbulence model	$f_K = 0.2$	$f_K = 0.45$	$f_K = 0.7$	URANS
Realizable $k - \varepsilon$ PANS	$0.34U_\infty$	$0.35U_\infty$	$0.32U_\infty$	$0.25U_\infty$
$v^2 - f$ with variable C_μ PANS	$0.35U_\infty$	$0.32U_\infty$	$0.33U_\infty$	$0.28U_\infty$
Standard $k - \varepsilon$ PANS	$0.32U_\infty$	$0.34U_\infty$	$0.30U_\infty$	$0.26U_\infty$

Table 5.2: Maximum reverse velocity (*Exp.*: $0.33U_\infty$)

The results in terms of reattachment length, evaluated for each turbulence models, and defined as the point in the separated region where the wall-shear stress inverts its sign, are summarized in Table 5.3. With low f_k the reattachment length is captured accurately.

Turbulence model	$f_K = 0.2$	$f_K = 0.45$	$f_K = 0.7$	URANS
Realizable $k - \varepsilon$ PANS	7.09	8.27	7.68	7.21
$v^2 - f$ with variable C_μ PANS	6.92	6.93	6.89	7.67
Standard $k - \varepsilon$ PANS	6.85	6.33	8.43	7.13

Table 5.3: Comparison of reattachment lengths x/H . $(x/H)_{exp} = 7.0$

The results are generally in good agreement with experimental data for $f_k = 0.2$ for all the three models. As f_k increases, the profiles of mean velocity are still captured but a progressive reduction in the level of the velocity fluctuations is observed for both Standard and Realizable PANS models.

At $f_k = 0.7$ the Realizable $k - \varepsilon$ model provides an improvement over the Standard $k - \varepsilon$ in the velocity fluctuations near the step. As expected, for higher f_k values, the formulation of the Realizable model are more visible.

Chapter 5. New Partially Averaged Navier Stokes model development and validation

In the URANS simulations (Fig. 5.10), which are equivalent to having $f_k = 1$, the Realizable model is still able to capture some fluctuations -even though it shows severe underestimation of U_{rms} at all stations- while the Standard $k - \epsilon$ does not calculate any. The behavior of the $v^2 - f$ with variable C_μ PANS is, on the contrary, remarkable as the filter width f_k increases: the vertical profile of the rms velocities is in fact recovered at almost all stations up to $f_k = 0.7$ and even at $f_k = 1$ (URANS solution) it is possible to observe a good prediction of the fluctuations, at a level that is unattainable with the other two models. The results are very encouraging for this model.

In analogy to the case of the square cylinder, for the qualitative description of the instantaneous coherent structures, the Q-criterion is utilized. The coherent structures generated with the three cases of filter f_k are shown in Fig. 5.17, 5.15, 5.13. It is quite evident that as the filter f_k increases from 0.2 to 0.7, only the coarser structures are captured. In the simulation with $f_k = 0.2$, it is possible to observe the development of the vortices in the mixing layer, which gradually curve towards the lower wall. The difference in velocity at the interface behind the step determines the development of large-scale coherent structures due to the Kelvin-Helmholtz instability in the shear layer.

In the following figures, a comparison is performed between different PANS turbulence models, where:

- **RV** is the $v^2 - f$ with variable C_μ PANS (original model);
- **R** is the Realizable $k - \epsilon$ PANS (original model);
- **S** is the Standard $k - \epsilon$ PANS (literature model).

5.4. Model validation

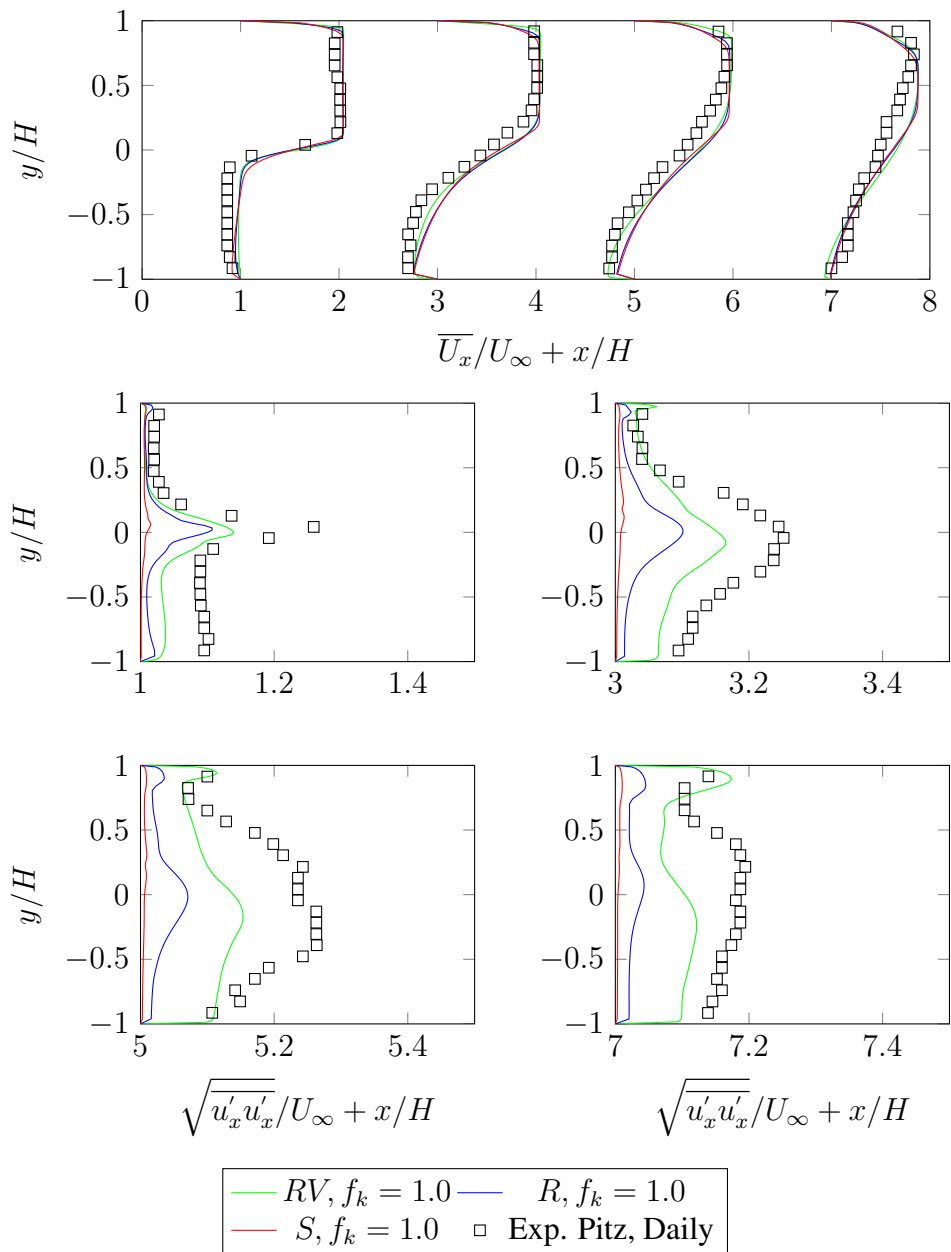


Figure 5.10: Top: streamwise mean velocity profiles behind the step. Bottom: rms velocity profiles. Comparison with $f_k = 1.0$

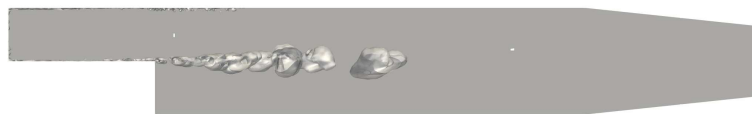


Figure 5.11: Coherent structures calculated using Q -criterion with $Q = 10000$ for URANS Realizable $k - \epsilon$

Chapter 5. New Partially Averaged Navier Stokes model development and validation

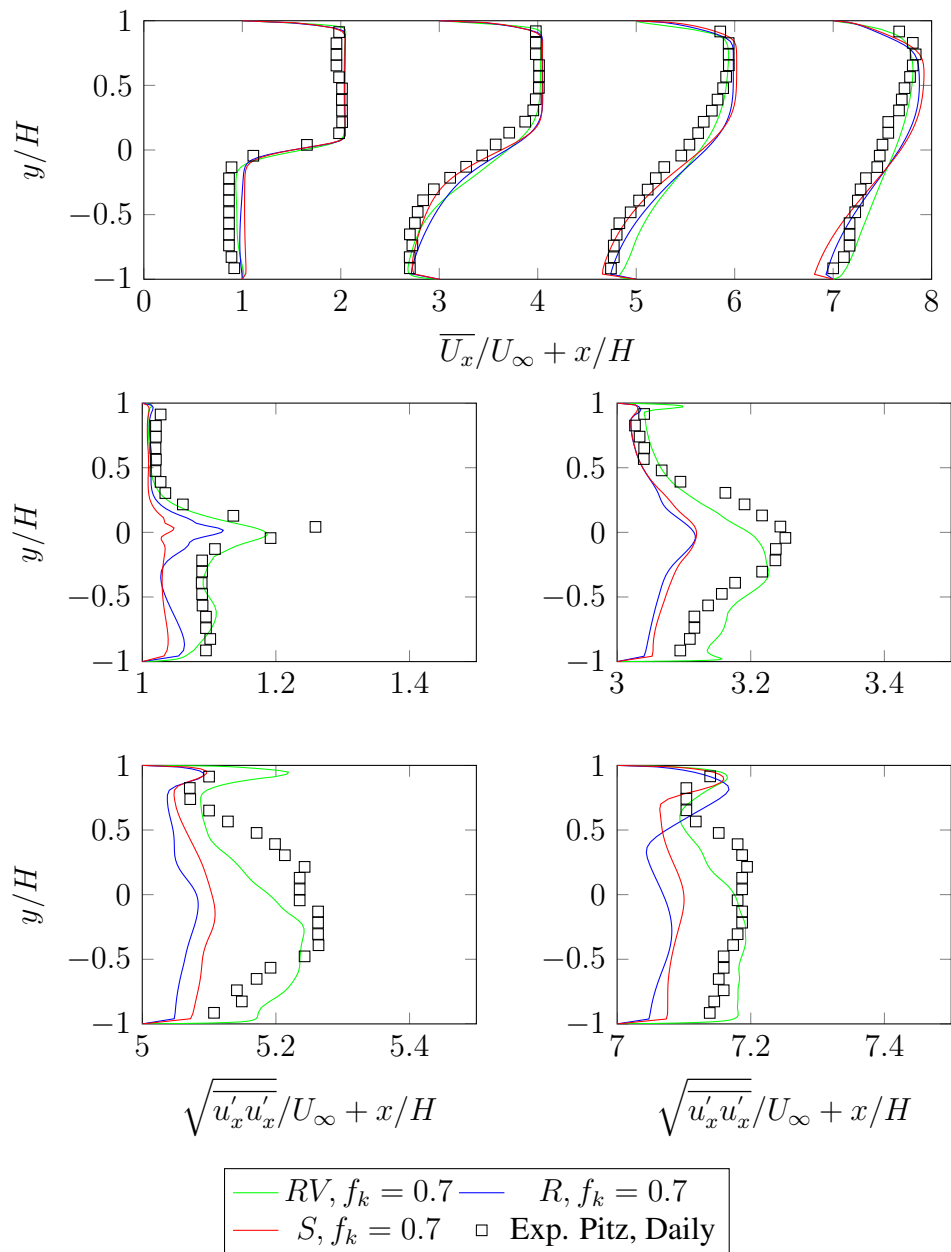


Figure 5.12: Top: streamwise mean velocity profiles behind the step. Bottom: rms velocity profiles. Comparison with $f_k = 0.7$



Figure 5.13: Coherent structures calculated using Q -criterion with $Q = 10000$ at $f_k = 0.7$

5.4. Model validation

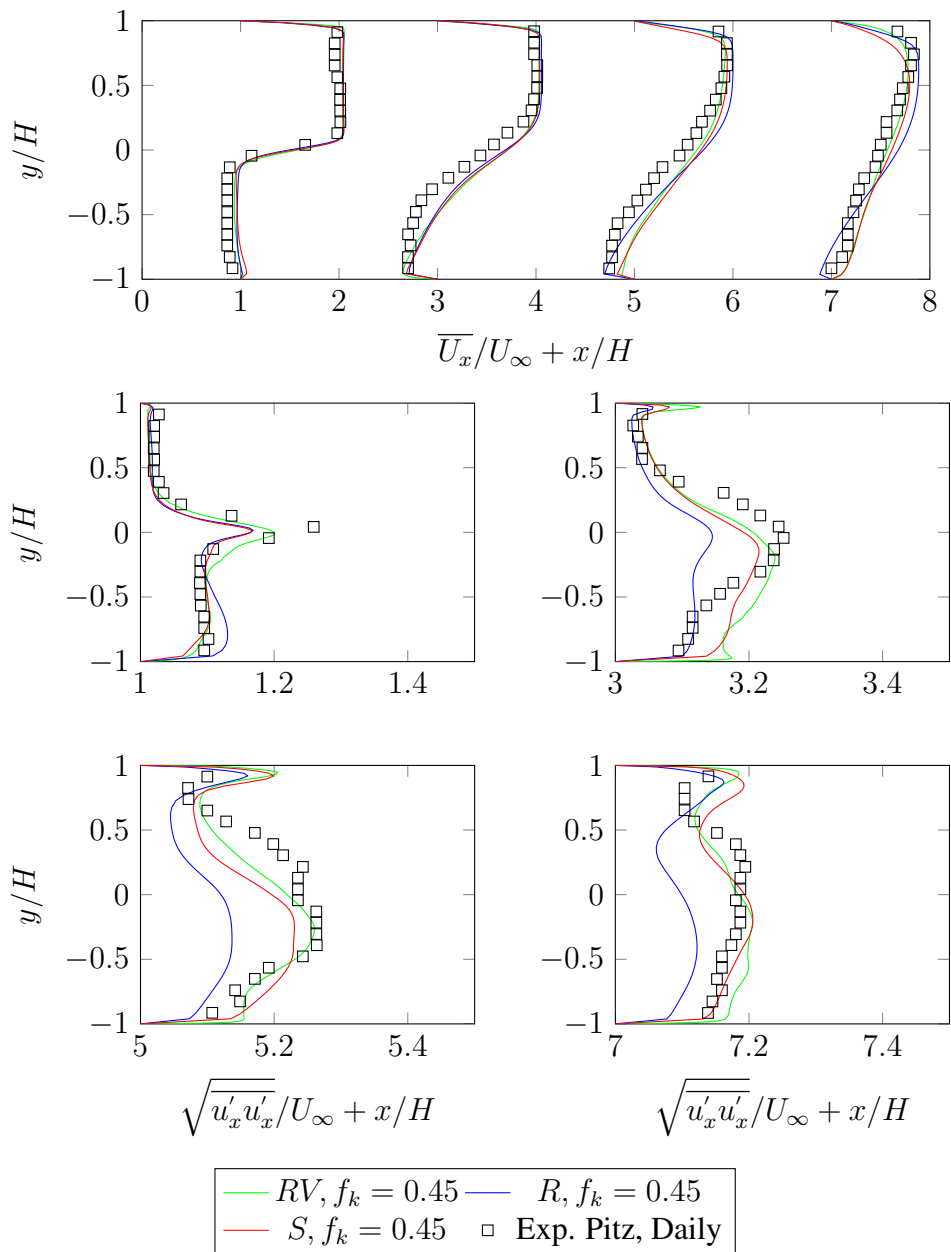


Figure 5.14: Top: streamwise mean velocity profiles behind the step. Bottom: rms velocity profiles. Comparison with $f_k = 0.45$

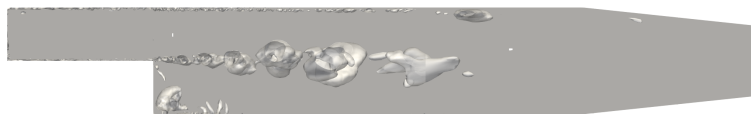


Figure 5.15: Coherent structures calculated using Q -criterion with $Q = 10000$ at $f_k = 0.45$

Chapter 5. New Partially Averaged Navier Stokes model development and validation

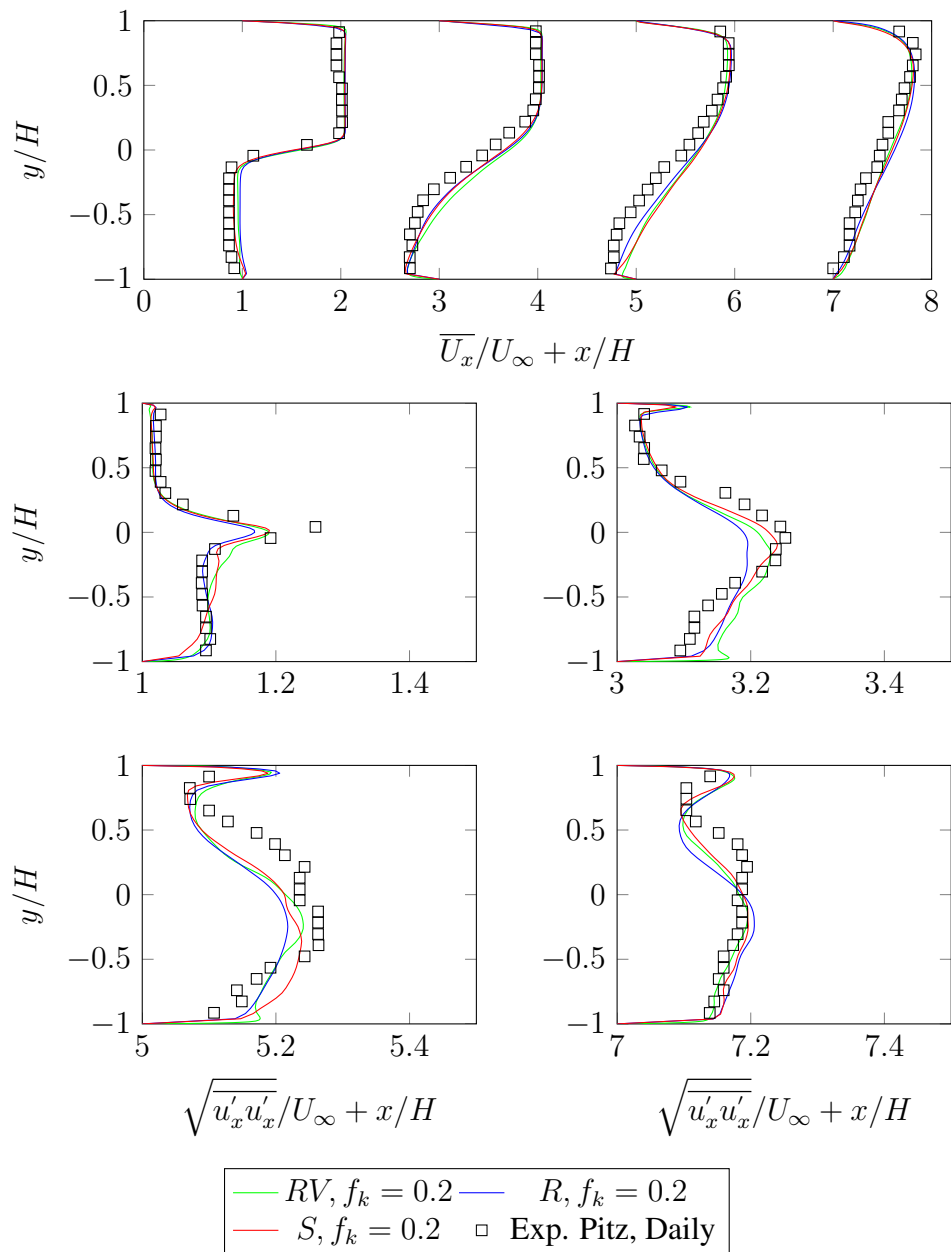


Figure 5.16: Top: streamwise mean velocity profiles behind the step. Bottom: rms velocity profiles. Comparison with $f_k = 0.2$

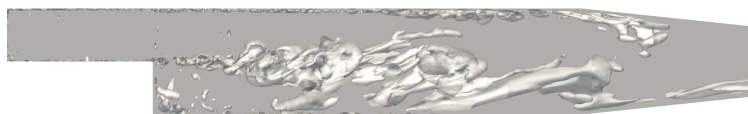


Figure 5.17: Coherent structures calculated using Q -criterion with $Q = 10000$ at $f_k = 0.2$

5.5 Conclusions and future developments

In the current chapter the development of two new turbulence models which follow the PANS paradigm is presented. The two models, the Realizable $k-\varepsilon$ PANS and the v^2-f with variable C_μ PANS have been developed theoretically, implemented in OpenFOAM open source CFD environment and tested in typical benchmark cases. The results here obtained are encouraging compared to the simple $k-\varepsilon$ PANS model, especially for the second model. In fact the superior formulation of the v^2-f model compared to the Standard $k-\varepsilon$ emerged during the test of the backwards facing step, where the new model was successful in determining the evolution of velocity fluctuations along the fluid domain even at high values of filter f_k . This means that this model would be expected to provide a good representation of fluctuating coherent structures not only when the computational grid is fine and low values of f_k can be achieved, but also for coarse grids.

Since the PANS approach was presented by Girimaji in 2006, this new method has found several applications and has started to become a viable alternative to LES for the simulation of fluctuating fields. The ability of PANS models to provide robust results at reduced computational cost compared to LES is already established in literature (for example, Mirzaei [129] have shown a 35% reduction in computational cost of PANS compared to LES). Among the future developments of this study, there is the need to quantify the actual advantage in the calculation times of the PANS models developed here compared to the LES models. This was not discussed in the present analysis as all the studies were carried out on the same grid. To highlight the difference between the calculation times, it will be necessary to carry out a sensitivity analysis of the results with respect to the grid to evaluate the different levels at which it is achieved with the various models.

At the moment, there are still open topics regarding PANS such as a consistent definition of a space and time variable coefficient f_k and, in general, the application of PANS to different applications. In relation to application of PANS to the transient simulation of wind loads on large structures, still no application of PANS has been shown in literature so far. Among the points that need to be addressed, perhaps the main one for this type of application is the utilization of boundary conditions representative of the atmospheric boundary layer which are able to develop a vertical profile of velocity and turbulent intensity along the computational domain. The extension of the PANS models to the problems of environmental flow modelling therefore represents a natural future development for the research presented here. Considering the qualities of

Reference

simplicity, robustness and computational efficiency of these models, developments in this direction may make the PANS approach a reference in environmental wind flow modelling.

5.6 Reference

- [120] Branislav Basara, Siniša Krajnovic, Sharath Girimaji, and Zoran Pavlovic. Near-Wall Formulation of the Partially Averaged Navier Stokes Turbulence Model. *AIAA Journal*, 49(12):2627–2636, 2011.
- [121] P W Bearman and E D Obasaju. An experimental study of pressure fluctuations on fixed and oscillating square-section cylinders. *Journal of Fluid Mechanics*, 119:297–321, 1982.
- [122] G Bosch and W Rodi. Simulation of Vortex Shedding Past a Square. *International journal for numerical methods in fluids*, 616(October 1997):601–616, 1998.
- [123] Lars Davidson, Peter V Nielsen, and Andreas Sveningsson. Modification of the ν^2 -f Model for Computing the Flow in a 3D Wall Jet. *Turbulence, Heat and Mass Transfer*, 4:577–584, 2003.
- [124] Hosein Foroutan and Savas Yavuzkurt. A partially-averaged Navier-Stokes model for the simulation of turbulent swirling flow with vortex breakdown. *International Journal of Heat and Fluid Flow*, 50:402–416, 2014.
- [125] Sharath Girimaji and Khaled Abdol-Hamid. Partially-Averaged Navier Stokes Model for Turbulence: Implementation and Validation. *43rd AIAA Aerospace Sciences Meeting and Exhibit*, (January):1–14, 2005.
- [126] Jinhee Jeong and Fazle Hussain. On the identification of a vortex. *Journal of Fluid Mechanics*, 285(February 2015):69–94, 1995.
- [127] Fue Sang Lien and Georgi Kalitzin. Computations of transonic flow with the ν^2 -f turbulence model. *International Journal of Heat and Fluid Flow*, 22(1):53–61, 2001.
- [128] DA Lyn, S Einav, W Rodi, and JH Park. A laser-Doppler velocimetry study of ensemble-averaged characteristics of the turbulent near wake of a square cylinder. *Journal of Fluid Mechanics*, 304:285–319, 1995.

- [129] Maryam Mirzaei, Siniša Krajnović, and Branislav Basara. Partially-Averaged navier-stokes simulations of flows around two different ahmed bodies. *Computers and Fluids*, 117:273–286, 2015.
- [130] S Murakami and A Mochida. On turbulent vortex shedding flow past 2D square cylinder predicted by CFD. *Journal of Wind Engineering and Industrial Aerodynamics*, 54-55(C):191–211, 1995.
- [131] Robert W Pitz and John W Daily. Combustion in a Turbulent Mixing Layer Formed at a Rearward-Facing Step. *AIAA Journal*, 21(11):1565–1570, 1983.
- [132] Tsan-Hsing Shih, William W Liou, Aamir Shabbir, Zhigang Yang, and Jiang Zhu. A new k-epsilon eddy viscosity model for high reynolds number turbulent flows - model development and validation. *Computers & Fluids*, 24(3):227–238, 1995.
- [133] Chi-su Song and Seung-O Park. Numerical simulation of flow past a square cylinder using Partially-Averaged Navier–Stokes model. *Journal of Wind Engineering and Industrial Aerodynamics*, 97(1):37–47, 2009.

CHAPTER 6

Application: wind-induced fatigue calculation of a stadium roof

6.1 Highlights

In the present chapter, the procedure outlined in Chapter 4 is applied, considering the new AEK Stadium in Athens, fabricated and built by Cimolai S.p.A., as case study. The aim of the chapter is to provide the reader with a detailed description of each aspect of the procedure and a constant critical discussion on the obtained results. The focus is given to a steel connection with welded joints in order to emphasize all the relevant aspect of the phenomena.

This chapter is not intended, however, to provide an assessment of the structural performance of the structure taken as a case study, of which only one connection is arbitrarily chosen, and analyzed with the sole purpose of presenting the calculation method for wind-induced fatigue.

The description of the fatigue assessment is preceded by a brief description of the roof structure and its dynamic properties.

6.2 Case study

The stadium's roof structure, shown in Fig. 6.1 is a cantilever roof and consists of 4 main trusses which extend between concrete columns. Two long trusses have a span of 140 m and 2 short trusses have a span of 90 m. Secondary beams are mounted on top of the main trusses and are supported by lateral concrete stands. The primary trusses are connected by a hanging system to the concrete columns while the secondary beams (rafters) are linked to each other by means of ring beams (one inner, one outer and two internal ones).

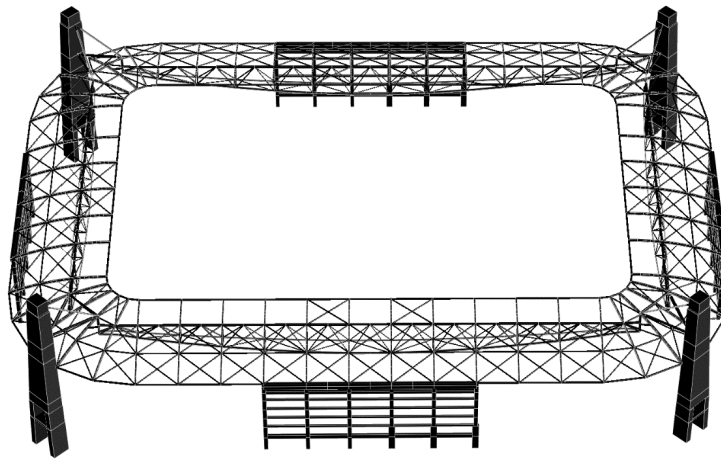


Figure 6.1: *Roof structure of the AEK Stadium in Athens*

The vertical loads are in part transferred to the concrete columns through the hanging system (with a strut-and-tie resistance system, see Fig. 6.2) and in part transferred from the rafter to the outer ring beam, which is supported by the concrete stands. A bracing system transfers horizontal loads partly to the ring beams and partly to the rafters.

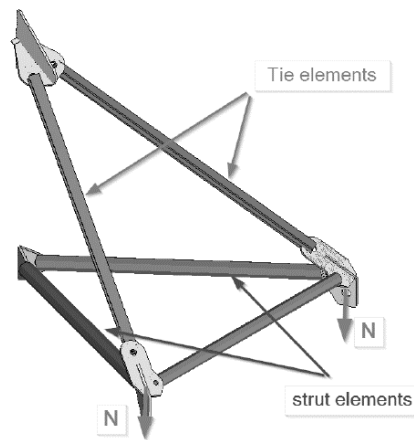


Figure 6.2: *Strut-and-tie behaviour of the hanging system*

The restraints of the roof, located in correspondence of the lateral stands, are shown in Fig. 6.3. The restraints are mono-directional vertical supports, except for two supports on each side that are bi-directional and react vertically and horizontally, parallel to the roof side.

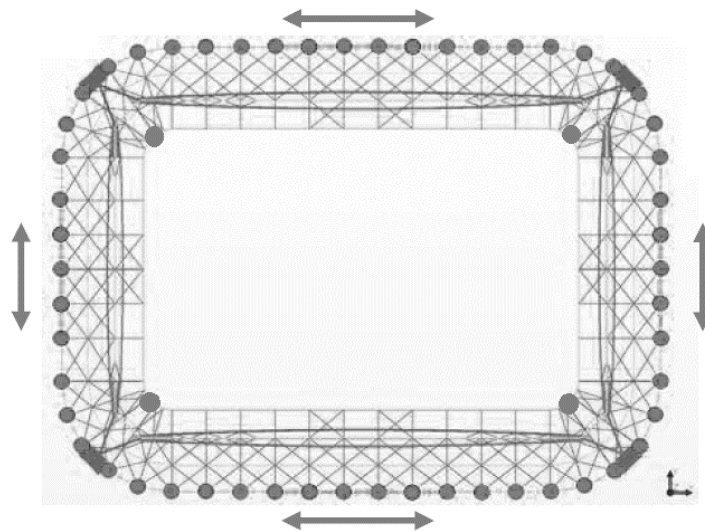


Figure 6.3: *Layout of the restraints*

The roof cladding is made with pre-tensioned membranes. Each membrane is located between two adjacent rafters and covers a dimension of about 10 x 25 m. A double-curved surface is realized for the membranes thanks to a system of intermediate arches, also providing additional stiffness to the secondary structure for sustaining wind and snow pressure loads.

Chapter 6. Application: wind-induced fatigue calculation of a stadium roof

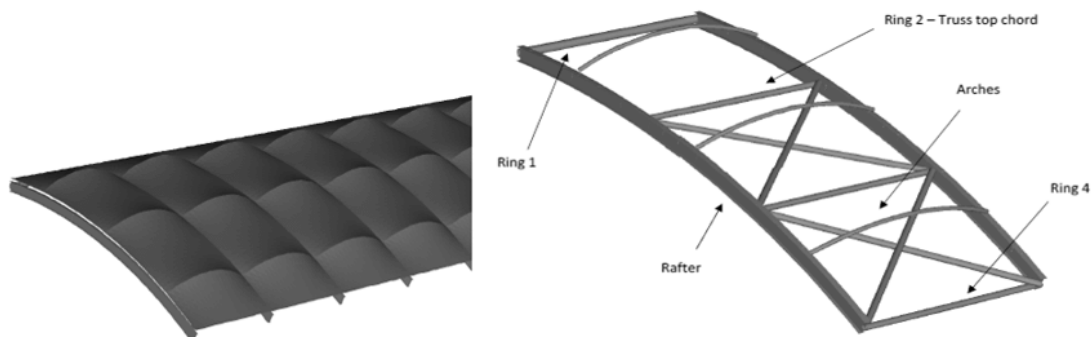


Figure 6.4: *Membrane roof system*

The main trusses are characterized by triangular cross-section (Fig. 6.5) composed by a CHS profile on top chords (with section 610x30), a T profile on both bottom chords (with section 600x45x35), and CHS profiles for bracings. The truss exhibits variable height over its length with a maximum extension at midspan, equal to 7.7 m for the long trusses and 5.7 m for the short trusses. A set of inclined struts provides torsional restraints for the main trusses. The rafters are curved built-up I sections, having a variable height and almost 25 long.

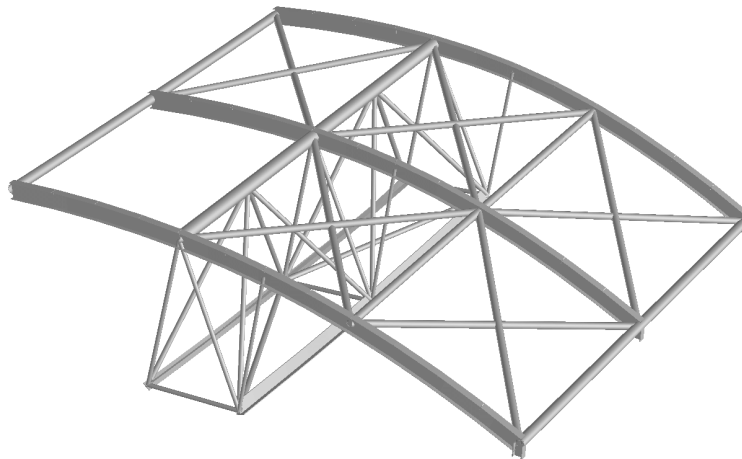


Figure 6.5: *Main truss and rafter system*

A typical connection of the main truss is shown in Fig. 6.6. The connection contains both bolted and welded joints.

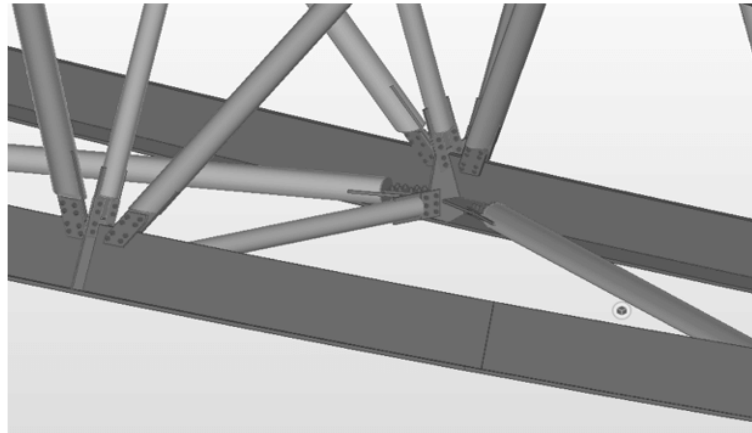


Figure 6.6: *Main truss typical joint*

6.3 Dynamical properties

A modal analysis is conducted based on the structure's Finite Element model, in which all the structural elements have been modelled as beam elements. In addition to the structural mass, non-structural masses have been considered, including the weight of the catwalks hanged on the roof and of the corners connections.

The first two natural frequencies are equal to 0.84 Hz and 0.88 Hz, respectively, and are associated with the motion of the two long sides of the roof cantilevers. The 4th and 5th modes, respectively at 1.12 Hz and 1.17 Hz, are instead associated to the cantilever motion of two short sides. The modal shapes for modes 1 and 5 are shown in Fig. 6.9. The low frequency values and the modal shapes make these modes significant for the wind response.

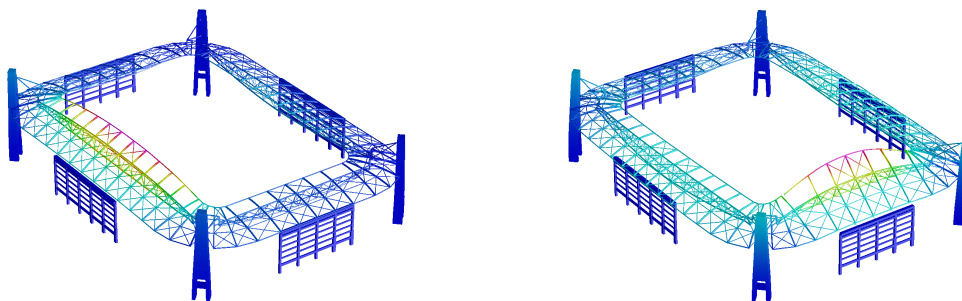


Figure 6.7: *First cantilever modes of a long roof side (Mode 1) and of a short roof side (Mode 5)*

The 6th and 9th modes, at 1.19 Hz and 1.34 Hz, are linked to the asynchronous mo-

Chapter 6. Application: wind-induced fatigue calculation of a stadium roof

tion of two concrete columns, while the 7th mode, at 1.29 Hz, relates to a synchronous motion of all the columns (6.8).

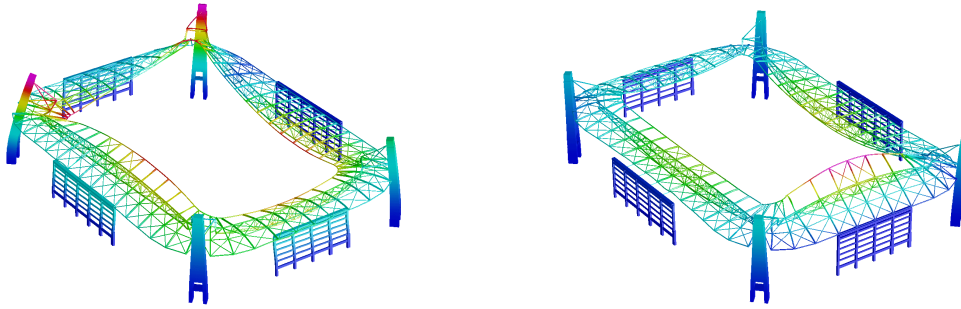


Figure 6.8: *Examples of low frequency global modes (Mode 6 and 7)*

Other modes that are expected to have an interaction with wind action are the anti-symmetric flexural modes such as the 17th and 19th modes at 2.12 Hz and 2.17 Hz for the long side and the 33th and 34th at 2.73 Hz and 2.78 Hz.

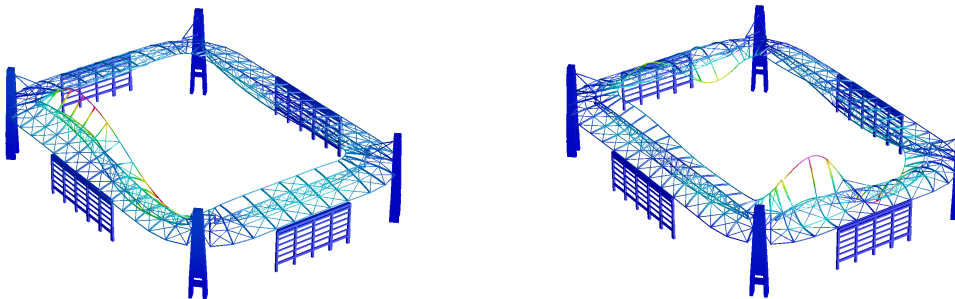


Figure 6.9: *Local anti-symmetric mode of a long roof side (Mode 17) and of a short roof side (Mode 34)*

The effective number of relevant modes for the evaluation of the buffeting response is quite limited and is not expected to exceed a number of 15. For this particular case, the solution of the dynamic equations can thus be performed with the use of the modal superposition technique. This evaluation of the relevant modes could be avoided if a direct integration technique is performed. This approach would be necessary in cases where a higher number of modes needs to be considered.

6.4 Statistical analysis of wind data

The wind climate analysis has been carried out based on the data provided by the National Observatory of Athens (NOA) relative to the anemometer in Thissio, which is located at 10 Km from the building site.

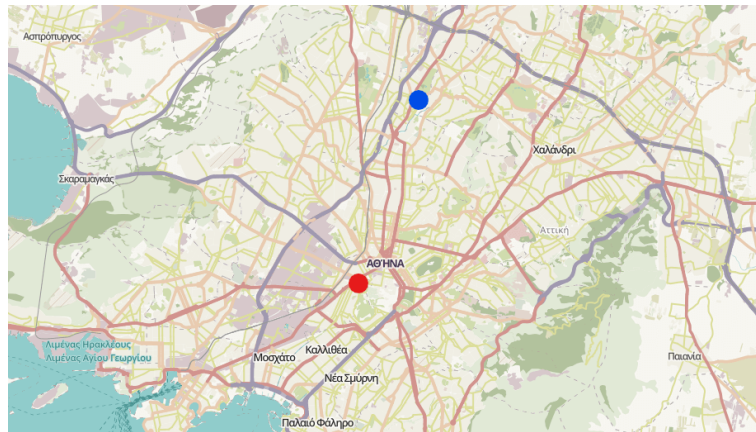


Figure 6.10: Location of the station (red dot) and building site (blue dot) (Map from OpenStreetMap)

The measurements are recorded by an anemometer at 10 m elevation on the top of the hill and represent an hourly mean wind speed and direction that has been collected for nearly 30 years. The number of directional sectors is $S = 16$. As shown in Fig. 6.11, the ground roughness z_0 in the surroundings of the anemometer can be associated to a ground Category II only in the sectors within the dotted lines. Category III ($z_0 = 0.3$) is, on the contrary, associated to the other areas.

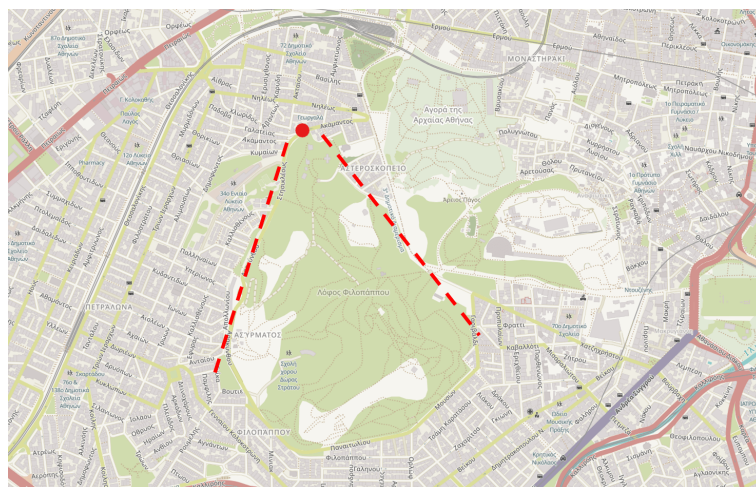


Figure 6.11: Ground roughness on the surroundings of the station site (red dot) (Map from OpenStreetMap)

Chapter 6. Application: wind-induced fatigue calculation of a stadium roof

Wind speeds coming from the latter sectors have thus been amplified by a coefficient $k = 1.33$ to normalize them to ground Category II. Table 6.1 shows the correction factor considered for each wind direction.

Sector	z_0	k
N	0.3	1.33
NNE	0.3	1.33
NE	0.3	1.33
ENE	0.3	1.33
E	0.3	1.33
ESE	0.05	1
SE	0.05	1
SSE	0.05	1
S	0.05	1
SSW	0.05	1
SW	0.3	1.33
WSW	0.3	1.33
W	0.3	1.33
WNW	0.3	1.33
NW	0.3	1.33
NNW	0.3	1.33

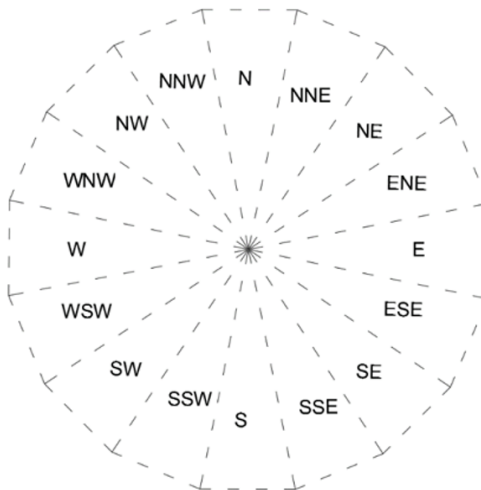


Table 6.1: Conversion factor of the recorded wind speeds based on the ground roughness for each statistical direction

6.4. Statistical analysis of wind data

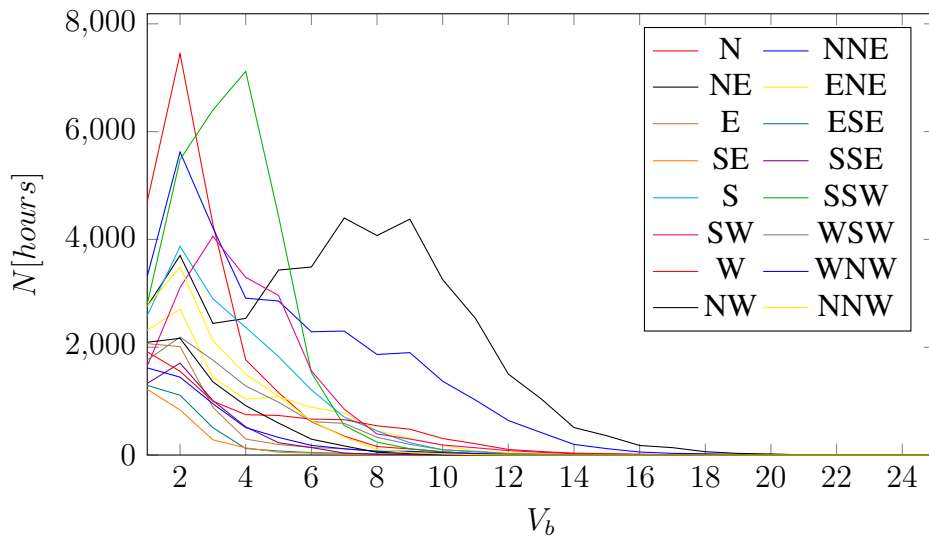


Figure 6.12: Joint occurrence of wind speeds and sectors

The collected data have then been fitted using a Hybrid Weibull model, as detailed in Chapter 4. The following tables show the fitting results for all the sectors, while the corresponding Weibull parameters k and c are shown in Table 6.2.

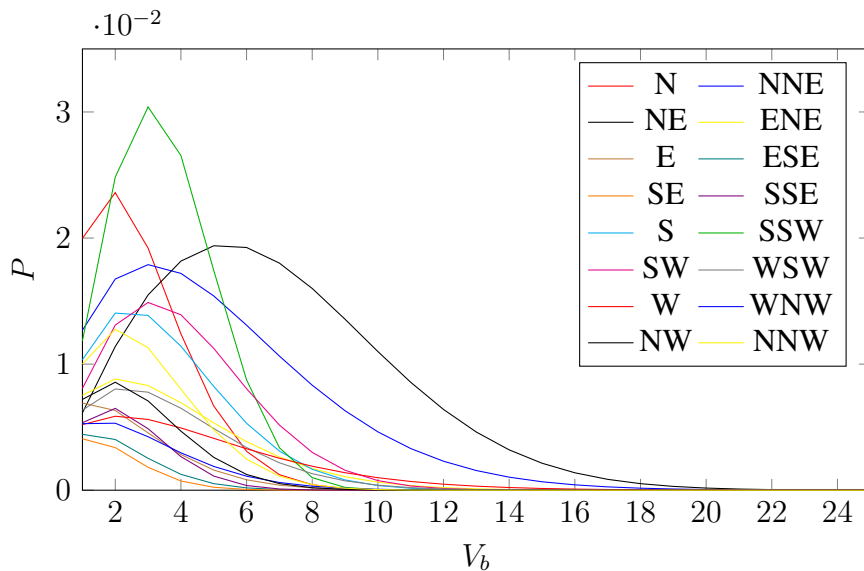


Figure 6.13: Fitting of wind data to Weibull distribution curves

The presence of preferential sectors is clear in Fig. 6.13. Most of the time, wind is acting in the North-Eastern sectors (NNE and NE sectors), and these sectors are also associated to high wind speeds. Also, the West sector is characterized by a high

Chapter 6. Application: wind-induced fatigue calculation of a stadium roof

Sector	k	c
N	1.74	3
NNE	1.58	5.73
NE	1.97	7.72
ENE	1.54	4.19
E	1.46	2.72
ESE	1.61	2.34
SE	1.64	2.09
SSE	1.87	2.72
S	1.75	3.92
SSW	2.31	3.91
SW	1.92	4.55
WSW	1.64	4.09
W	1.42	4.93
WNW	1.48	3.15
NW	1.73	3.06
NNW	1.78	3.29
SW	1.92	4.55
WSW	1.64	4.09

Table 6.2: Weibull parameters for each direction

scale factor ($c \simeq 5m/s$), and thus a high probabilities of occurrence is associated to the stronger winds speeds. This becomes even clearer by observing the polar representation of the joint probability distribution of wind speeds and sectors in Fig. 6.14. The contour lines represents equal wind speed's probability of exceedance. The sectors associated with the North-East sector are the only fatigue-relevant sectors at high exceedance probabilities, i.e. 0.1 percent. However, as the probability of exceedance decreases, wind sectors due to the West sector become more and more relevant. This effect is, again, a consequence of the corresponding very high value of scale factor.

6.4. Statistical analysis of wind data

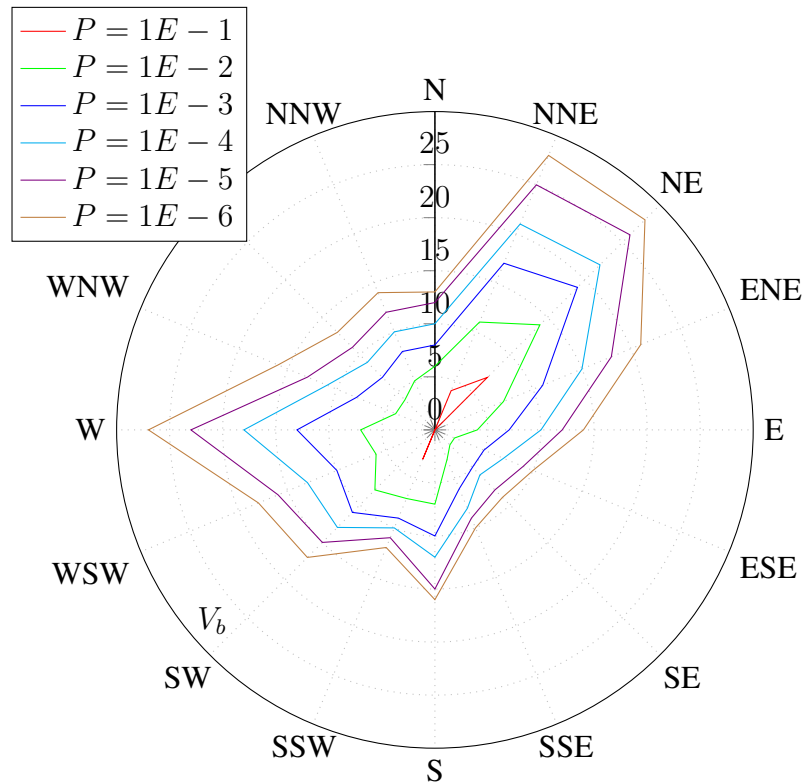


Figure 6.14: Polar representation of the joint probability distribution of wind speeds and sectors

Joint occurrences of wind speeds and directional sectors are then corrected considering the two following requirements:

- The directions in which the model was tested in the wind tunnel must match the directional sectors;
- the results are referred to the basic wind speeds V_b at 10 m height in a terrain category II, and therefore, based on the site roughness coefficient z_0 and on the mean wind profile, they must be referred at the roof height $h = 25.5m$.

The orientation of the stadium with respect to each of the directional sectors and obtained from the statistical analysis and the 8 selected directions considered from the wind tunnel test (see following Section) is shown in Fig. 6.15.

Chapter 6. Application: wind-induced fatigue calculation of a stadium roof

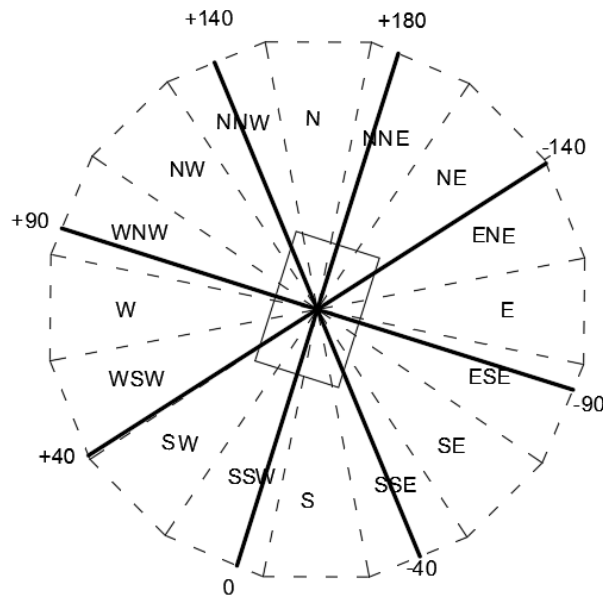


Figure 6.15: Matching between statistical directional sector and simulated directions

The three fatigue relevant sectors, namely NNE, NE, W, are thus converted into three fatigue relevant directions, i.e. 180, -140, +90.

The wind speed at the roof reference height is obtained by means of the mean wind profile given by EN 1991-1-4:

$$V(z_{ref}) = V_b k_r \ln \left(\frac{z_{ref}}{z_0} \right) \quad (6.1)$$

where:

$$k_r = 0.19 \left(\frac{z_0}{z_{0,II}} \right)^{0.07} \quad (6.2)$$

and z_0 is the site roughness, assumed equal to 1. The results of the statistical analysis are summarized in Fig. 6.16, where the joint number of occurrence (hours) of each mean wind speed at the roof reference height and directions of analysis is shown.

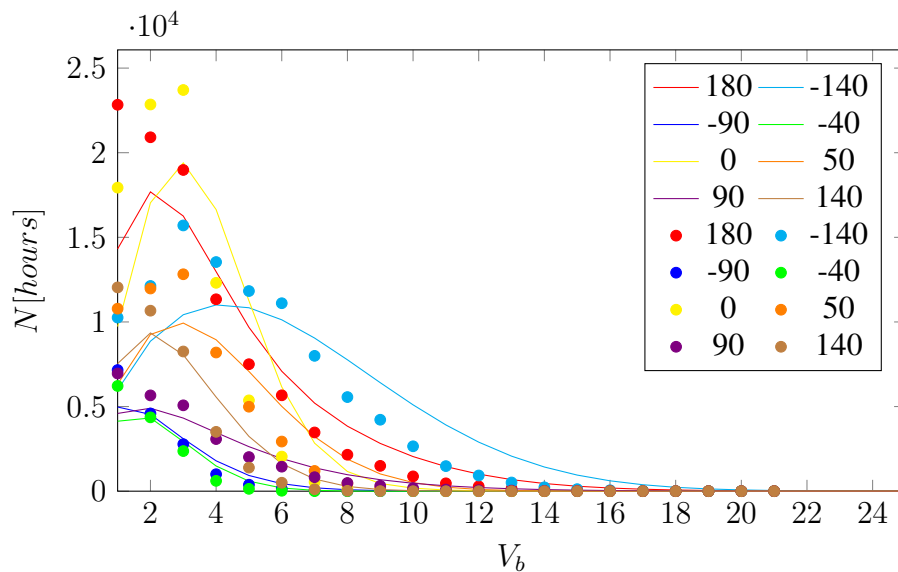


Figure 6.16: Number of hours of occurrence of basic wind speeds (continuous line) and of wind speeds at the roof height (dots) for each simulated direction

The higher mean wind speed considered is 21 m/s; this occurs for 12, 42 and 72 minutes in 50 years, respectively, in the direction +90, 180, -140.

6.5 Wind simulation

6.5.1 Wind Tunnel Test

The Wind Tunnel Tests on the AEK stadium have been carried out in the boundary layer test section of the Politecnico di Milano on a 1/120 rigid model of the structure. The general view of the model is shown in Fig. 6.17, together with the surrounding and the turbulence generators, while Fig. 6.18 shows a detail view of the model.

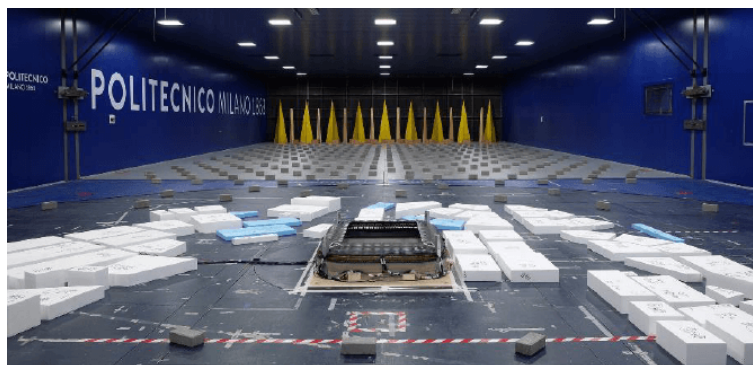


Figure 6.17: BLWT of the Politecnico di Milano with AEK model

Chapter 6. Application: wind-induced fatigue calculation of a stadium roof



Figure 6.18: *Model of the AEK stadium*

The simulation of the wind loading were performed considering a velocity scale $\lambda_v = 3$. With reference to the roof reference height, the full-scale mean wind speed, equal to 20.5 m/s, becomes equal to 6.8 m/s at the model scale. The pressure measurements were carried out for 36 wind directions spaced 10 degrees apart with the use of 250 pressure taps and using high-speed scanning pressure whose frequency of resolution is 500 Hz. The distribution of pressure taps over the model and the corresponding tributary areas, whose dimensions are almost 10 x 10 m in prototype scale, are shown in Fig. 6.19.

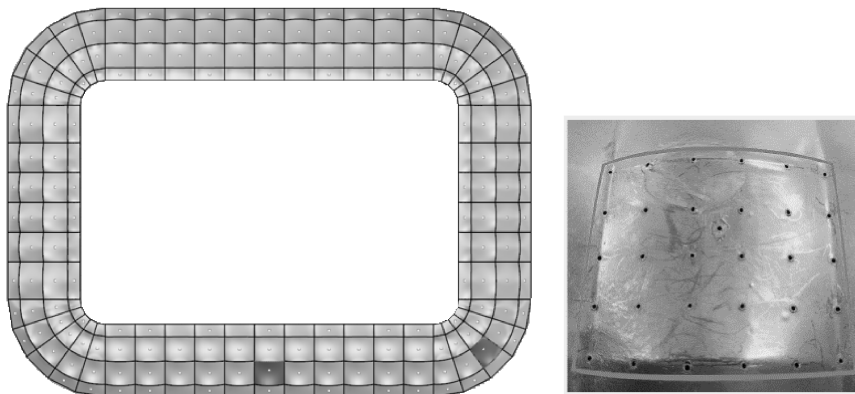


Figure 6.19: *Layout of the pressure taps over the roof and detail view of the high-density panel*

The wind tunnel engineers obtained the admittance functions for all the incoming wind directions by covering two areas, shown in Fig. 6.19 with high taps density. Fig. 6.20 shows the experimental admittance functions, plotted against the reduced frequency $f^* = fL/V$. $L = 9.2m$ is the effective length, obtained experimentally on the basis on the observed spatial correlation between mutual pressure fluctuations on the panel with high density of pressure taps. The absence of Reynolds number effects has also been proved by performing a second simulation test at a reduced wind speed,

equal to about 4.5 m/s at the roof height.

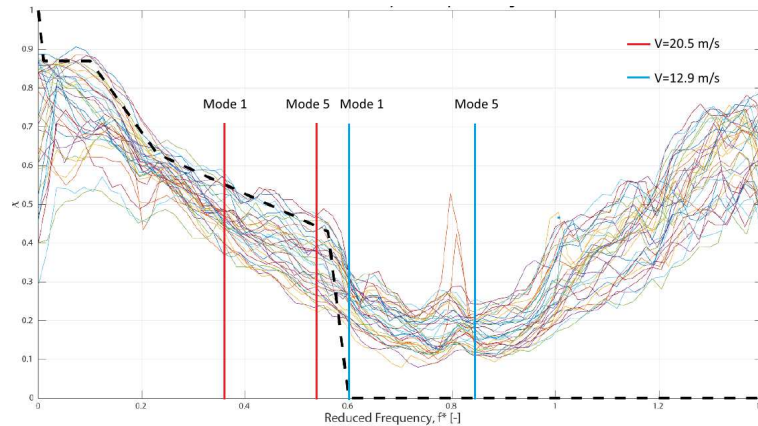


Figure 6.20: *Experimental admittance functions and ULS envelope*

The dashed line in Fig. 6.20 represents the envelope filter considered for determining the Ultimate Limit State (ULS) wind loading, used for the dimensioning of the structural elements. The use of a single admittance function for the whole roof area represents a conservative approach as it corresponds to using an envelope admittance function. The use of a single admittance function is equivalent to assuming that the correlation of the pressure fluctuations is the same all along the roof and for all the wind-incoming directions. In doing so, the effective spatial correlation structure of the wind field is not rigorously reproduced. However, unless the roof is covered with a larger number of panels with high density of pressure taps, this approach seems the only possible way to deal with the problem of modelling the spatial correlation of pressures recorded from the WTTs. This would allow to perform a matching among the recorded pressure taps so as to assign a different admittance function for each tributary area and wind direction

In the same figure, the values of reduced frequencies associated to the structural modes are represented by the solid lines. A cut-off of the aerodynamic admittance function at a reduced frequency equal to 0.6 can be observed. The main reasons for this cut-off are the following:

- The frequencies in the range $[1.4; 2.2]$, i.e. the ones associated to reduced frequencies in the range $[0.6; 1]$, are not relevant in ULS perspective since the main resonant modes are well captured;
- The correlation between pressure fluctuations in the range $[1.4; 2.2]$ is found to be quite negligible.

Chapter 6. Application: wind-induced fatigue calculation of a stadium roof

The second aspect is also a consequence of the adopted velocity scale $\lambda_V = 3$. The minimum velocity scale that leads to the maximum velocity at the scale model which allows for an accurate evaluation of all the pressure fluctuations whose frequencies are lower than a given value f_p can be further evaluated:

$$\lambda_V \geq \frac{\lambda_L f_p}{\alpha f_{res}} \geq \frac{\lambda_L V_p f^*}{\alpha f_{res} L_p} \quad (6.3)$$

Where the variables are defined in Section 4.2. By inverting the approach, it is possible to evaluate the last reduced frequency whose response is considered:

$$f_{max}^* = \frac{\alpha f_{res} L_p \lambda_V}{\lambda_L V_p} = \frac{1/10 \cdot 500 \cdot 9.2 \cdot 3}{120 \cdot 20.5} \simeq 0.6 \quad (6.4)$$

where it is assumed $\alpha = 1/10$. It should be noted that for reduced frequencies higher than 0.6 the signal of the wind pressure fluctuations is less and less accurate, up to a value $f^* = 2.5$ ($\alpha = 1/4$) after which the signal ceases to have any content due to pressure taps sensitivity. Therefore, the quite low correlation structure of the wind pressure for reduced frequencies in the range $[0.6; 1]$ also derives from the adopted velocity scale. By considering $f^* = 1$, the resulting minimum velocity scale would have resulted to be $\lambda_V \simeq 5$ ($V_m \simeq 4\text{m/s}$). A possible compromise would have been the choice a velocity scale equal to $\lambda_V \simeq 4$ ($V_m \simeq 5\text{m/s}$); the independence in relation to Reynolds number effects for this wind speed would still be guaranteed.

In the perspective of performing a wind-induced fatigue analysis, the cut-off of the experimental admittance functions at a reduced frequency $f^* = 0.6$ appears to be a relevant assumption, which could result in an underestimation of the number of cycles associate to lower wind velocities. In particular, with this cut-off limit, all the stress cycles associated to wind speeds lower than 12 m/s could not be captured, as, at 12 m/s the reduced frequency associated to the Mode 1 is at 0.6. Hence, the filtering envelope that is normally adopted for ULS analyses may not be adequate for the evaluation of the wind-induced fatigue phenomenon.

An alternative approach is the use of a moving average filter. From Fig. 6.21, it is possible to observe how the filter with $k = 1$ fits quite well the experimental admittance functions for all the wind incoming directions. The results described in the following paragraphs are therefore associated to the use of the moving average filter, instead of the experimental filter.

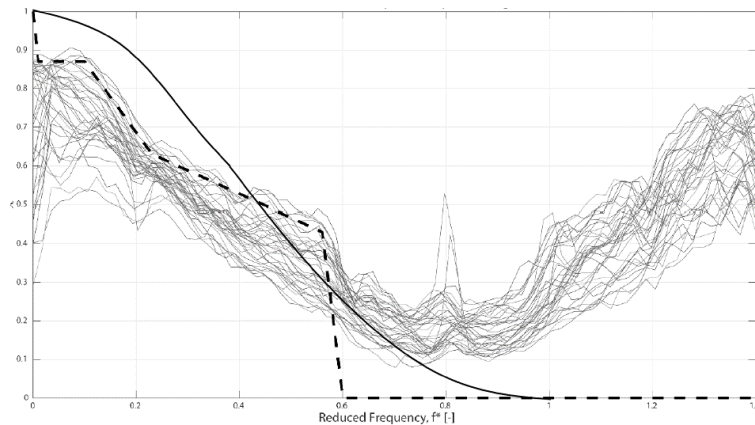


Figure 6.21: *Moving average filter with $K = 1$*

Following the filtering procedure, the pressure associated with each pressure tap is applied to its respective tributary area and converted on the rafters into distributed forces based on the type of load patch shown in Fig. 6.22.

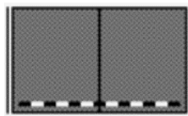


Figure 6.22: *Load patch type*

The Fig. 6.23 shows the load patches distribution in the FE model and the corresponding rafters. Due to the rafter's curvature, each pressure tap's tributary area is divided into two or four load patches, depending on the dimension of the tributary area.

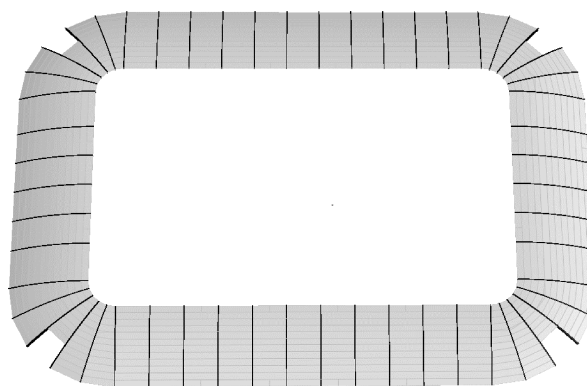


Figure 6.23: *Load patch layout*

It should be noted that the present approach assumes that no significant aeroelastic effects occur. The study is, in fact, addressed to “rigid” roof structures for which the

Chapter 6. Application: wind-induced fatigue calculation of a stadium roof

time and space variant pressure fields are obtained based on WTTs on rigid models.

In conclusion, the wind tunnel test provided the time histories of pressure coefficients related to every load area of the roof, and to many directions of wind, obtained by rotating the structure at different attack angles. For the purpose of the current calculations, the directions in Tab. 6.3 were considered.

$$\alpha \mid 180 \quad -140 \quad -90 \quad -40 \quad 0 \quad 50 \quad 90 \quad 140$$

Table 6.3: *List of considered wind tunnel simulations*

6.5.2 Computational Wind Engineering simulation

As an alternative to conducting a wind tunnel test on a rigid model of the stadium, a Computational Wind Engineering study can be framed in the procedure for the calculation of wind-induced fatigue, using the CFD approaches described in the chapters 2 and 5. This model can be employed to obtain a series of time histories of pressure coefficients on each load area of the stadium roof, for each of the wind directions considered in the Wind Tunnel test. This requires to conduct a transient solution for each of these conditions, which is extended enough in time in order to provide a sufficiently representative loading simulation and, therefore, a computationally efficient turbulence model such as PANS is required for a feasible computational effort. The purpose of this paragraph is, however, only to illustrate the key points that must be considered in the construction of a model in order to complete the fully numerical method of wind induced fatigue of a megastructure as the actual simulation is not carried out here. It is important to take into account the fact that further research is still needed to achieve complete usability of the PANS models illustrated here for calculating the action of the environmental wind on a megastructure and in particular, with respect to the modeling of the turbulent Atmospheric Boundary Layer. Since the fluctuating wind load is related to an Atmospheric Boundary Layer problem, the fluctuations are related both to:

- coherent turbulent structures coming from the inlet, due to the peculiar wind natural spectral content;
- coherent turbulent structures that generate due to the blockage of the structure itself and of the obstructions nearby.

The two approaches generally adopted to introduce the first source of turbulent structures have been addressed in Chapter 2 in relation to the ABL modeling:

- Through synthetic turbulence generators;
- Through a precursor simulation.

The first approach, has seen in recent years the development of a series of algorithms that are able to introduce a divergence-free velocity field into the computational domain, such as the DF-SEM algorithm by Poletto [30], which is readily available in open-source CFD code OpenFOAM, or the CDRFG method by Aboshosha and Huang [46], which was already proven to introduce the proper turbulence spectra and coherency in case of ABL. The second approach, on the contrary, requires running a separate simulation of the flow behind a wind-tunnel precursor, and then uses the time history of various flow parameters computed with this simulation as the inlet of the actual calculation. This approach has the advantage of considering a physical-based inlet, but has the evident drawback of having a heavy computational cost. It appears to the author that the latter method would be advisable to be used in conjunction with Wind Tunnel Tests, as it relies heavily on the configuration of a particular tunnel, and would allow extending or integrating any wind tunnel tests with CFD simulations based on the same boundary conditions and therefore characterized by high coherence. The first method appears, on the contrary, more suitable for use if the WTT data were not available. The issue of ABL modelling is, at the moment, one of the most discussed and studied topics in the field of computational wind engineering and the use of PANS for this purpose has yet to be delivered. This application represents one of the main future developments related to the themes introduced with this thesis and also appears fundamental to allow a complete numerical procedure for the calculation of wind induced fatigue.

Once the boundary conditions are defined, the main features of the simulations need to be addressed:

Target geometric level of detail

To address a target geometric level of detail means to simplify the geometry of the structure as much as possible, without affecting its effects on flow field. A structure like AEK Stadium is characterized by extremely fine details which are incompatible with a CFD model, and they need to be addressed with specific sensitivity analyses and, when possible, simplified. For example, the steel lattice trusses below the membrane could be transformed into porous volumes with equivalent effect of pressure drop, under the hypothesis that it is the only effect they provide on the lower surface.

Chapter 6. Application: wind-induced fatigue calculation of a stadium roof

Approach for turbulence modeling

The turbulence modeling approach needs inevitably to be on Scale-Resolving type, since the fluctuating field relies on the ability of the physical model to sustain it. An averaged approach like Unsteady RANS would only produce macroscopic coherent structures, such as the vortices behind a cylinder. The choice of models could therefore be placed on LES or PANS models or other similar approaches. With PANS approach, it is possible to assume that a lower grid refinement would be required compared to LES. In such case, a variable f_k should be adopted to maximize the effectiveness of PANS on the grid.

Computational grid

A thorough meshing process is necessary in every CFD computation, and it is a crucial step for using scale resolving models like PANS or LES. In case a PANS simulation is performed, partial averaging requires the grid to realize a sufficient resolution in order to resolve the part of the turbulent kinetic energy required by the parameter f_k . By adopting a variable-resolution f_k , there is no risk of requesting a f_k which is unsustainable by the grid, but a coarse grid would lead to high values of f_k up to 1, thus collapsing to URANS solution and losing PANS advantages.

The grid refinement should be chosen with the help of a series of 2D models which allow to evaluate the dependency of the result to various parameters with a small computational effort. Two types of analyses should be performed: first the grid density must be varied, in order to find the sensitivity of the result to the refinement level; secondly, the minimum f_k must be varied to evaluate the dependency of the result to the PANS filter. Once a 2D grid is chosen, a 3D grid can be built on the basis of the refinement level.

If wind tunnel results were available together with a CFD simulation, it would be possible to increase the quality of both CFD and WTT approaches. The interaction between wind tunnel tests and CFD simulations will be deeper and deeper, as turbulence models become more reliable and affordable, and will be two-way: on the one hand, since tunnel models can experimentally simulate a physical phenomenon, they can be used as an aid to CFD model validation and to the choice of the optimal numerical modeling; on the other hand, the CFD model produces information that the tunnel model cannot have due to the limited number of measuring instruments. For example, from the CFD model it might be possible to define more accurately the admittance functions to be used for each pressure tap; or, on the basis of the flow fields calculated by the CFD model it

6.5. Wind simulation

would be possible to identify and describe the turbulent structures and their origin.

All grids, both two-dimensional and three-dimensional, should be developed using a two-stage strategy. First, a base coarse structured mesh is built with *OpenFOAM* utility *blockMesh*, further referred to as *Base Mesh*. Then multiple refinements are performed on the volumes that need refinement using *snappyHexMesh* utility. The level of refinement indicates the number of divisions carried out in each direction.

- *Inlet*: the domain from the inlet up to the structure must provide a sufficient discretization in order to sustain the turbulent coherent structures introduced at the inlet;
- *Near-wall*: finest refinement around the structure;
- *Focus region*: region around the structure which still needs refinement.
- *Wake region*: region in the wake of the structure, where a higher number of elements is necessary to calculate recirculation phenomena.

An example of a two-stage grid (here, a coarse mesh) is shown in Fig. 6.24

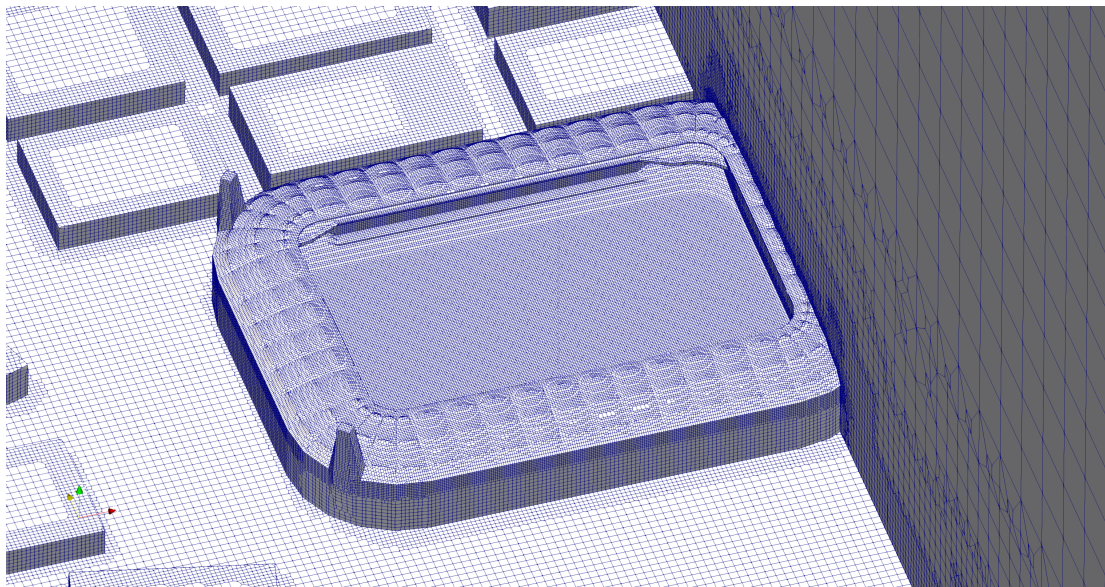


Figure 6.24: Detail of the computational grid

Numerical setup

In order to obtain numerical accuracy, Second order methods must be adopted for time discretization and divergence calculation.

Chapter 6. Application: wind-induced fatigue calculation of a stadium roof

Output configuration

Since the amount of data requested is high, a series of points of measurement of the quantities of interest must be prepared before the simulation, so that they are extracted during the calculation. In this way it is not necessary to store all the time instants of all the variables of the fluid domain, but only the output data at the points of interest. In the case of AEK Stadium, the data of interest consist on the time histories of the averaged pressure coefficients acting on each load area of the roof.

6.6 Modal analysis

The time histories of pressure acquired by the wind tunnel test are scaled for the various average speeds to the reference altitude of the roof (with respect to which they had been made dimensionless in the wind tunnel). The list of simulations is shown in Table 6.4.

α	180	-140	-90	-40	0	50	90	140
$V_m = 21m/s$	1	2	3	4	5	6	7	8
$V_m = 20m/s$	9	10	11	12	13	14	15	16
$V_m = 19m/s$	17	18	19	20	21	22	23	24
$V_m = 18m/s$	25	26	27	28	29	30	31	32
$V_m = 17m/s$	33	34	35	36	37	38	39	40
$V_m = 16m/s$	41	42	43	44	45	46	47	48
$V_m = 15m/s$	49	50	51	52	53	54	55	56
$V_m = 14m/s$	57	58	59	60	61	62	63	64
$V_m = 13m/s$	65	66	67	68	69	70	71	72
$V_m = 12m/s$	73	74	75	76	77	78	79	80
$V_m = 11m/s$	81	82	83	84	85	86	87	88
$V_m = 10m/s$	89	90	91	92	93	94	95	96
$V_m = 9m/s$	97	98	99	100	101	102	103	104
$V_m = 8m/s$	105	106	107	108	109	110	111	112
$V_m = 7m/s$	113	114	115	116	117	118	119	120

Table 6.4: List of ij transient simulations related to i – th direction and j – th velocity level

A total of 120 global FEM models are thus produced. Each model is equivalent from a structural point of view but is loaded with a time history of loads related to one of the above cases.

The time duration considered for the analysis is about 10 minutes at the design wind speed (7500 load steps), i.e. 1/10 of the total duration of the simulations tests in the wind tunnel. The minimum time step of analysis has been obtained based on a

6.6. Modal analysis

preliminary analysis. It has been found at the maximum design wind speed, the last frequency that significantly contributes to the dynamic response can be considered equal to 2 Hz. Therefore, the adopted time step is $\delta t_d = 0.04s$. If on one hand, as the wind speed decreases the time duration of the analysis increases, on the other hand, also the excited frequencies reduced in number and become a single value at the quasi-static wind speed. These considerations allow the use of a larger time step as the wind speed decreases; in particular $\delta t = 0.06s$ for wind speeds in the range [21; 17], $\delta t = 0.08s$ for wind speeds in the range [16; 13], $\delta t = 0.1s$ for wind speeds in the range [12; 7]. For what concerns the choice of the structural damping, the selected logarithmic decrement is equal to $\delta = 0.05$; this value is the one provided by the Eurocode 1-4 Annex F (Table F.2) for steel buildings or steel structures (bridges and lattice towers) with ordinary bolted joints. This value leads to the choice of the damping ratio $\zeta = 0.008$, which is assigned to the first natural frequency $f_1 = 0.84Hz$ and the last frequency $f_2 = 2.5Hz$; it should be noted that Rayleigh formulation underestimates the damping for all frequencies in the range $[f_1; f_2]$, while overestimates the damping for all the frequencies higher than f_2 or lower than f_1 (see Fig. 6.25).

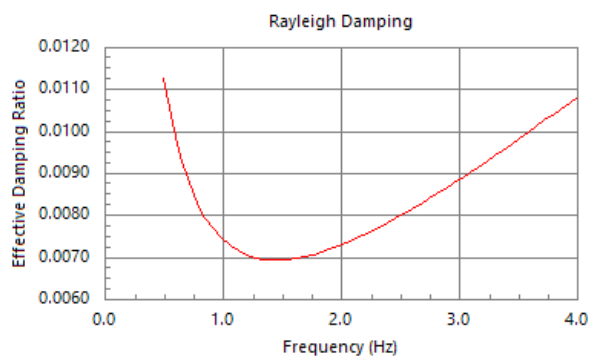


Figure 6.25: Structural damping ratio adopted for the dynamic analysis

The solution here performed is linear transient. However a geometric non-linearity could easily be included in the computation since the calculation is based on the use of finite element models that can employ consolidated commercial and non-commercial software tools. This is a major advantage of the procedure, as non-linearity by geometry can be a significant factor in stress calculations in slender structures, and cannot easily be implemented in a frequency domain calculation.

In the following, a brief discussion on the dynamic response to wind is presented. The discussion is based only on the fatigue relevant directions identified by the statistical analysis, namely +90/ -140/ 180 and evaluates the Power Spectral Density (PSD) of the

Chapter 6. Application: wind-induced fatigue calculation of a stadium roof

displacement in three nodes, identified in Fig. 6.26:

- Node A, at the center of the main roof side;
- Node B, at the center of the short roof side;
- Node C, at the angle of the roof.

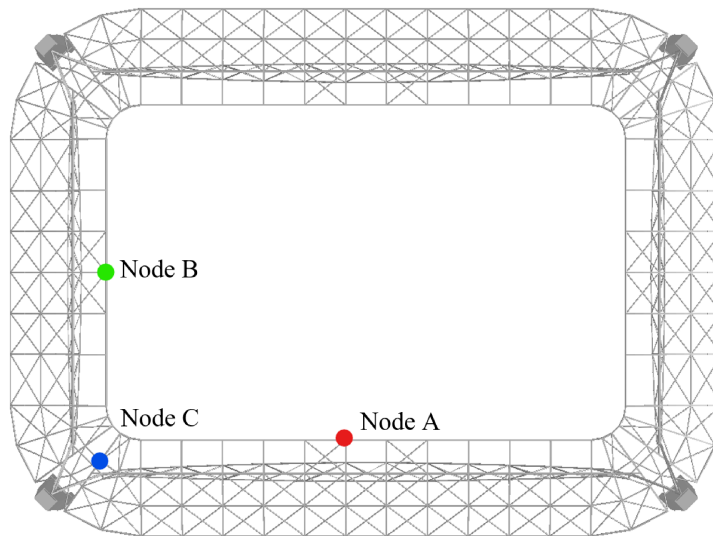


Figure 6.26: Observed nodes on the roof

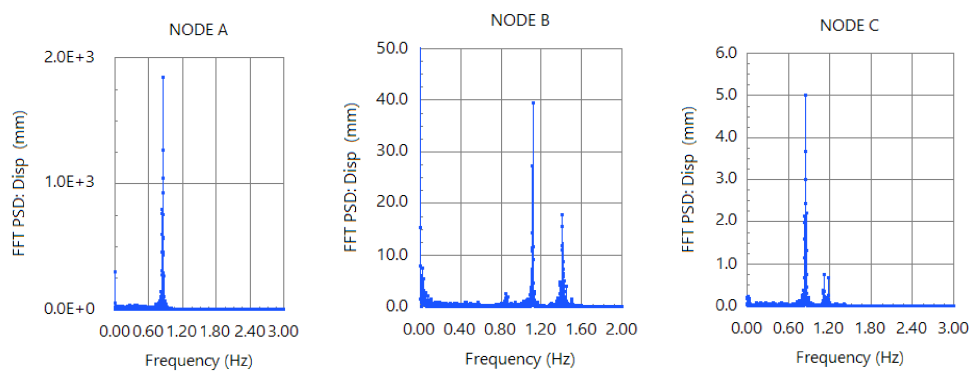


Figure 6.27: PSD of the displacement at 21 m/s (direction +90)

6.6. Modal analysis

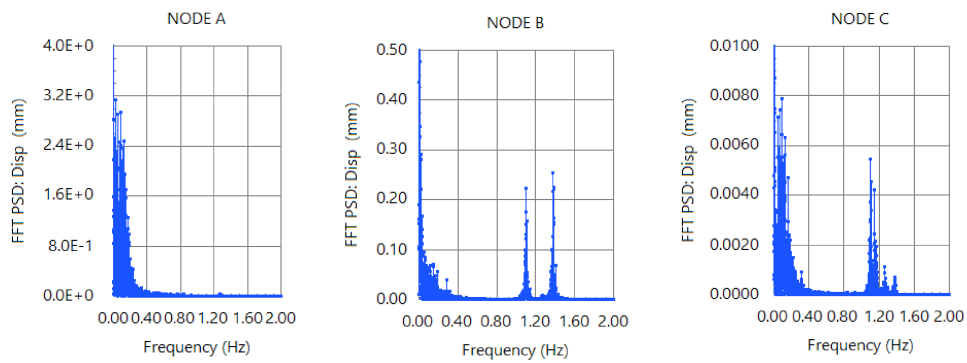


Figure 6.28: PSD of the displacement at 7 m/s (direction +90)

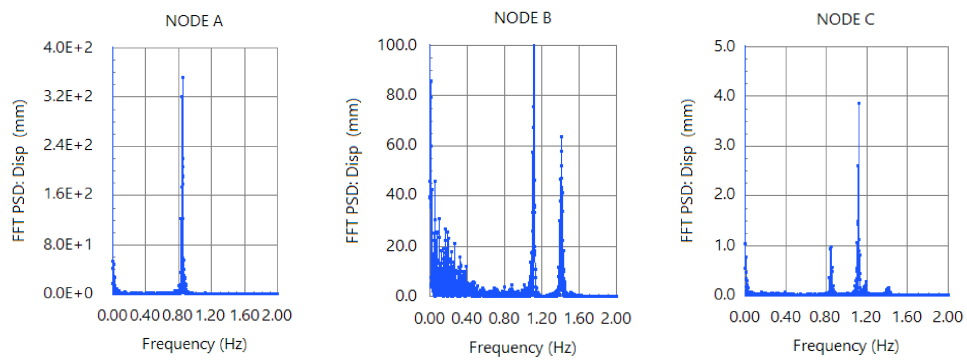


Figure 6.29: PSD of the displacement at 21 m/s (direction -140)

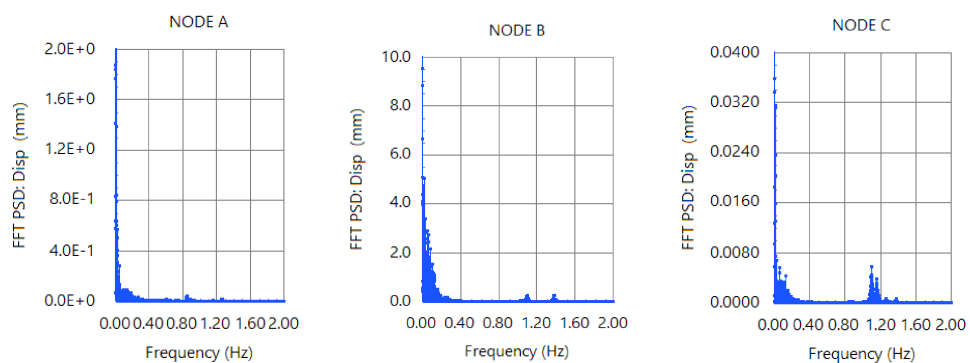


Figure 6.30: PSD of the displacement at 7 m/s (direction -140)

Chapter 6. Application: wind-induced fatigue calculation of a stadium roof

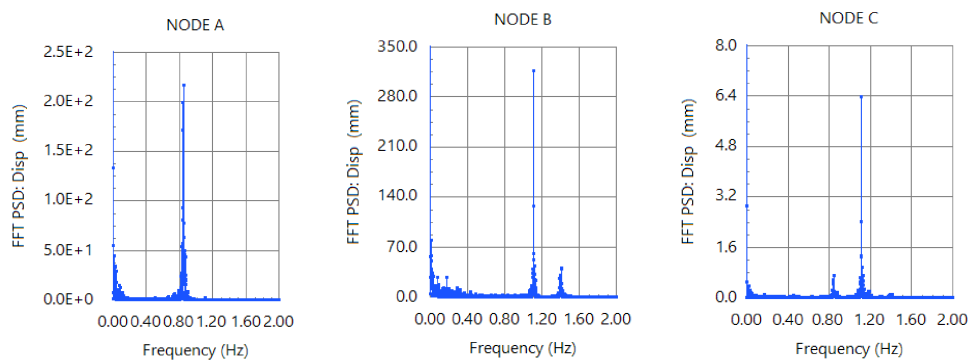


Figure 6.31: PSD of the displacement at 21 m/s (direction 180)

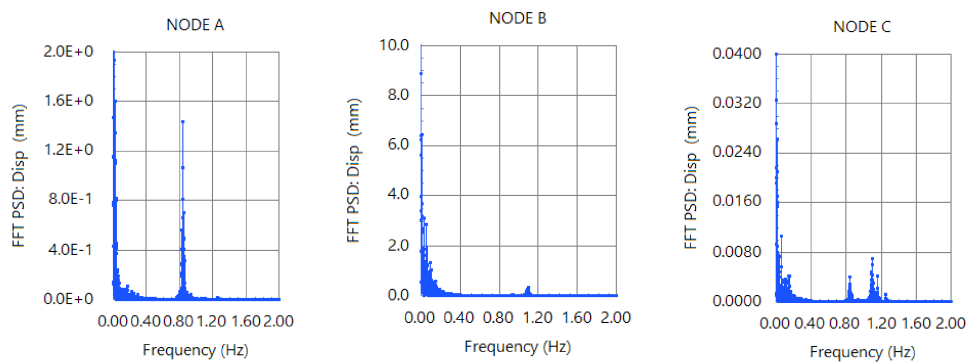


Figure 6.32: PSD of the displacement at 7 m/s (direction 180)

The PSDs in Figs. 6.27, 6.28, 6.29, 6.30, 6.31, 6.32 provide a series of relevant informations.

- For node A, the PSD of the response at 21 m/s shows a peak at a frequency of 0.84 Hz corresponding to the first frequency of the structure (first cantilever mode) for all the wind excitations, and hence the response is a typical narrow-band.
- As the wind speed decreases from 21 m/s to 7 m/s, the response becomes quasi-static and the PSD of the displacement has all the wind energy content outside from the range of the structural frequencies, as shown in Fig. 6.28. This is due to the fact that, once scaled at a speed of 7 m/s, wind tunnel measurements do not have frequency content to excite the structure.
- For nodes B and C, the PSD is not narrow-band anymore for both high and low wind speeds and depends on two structural modes which have a different weight in the response based on the direction and on the intensity of wind.

- The response type is thus dependent on the location in the structure, on the direction of wind and on the level of wind velocity.

The hypothesis of narrow-band are, therefore, not sustainable for all the points of the structure and for all wind velocities. It is therefore necessary to evaluate the contribution on the dynamic response due to all the spectral components excited on the structure, in order not to neglect important sources of fatigue cycles. Generating a time history for each wind direction and for each wind speed level to which the structure may be subjected during its lifetime appears to be the simplest way to consider all possible frequency contributions without the need to pose hypotheses that could prove too much, or too little, conservative in the case of a complex structure such as the one under examination.

6.7 Cycle counting

As addressed in Chapter 4, the cycle counting procedure must proceed as follows:

- **Definition of the local shell FE model**

A local shell FE model is built (Fig. 6.33), which represents a joint of the main truss of the roof whose position is shown in Fig. 6.34. The model is built in *Strand7* environment and uses mainly QUAD4 shell elements with a minority of TRI3 elements. This connection has been selected to highlight the key aspects of the fatigue assessment procedure. The joint is located at the lower chord of one of the two main long trusses and its position is almost at the quarter span of one of the main long truss. The position of the interfaces of the connection was chosen at a sufficient distance from the convergent central node in order to avoid local redistribution effects. The joint presents a main T-section beam (600 x 400 x 35) and 6 CHS hollow section diagonals, all converging to a central node. The connection of the diagonal elements are made of internal plates welded to the CHS profiles and bolted to cover plates (thickness of 2 mm) that, in turn, are welded to the beam web.

- **Choice of Virtual Strain Gauges**

Before the virtual strain gauges can be defined, it is necessary to solve the local shell FE model by imposing a series of cases of unitary displacements at the boundaries (Fig. 6.35). Each of these cases provides the stress due to a unitary displacement at each boundary in every plate element. Then, a number of virtual strain gauges is chosen to allow a complete identification of the fatigue load in

Chapter 6. Application: wind-induced fatigue calculation of a stadium roof

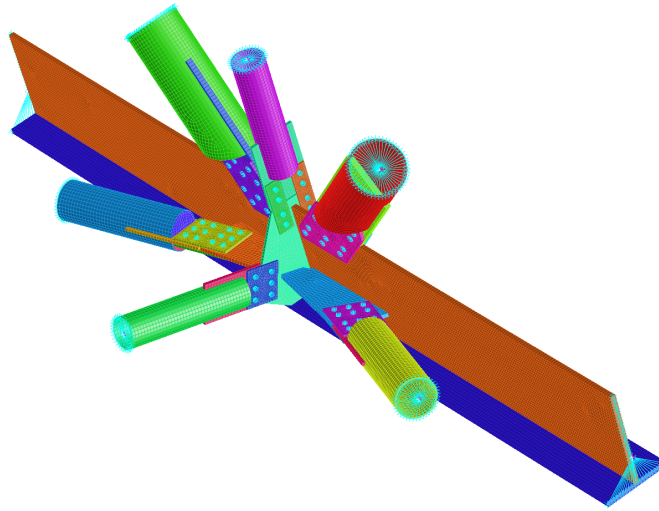


Figure 6.33: Local shell FE model of a connection

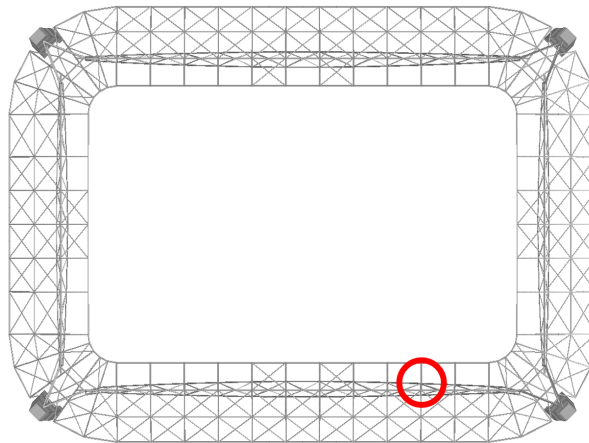


Figure 6.34: Joint position in the global model

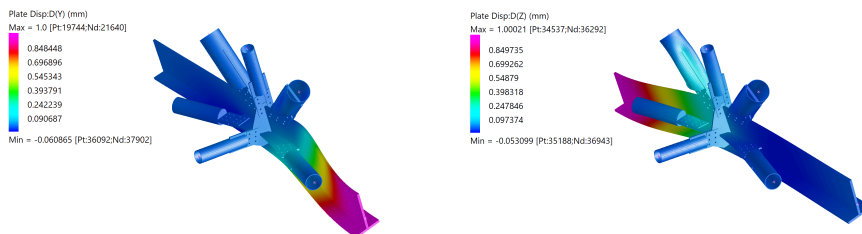


Figure 6.35: Sample solutions of the shell FE model with unitary displacements applied at the boundary

all the points of the local shell model. While, on one hand, the sample of VSGs should be enough populated to capture the different behaviors due to the complex

6.7. Cycle counting

global dynamic response of the structure, on the other hand it is not necessary to select too many VSGs. In fact, each virtual strain gauge is representative of a correlated area where stress time histories are synchronized. For this correlated area, the stress cycles are identified by the same time steps, hence it is not necessary to introduce more than one VSG for each correlated area. As an example, a series of VSGs is chosen for the connection under study, which is shown in Fig. 6.36. For

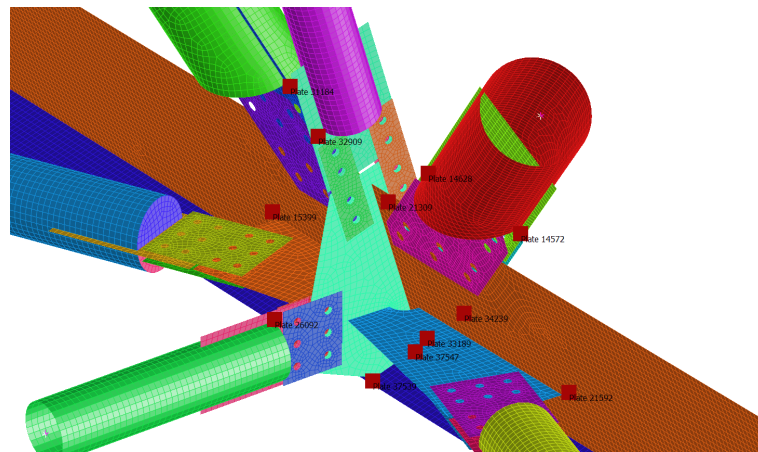


Figure 6.36: Virtual strain gauges selected in the connection (red markers)

each VSG, the surface of the plate (+z, midplane, -z) where the Influence Vector (see Section 4.5) is built must be chosen a priori. This choice can be done by evaluating if the expected behavior is mainly flexural or membranal. In general, the choice of a +z or -z face appears to be more convenient than midplane. An automatic algorithm built using Strand7 API allows to generate the relevant information for each virtual strain gauge by communicating directly with the local shell FE model and its results:

- The stress components σ_{xx} and σ_{yy} due to each of the unitary displacements at the boundary. The array of these stress components was defined in Section 4.5 as *Influence Vector* and allows to directly calculate the stress in the VSG by multiplying the actual displacements measured at the boundary of the connection from the modal solution;
 - The plate number associated to the VSG;
 - The chosen surface (+z, midplane, -z);
 - A progressive ID number.
- For each Virtual Strain Gauge, it is possible to compute the complete time histories of stress for all the ij simulations in Table 6.4.

Chapter 6. Application: wind-induced fatigue calculation of a stadium roof

- Every time history of stress is then treated with Rainflow Cycle Counting algorithm, thus identifying the total number of cycles associated to different levels of range $\Delta\sigma$ and mean stress $\bar{\sigma}$. In Fig. 6.37 a sample time history measured in one of the VSG is shown, with a representation of the peaks and valleys identified as the start and end of every cycle. In the same figure, the largest range is also displayed as a red thick line. It is possible to notice that the largest range starts and ends in time instants far from each other.

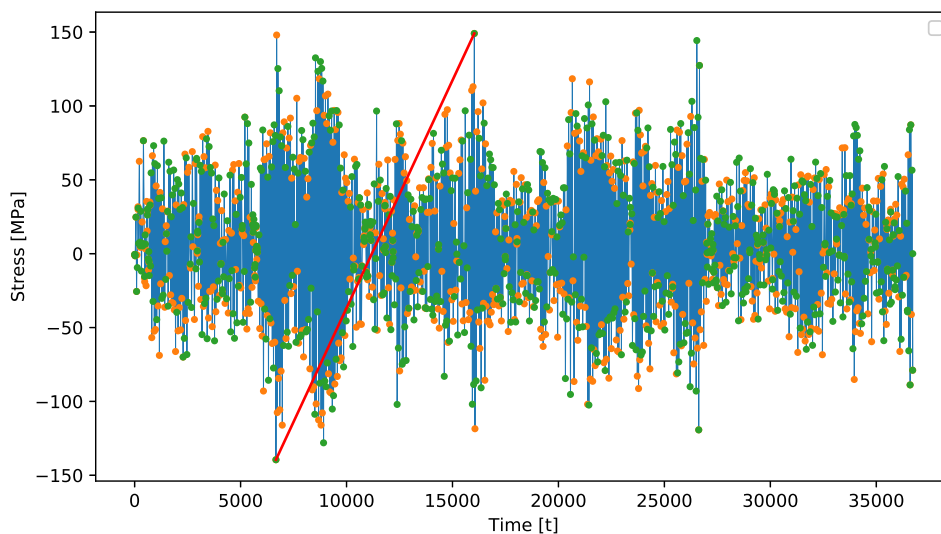


Figure 6.37: Time history of stress at a VSG (blue line), peaks and valleys of measured cycles (markers), largest range (red line)

- The cycles counted are then grouped by a discrete 64x64 matrix of range $\Delta\sigma$ and mean stress $\bar{\sigma}$;
- The numbers of cycles in each bin of the matrix are then scaled to consider the total number of hours in the lifetime of the structure by α_{ij} ;
- The number of cycles considered for all the conditions ij for a VSG are then summed to obtain the wind-induced fatigue spectrum at each VSG. The result is still a 64x64 matrix, where most of the cycles are concentrated around a zero $\bar{\sigma}$ and with low values of $\Delta\sigma$, as shown in Fig. 6.38.

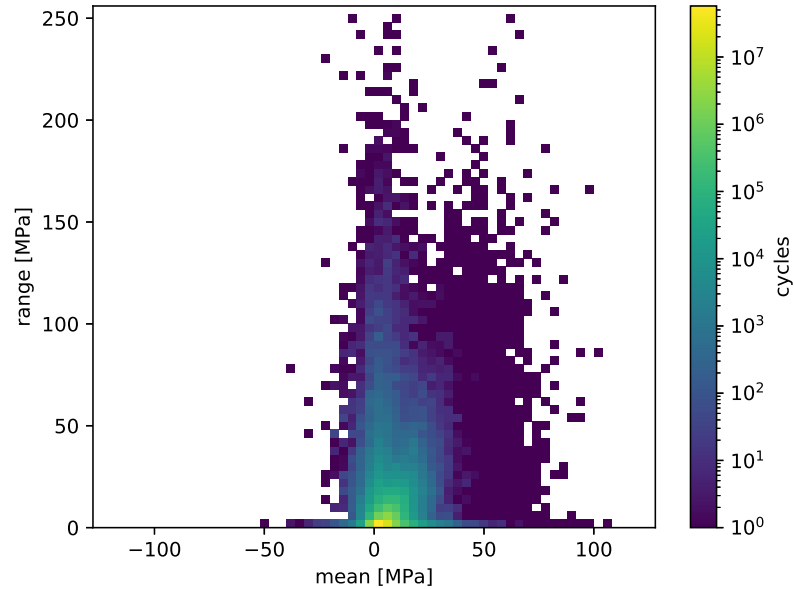


Figure 6.38: *Fatigue load distribution at a VSG*

Fig. 6.38 shows the number of cycles associated with a $(\Delta\sigma, \bar{\sigma})$ combination relative to the VSG where the most intense cycle was found, chosen for convenience of representation (Fig. 6.39). It is possible to observe that the number of cycles

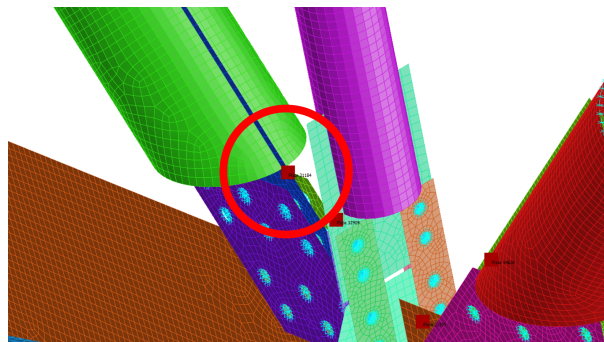


Figure 6.39: *Selected VSG*

related to high-stress ranges is relatively low, while it increases as the stress range reduces. This representations of the fatigue load distribution are also able to provide useful information about the loading state in a VSG. It is, in fact, possible to observe that the distribution of cycles is not symmetric around a mean value, as shown in Fig. 6.38. The reasons for this asymmetry can be easily understood by observing the exploited numbers of cycles in function of the direction of wind loading (Fig. 6.40). Wind loading is in fact not symmetric and different

Chapter 6. Application: wind-induced fatigue calculation of a stadium roof

directions of loading may cause different mean wind loads, as it happens in this situation.

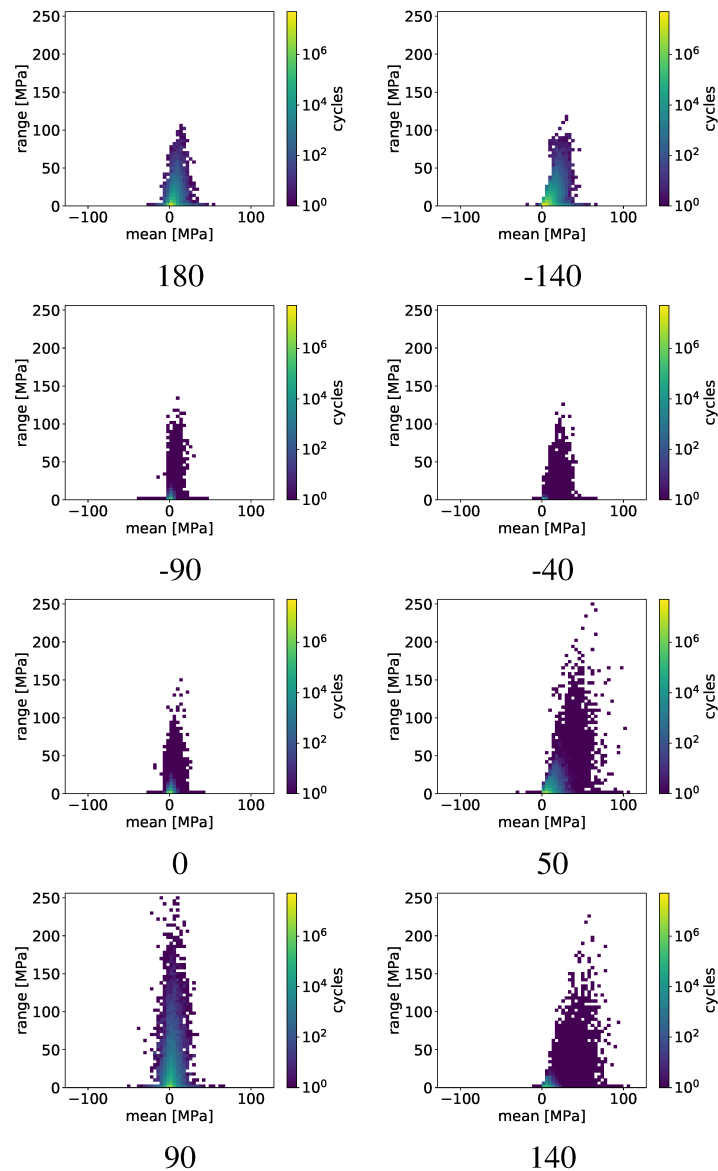


Figure 6.40: *Computed cycles at a VSG for each wind direction*

The total fatigue load distribution in Fig. 6.38 is then exploited in function of the contributions of each velocity level, as shown in Fig. 6.41. It is clear from these figures that higher wind velocities exhibit a more dispersed distribution of cycles, both on stress range and on mean values, and are responsible for the most intense stress cycles. However, high velocities are also associated to a low level of occurrence during 50 years of lifetime. Lower velocities generate lower

6.7. Cycle counting

intensity cycles but related to higher numbers of cycles. By observing Fig. 6.41 it

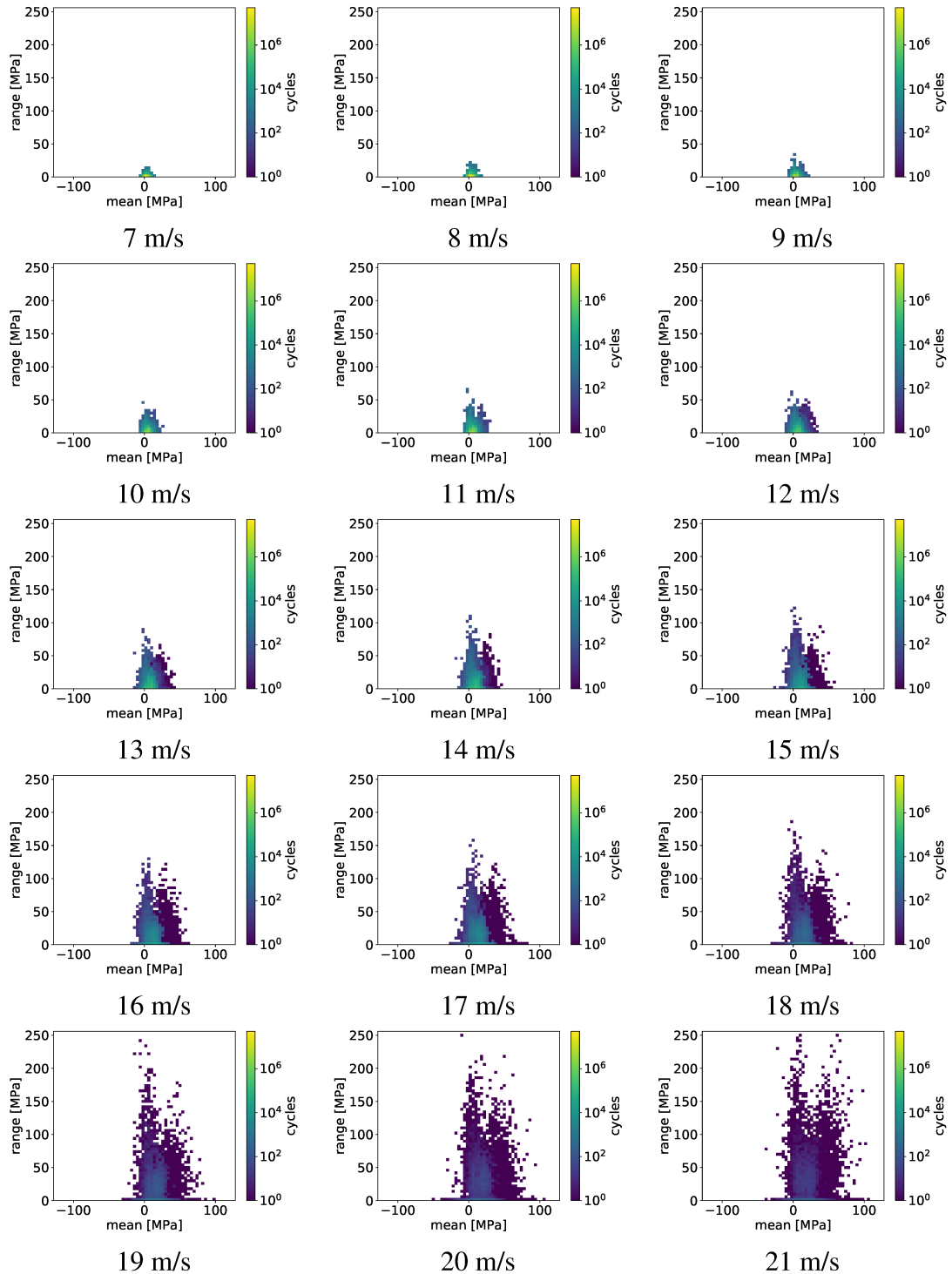


Figure 6.41: Computed cycles at a VSG for each wind direction

is possible to observe that at 7 m/s stresses are already lower than the cut-off limit. Following EC3 1-9 requirements, no further damage could be produced by these

Chapter 6. Application: wind-induced fatigue calculation of a stadium roof

cycles. However, IIW instructions do not support the concept of infinite-life and introduce the $m = 22$ slope for $N > 10^8$). Here the calculations are performed with the EC3 1-9 approach, as it is shown in further sections that already for cycles related to a lower number of cycles (e.g. 10^6) there is no more damage accumulation. The effect of lower wind velocities could however be included by just scaling the fatigue spectrum measured at 7 m/s, since at 7 m/s it is shown that generally no dynamic amplification occurs anymore and the effect of wind on structure is quasi-static.

- Loading of the local shell FE model with the stress cycles: for each of the blocks in the 64×64 matrix, the displacements that induce each state of stress corresponding to a non-empty bin in the fatigue load distribution (Fig. 6.39) of each VSG are then loaded as boundary conditions in the local shell FE model. In Fig. 6.42, the stress distribution in the connection which represent the highest $\Delta\sigma$ in the sample VSG is shown. The maximum $\Delta\sigma$, around 250 MPa, is clearly reproduced in the shell FE model.

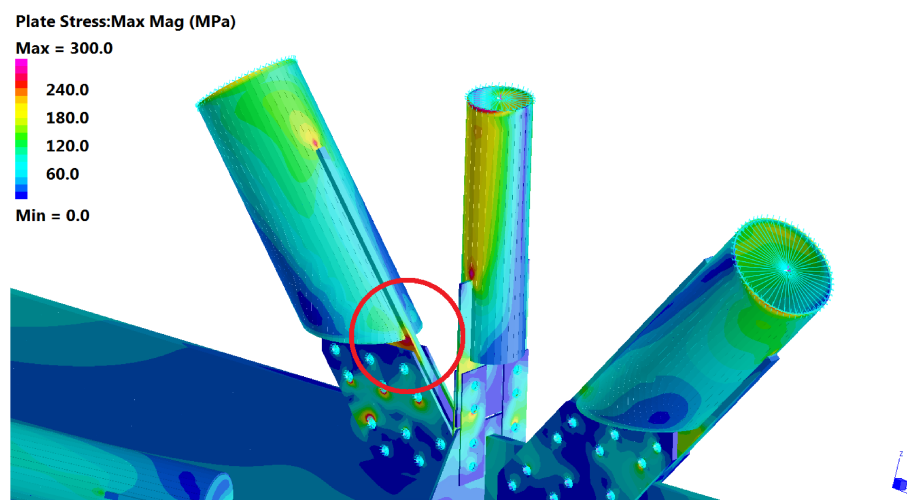


Figure 6.42: Local shell FE model with the application of the boundary conditions that introduce the highest stress cycle in the sample VSG

6.8 Detailed fatigue design

6.8.1 Approach for fatigue design

The roof structure contains hundreds of connections: about 200 in the main trusses, 170 between rafters and ring beams, dozen in the hanging system. Each connection

6.8. Detailed fatigue design

contains dozens of welds and each weld would require up to 28 fatigue verifications. This quantity of elements to be designed against fatigue excludes the possibility of using local fatigue methods that require very fine and rigorous meshes, such as the NSIF or the Effective Notch Stress.

The approach adopted for the wind-induced fatigue design of the joints of the stadium is thus based on the Modified Nominal Stress with SED correction of the bending components of stress presented in Section 3.2.2. This approach assumes that the structure respond elastically, oligocycle fatigue is not present, and is consistent with the fact that the modified nominal stress considers the crack initiation life which represent the most significant phase in terms of cycles. Therefore, the crack propagation phase is not considered, in favour of safety. This conservativity is generally considered acceptable in the design of civil structures, as the number of cycles of the crack propagation phase is generally a fraction of the number of cycles required for the crack initiation, however the extension of this phase in terms of cycles depends on the chosen detail. Nevertheless, it seems reasonable given all the uncertainties inevitably present in the fatigue load assessment discussed in Chapter 4.

The design process of a steel structure such as the one under examination starts from the conception of the joint, follows in the verification and after the implementation takes place the targeted control depending on the resistance utilization rate and fatigue damage. This flow, in compliance with international standards, ensures the satisfaction of safety performance with attention to the economic fact as per Annex L of EN 1090-2:2018. To complete the process, the traceability of the calculation data using BIM technologies (Building Information Model) provides the possibility to manage the maintenance of the structure in an economic way and therefore allows to follow the design choice of the "damage tolerant method" to reduce initial costs and plan future ones.

The phenomenon of fatigue, in the damage tolerant hypothesis, requires a management that extends from the design phase to that of maintenance of the structure during its lifetime:

1. Conception of the joint;
2. Fatigue verification;
3. Definition of Non Destructive testing (NDT) based on the utilization rate and relevance of each detail;
4. Inspection and maintenance during lifetime.

Chapter 6. Application: wind-induced fatigue calculation of a stadium roof

6.8.2 Calculation of damage

By considering the fatigue load spectrum calculated on the VSG shown in the previous section, the calculation of fatigue on a weld in the nearby area of the VSG is performed (Fig. 6.43).

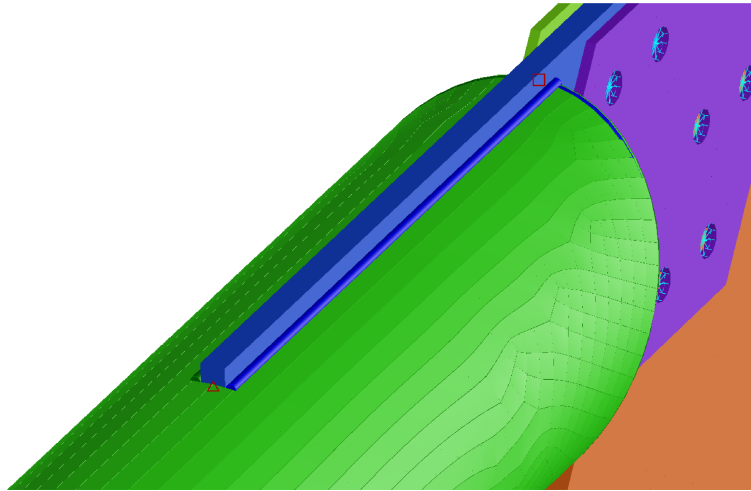


Figure 6.43: Sample weld nearby the VSG. Blue and green cylinders represent the weld fillet at the sides (the two cylinders are not actual finite elements used in the calculation).

As detailed in Chapter 4, a total number of 28 fatigue checks is performed on this weld. A complete report of the total damage calculated for each check is shown in Fig. 6.44.

Weld 37

TJOINT - Fillet 1: 5.0 mm; Fillet 2: 5.0 mm; - L = 621 mm - Start = (34955.839,-48596.962,21165.622); End = (35351.218,-48457.775,20707.872); Weld coord syst at Start: i1=(0.771,-0.188,0.609); Weld coord syst at Start: i2=(-0.002,-0.956,-0.292); $\gamma_{Mf}=1.15$; $\gamma_{Ff}=1.00$; $\lambda=1.00$

	a	a	a1	a1	a2	a2	b	b	c	c	d	d	e	e	f	f	h	h	h	h	g1	g1	g1	g1	g2	g2	g2	g2		
FAT	-	-	36	36	0	0	80	80	100	100	80	80	100	100	56	56	80	80	80	80	56	56	56	56	56	56	56	56	56	
Tab.	-	-	(T8_5, 3)	(T8_5, 3)	(T8_5, 8)	(T8_5, 8)	(T8_5, 1)	(T8_5, 1)	(T8_5, 5)	(T8_5, 5)	(T8_2, 6)	(T8_2, 6)	(T8_2, 5)	(T8_2, 5)	(T8_4, 6)	(T8_4, 6)	(T8_9, 1)	(T8_9, 1)	(T8_9, 1)	(T8_9, 1)	(T8_9, 2)	(T8_9, 2)	(T8_9, 2)	(T8_9, 2)	(T8_9, 2)	(T8_9, 2)	(T8_9, 2)	(T8_9, 2)	(T8_9, 2)	(T8_9, 2)
Soil.	$\Delta\sigma_W$	$\Delta\sigma_W$	$\Delta\sigma_W$	$\Delta\sigma_W$	$\Delta\sigma_W$	$\Delta\sigma_W$	$\Delta\sigma^{\perp}$	$\Delta\sigma^{\perp}$	$\Delta\sigma^{\parallel}$	$\Delta\sigma^{\parallel}$	$\Delta\sigma^{\perp}$	$\Delta\sigma^{\perp}$	$\Delta\sigma^{\parallel}$	$\Delta\sigma^{\parallel}$	$\Delta\sigma^{\perp}$	$\Delta\sigma^{\perp}$	$\Delta\sigma^{\perp}$	$\Delta\sigma^{\perp}$	$\Delta\sigma^{\perp}$	$\Delta\sigma^{\perp}$	$\Delta\sigma^{\perp}$	$\Delta\sigma^{\perp}$	$\Delta\sigma^{\perp}$	$\Delta\sigma^{\perp}$	$\Delta\sigma^{\perp}$	$\Delta\sigma^{\perp}$	$\Delta\sigma^{\perp}$	$\Delta\sigma^{\perp}$	$\Delta\sigma^{\perp}$	
x	561	561	601	601	561	561	0	0	0	0	601	561	0	561	4	615	0	621	0	621	0	621	0	0	0	0	621	0	0	0
Pos.	1+,2-	1+,2+	1+,2-	1+,2+	1+,2+	1+,2+	1+,2+	1+,2+	1+,2-	1+,2+	1+,2+	1+,2+	1+,2+	1+,2+	1+,start	1+,end	1+,2+,start	1+,2+,end	1+,2+,start	1+,2+,end	1+,2+,start	1+,2+,end	1+,2+,start	1+,2+,end	1+,2+,start	1+,2+,end	1+,2+,start	1+,2+,end	1+,2+,start	1+,2+,end
δ	0.0	0.0	0.0	0.0	0.0	0.0	35.0	35.0	35.0	35.0	6.0	6.0	6.0	6.0	6.0	35.0	35.0	35.0	35.0	6.0	6.0	6.0	6.0	6.0	6.0	6.0	6.0	6.0	6.0	6.0
ks	1.00	1.00	1.00	1.00	1.00	1.00	1.00	1.00	1.00	1.00	1.00	1.00	1.00	1.00	1.00	1.00	1.00	1.00	1.00	1.00	1.00	1.00	1.00	1.00	1.00	1.00	1.00	1.00	1.00	1.00
ksmp	1.00	1.00	1.00	1.00	1.00	1.00	1.00	1.00	1.00	1.00	1.00	1.00	1.00	1.00	1.00	1.00	1.00	1.00	1.00	1.00	1.00	1.00	1.00	1.00	1.00	1.00	1.00	1.00	1.00	1.00
kses	1.00	1.00	1.00	1.00	1.00	1.00	1.00	1.00	1.00	1.00	1.00	1.00	1.00	1.00	1.00	1.00	1.00	1.00	1.00	1.00	1.00	1.00	1.00	1.00	1.00	1.00	1.00	1.00	1.00	1.00
km	1.00	1.00	1.00	1.00	1.00	1.00	1.00	1.00	1.00	1.00	1.00	1.00	1.00	1.00	1.00	1.00	1.00	1.00	1.00	1.00	1.00	1.00	1.00	1.00	1.00	1.00	1.00	1.00	1.00	1.00
Dtot	0.00011	0.00011	4.7E-05	4.8E-05	0.00011	0.00011	0	0	0	0	6.5E-05	5.6E-05	0.00014	2.6E-05	0.054	0.0016	0	0	0	0	0.0021	0	0	0	0	0	0.002	0	0	0
Check	<1.0	<1.0	<1.0	<1.0	<1.0	<1.0	<1.0	<1.0	<1.0	<1.0	<1.0	<1.0	<1.0	<1.0	<1.0	<1.0	<1.0	<1.0	<1.0	<1.0	<1.0	<1.0	<1.0	<1.0	<1.0	<1.0	<1.0	<1.0	<1.0	<1.0

Maximum Dtot,max=0.054 in check f Start principal plate - toe f. - $\Delta\sigma^{\parallel}$; at position x=-6.00 mm(1+,start).

Figure 6.44: Summary report of the 28 checks performed on the selected weld

The worst check is check type *F* at the start of the weld (marked by a red triangle in Fig. 6.43), which is associated to a FAT56 detail (Table 8.4, detail 1) in EN 1993-1-9

6.8. Detailed fatigue design

and measures a $\Delta\sigma_{//}$ to the weld direction. The total damage for this check is equal to $D_{tot,f} = 0.054 < 1$. The fatigue check is therefore satisfied. For this fatigue check, it is possible to extract the distribution of damage in relation to the cumulated number of cycles (Fig. 6.45).

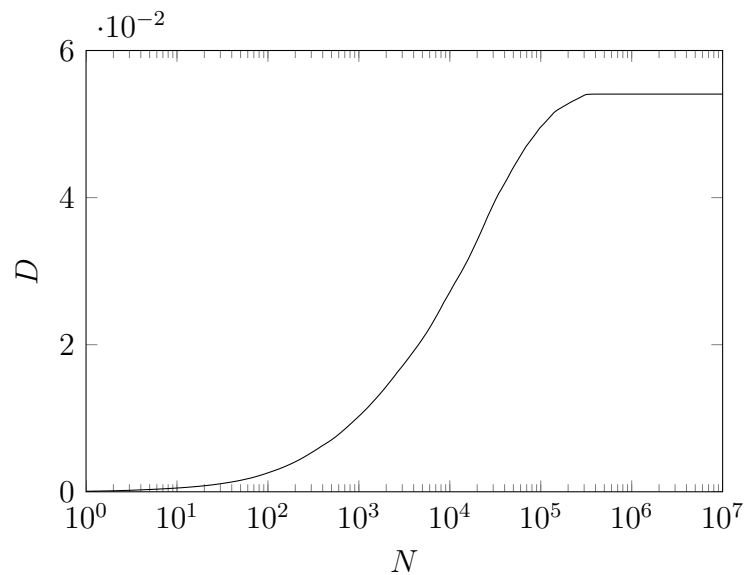


Figure 6.45: Cumulated damage for check f at weld start

In order to complete the fatigue verification of the connection, all the welds and the parent material need to be checked with the same approach, by considering the fatigue load spectrum related to the nearest VSG. Once all the welds and the parent material are verified, the highest value of damage leads to the calculation of the fatigue life of the connection. The minimum fatigue life in all connections represents the fatigue life of the structure T_F , which needs to be greater than the nominal life of the structure V_N .

If EN 1991-1-4 Annex B.3 were applied, thus excluding any directional effect, the damage in check f can easily be calculated and is equal to $D_{tot,f} = 4.7 > 1$. The ratio between the damage calculated using Eurocode equation and the one computed here is equal to $\frac{4.7}{0.054} = 87$. For the same cycles, the Eurocode curve is associated with much higher stress values. Considering that in the damage calculation stress is elevated with an exponent of 3 or 5, this level of conservativity can lead to an uneconomic design. The adoption of the Eurocode formulation would therefore be highly inappropriate as it is a non-directional approach that does not consider that a large megastructure like the one under study may have, in every point, very different responses to various wind loads. This is evident by observing the comparison for the distribution of stress cycles for the two approaches in Fig. 6.46.

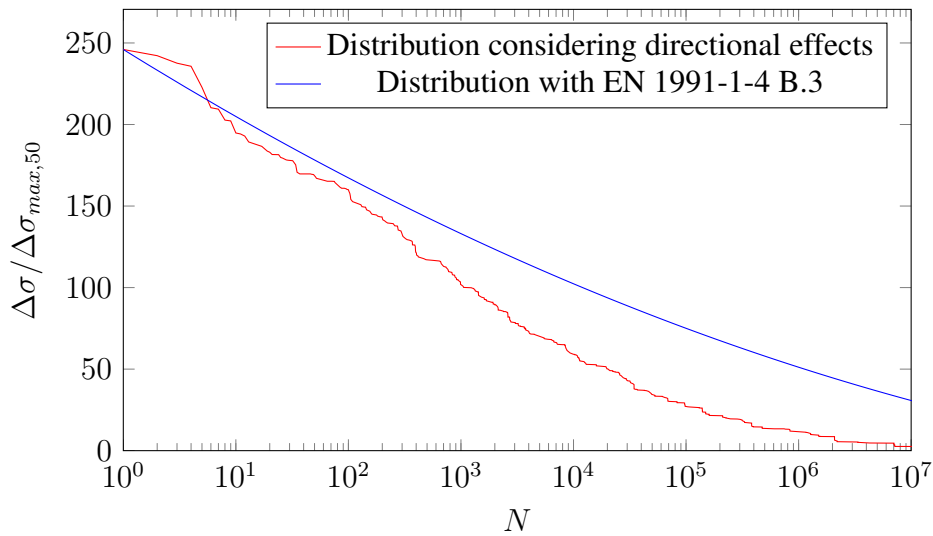


Figure 6.46: Cycles distribution for check f at weld start

The difference between the hypotheses for the calculation of fatigue cycles in Fig. 6.46 are numerous. In Chapter 3 a study from Kemper and Holmes was reported where the sensitivity of the Eurocode curve to various involved parameters analyzed. In that study, the conservativity of the curve was highlighted, as:

1. It does not consider actual structural response;
2. It does not consider wind directionality;
3. It does not consider different Weibull distributions of wind, in particular relatively to Weibull shape factor k .

From Fig. 6.40, it is possible to observe that the direction that generates the most of the cycles is direction 90. This could be easily expected a priori since this direction is orthogonal to the long roof side where the considered connection is located. From Table 6.2, it is possible to observe that, for direction +90, which is associated to sectors W-WNW, the average Weibull shape parameter k is less than 1.5, while Eurocode considers a higher value for k , between 2 and 2.5 (see Fig. 3.5). As the value of k reduces, the curve $\Delta\sigma/\Delta\sigma_{max,50} - N$ becomes more bowed and therefore fewer cycles are produced at the same amplitude. Directions 180 and -140 produce a number of cycles which is comparable with that of direction 90, however they cause cycles with lower amplitude due to an inferior effect on the structure.

Directions -90, -40, 0, 50, 140 on the contrary, do not excite much this particular point of the structures and therefore the cycles they generate are very small, both in number

6.8. Detailed fatigue design

and in magnitude, and it is reasonable to expect that they do not contribute to the accumulation of damage. It is possible to calculate the part of the damage due from each part of the damage due from each direction. Since local fatigue calculations are performed on the shell FE model where the fatigue loading is already the sum of all wind conditions, final fatigue calculations lose the information regarding the contribution of each direction on the total damage. It is, however possible to retrieve these information by directly processing the cycles measured at the VSG. Since the position of the VSG is not necessarily at the correct offset from the weld to consider it a nominal stress, and since the orientation of the stresses might not be aligned to the weld, a fatigue stress pilot value of $\Delta\sigma_c = 56\text{MPa}$ in accordance to BS PD 6705-2:2010+A1:2013 is chosen. It is underlined that this calculation is performed only for the purpose of comparing the contribution to the damage caused by each wind direction and does not produce an actual fatigue assessment.

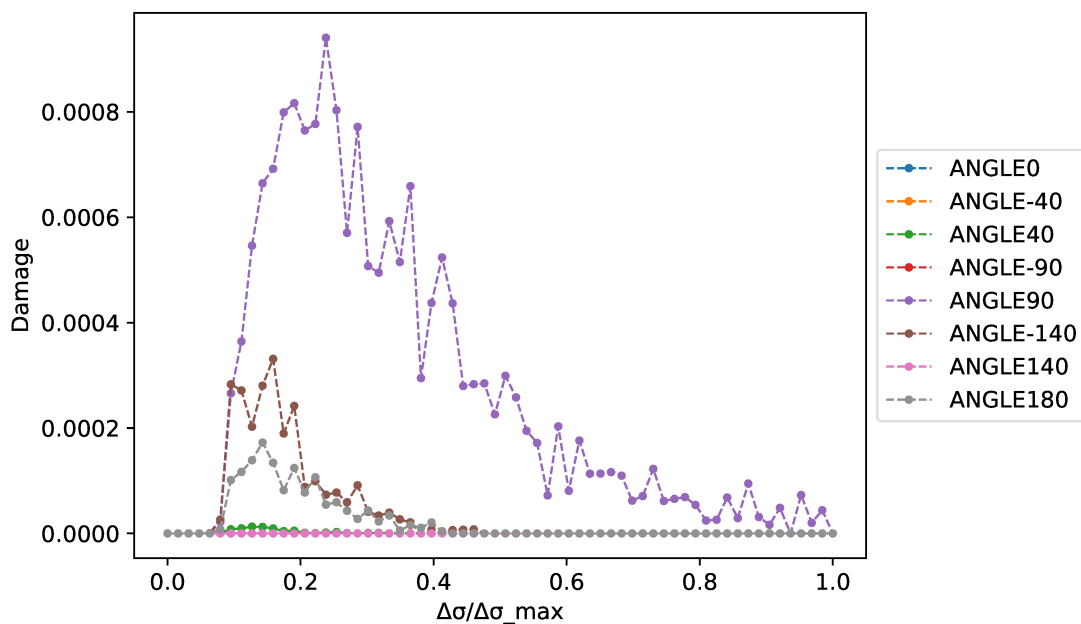


Figure 6.47: Damage distribution over different directions on selected VSG

Chapter 6. Application: wind-induced fatigue calculation of a stadium roof

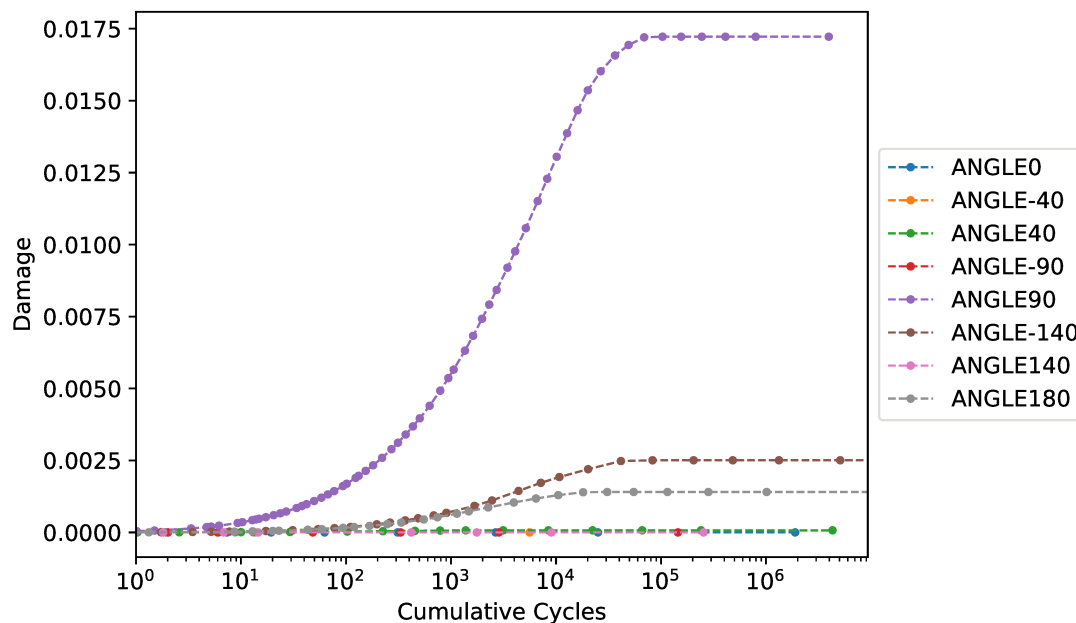


Figure 6.48: *Cumulated damage over different directions on selected VSG*

In Fig. 6.47 and Fig. 6.48, directionality effect in damage accumulation is evident and it is clearly affected both by the positioning of the connection relative to wind direction, and to wind climatic statistics. It should be noted that Fig. 6.45 and Fig. 6.48 do not show the exact same cumulative cycles distribution as they do not consider the same point for the verification and the VSG is not placed in the point of maximum stress (in fact, at the moment of VSG choice, there are no information about the local stress distribution).

6.9 Conclusions

The requirement to design fatigue resistant structures is a concept that is now rooted in European standards and particularly relevant in the case of megastructures, which by definition are linked to designs that are often structurally audacious and that are therefore often dynamically excited by the wind in a significant way. However, there was a lack of a comprehensive design tool capable of uniting all the blocks necessary to control the fatigue phenomenon.

This chapter presented the application of the original method shown in Chapter 4 for calculating wind-induced fatigue on the roof of a stadium. It is important to note that each of the steps which were shown here makes use of generally available data within the design workflow of such a structure. The introduction of this procedure therefore

6.10. Acknowledgements

makes it possible to transform wind-induced fatigue into a true design criterion, just as much as resistance. With this approach it is possible to design structures that manage the phenomena of fatigue right from the start of their conception phase. Until now, the design of such large structures still makes extensive use of concepts of structural symmetry and the use of fatigue details related to standard practice and simplified approaches. The design can be made more efficient, thanks to the approach presented here, by designing each area of the structure with respect to the actual expected wind excitation at the various points, and by calculating the fatigue life of each individual structural detail by means of advanced local methods. This will enable an understanding of the fatigue phenomenon so far unattainable and consequently a higher level of safety, together with a longer service life of the structures. This has positive repercussions not only on the cost efficiency of the work and on the possibility of designing a detailed management plan with respect to maintenance, but also from an environmental point of view, potentially reducing the quantity of material used in areas where it is not necessary and increasing structural durability. Also, in analogy to what is done with offshore flare booms or, more evidently, to wind turbines, when planning constraints allow it, a correct orientation of a megastructure might even represent a simple and viable solution that reduces the overall cost of the steelwork and of the maintenance, while increasing its safety level by reducing the number of fatigue cycles.

6.10 Acknowledgements

The author thanks the National Observatory of Athens (NOA) for providing the wind measurements used for the case study.

CHAPTER 7

Conclusions

The calculation of fatigue life in large steel structures is becoming a frequent design requirement due to various factors such as the ever-rising slenderness of structures, their optimization for resistance design and to the adoption of high-strength materials. Design Standards, such as EN 1090-2, are quickly evolving to adapt to this scenario and are enforcing the necessity to gain a detailed knowledge of the fatigue life for every component, especially welds, that constitute a steel construction product. However, while it is acknowledged that scientific literature has shown a dramatic increase in the quantity and quality of the research on this topic like, for example, the formulation of Repetto and Solari in CNR-DT 207 R1/2018, the topic of wind-induced fatigue design of large, complex steel structures such as a stadium roof is found to require a further effort.

The purpose of the current research activity is thus to provide a consistent approach for the calculation of fatigue in such structures. Due to the unicity of large structures, like stadium roofs or large industrial coverings, and each structure is itself a prototype and most of the parts of their design can only be based on simulation, whether numerical or experimental. Simulations usually are usually performed to quantify wind loading, to calculate dynamic structural response and to design local details in relation to resistance

Chapter 7. Conclusions

and fatigue.

Up to now, there is a low availability of methods in the literature for generalizing and correlating the various topics. In Chapter 4, an approach was developed that combines each aspect and permits the calculation of damage at each point of the structure. The approach is a powerful design tool which allows to overcome the limits of the closed formulations proposed by the Eurocode 1991-1-4, applicable to simpler cases of structure. The procedure was tested and run on a case study, the AEK stadium in Athens, showing the relevant points of the various steps of the analysis. Firstly, the effect of wind on the structure was assessed by means of wind tunnel tests. In this phase, it has emerged the need to consider, during the tunnel-testing phase, the interaction between the frequencies of the wind and those of the structure both at the maximum and reduced speed. Maximum speed is normally used to conduct tests in order to calculate the strength of the structure, whereas all the reduced speeds allow to estimate the effect to wind conditions to which the structure may be subject during its lifetime, whose response affects the fatigue calculation of the structure. The time history of the pressures for each wind direction was then scaled to different speed levels and applied to FE models, thus leading to a transient calculation of the structural response, evaluated in terms of displacement at the nodes. For a connection considered as an example, the time history of stress was then calculated in a series of sample points, here called Virtual Strain Gauges, by means of linear superposition, thus avoiding the need to perform onerous calculations of the time histories on detailed FE shell models. Each stress time history is then subjected to Rainflow Cycle Counting, identifying the number of cycles for a discrete set of blocks of $\Delta\sigma$ associated with each wind condition. The climate statistics at the site where the structure is located were then studied, showing that, in the considered case, a strong wind directionality is evident, and that this has incidence in determining the hours of occurrence of the various wind conditions during 50 years of exposure to wind. The cycles associated with each wind condition measured on each Virtual Strain Gauge are then scaled to take into account the entire service life of the structure. The cycles found on each Virtual Strain Gauge are representative of a larger area nearby the sampling point in the local shell FE model and, by applying the boundary displacement conditions that generate the discrete stress range levels, a fatigue calculation in the detailed FE shell model is carried out. In this model, all the welds are identified, and for each of them the fatigue damage is calculated by adding the contribution of each cycle for each of the verifications required by the Eurocode. A correction of the bending stresses is introduced by means of local advanced models based on the Strain Energy Density approach. Fatigue damage has been finally calculated on

a weld, and was found to be in the order of one hundredth of the damage that would be otherwise obtained considering the fatigue spectrum of the curve of EN 1991-1-4 B.3, which does not consider directionality, climate statistics, and effective structural response. This shows that adopting "conservative" criteria in the case of wind-induced fatigue can result in significantly inefficient evaluations and designs, due to the fact that the stress range is at the power of 3 or 5 for the calculation of damage.

The determination of time-varying wind loads in every point of the structure is the first step necessary for the approach for the wind-induced fatigue calculation proposed in this research project. For the simulation of wind loading, wind tunnels test are traditionally utilized and, specifically when time-dependent solutions of wind load on large structures are required, they represent the standard industrial practice. In order to provide a more efficient and less expensive approach, Computational Fluid Dynamics (CFD) is here introduced as a key aspect of the procedure, since computational power is constantly increasing and turbulence models are becoming more accurate and more computationally reasonable. As megastructures have generally complex geometrical features and the structural effect of wind on each point is strictly dependent on the direction from which wind acts, the wind loads must be assessed from a sufficiently representative number of angles of attack and thus, multiple simulations need to be performed. Whereas it is reasonable to assume that the geometry under consideration is not sensitive to Reynolds numbers effects (i.e. a dependency of non-dimensional loads on wind speed), which is often the case of sharp-edged geometries, it is, reasonable to calculate the time histories of pressure in relation to a velocity only and then to scale them to the different levels of speed to which the structure will be subjected during its lifetime. The data required is therefore large and, in the idea of evaluating the effect of wind by means of computational approaches, it is necessary for them to be computationally efficient. The most popular approach for performing time-dependent scale-resolving analyses is the Large Eddy Simulation approach, whose strict requirements have, however, prevented it from spreading on an industrial scale so far. In recent years, many modeling approaches for turbulence have emerged which provide hybrid modeling approaches such the Partially Averaged Navier Stokes method. This class of model permits a smooth transition between Direct Numerical Simulation (DNS) and Reynolds Averaged (RANS) solution by means of a constant-preserving filter-width parameter f_k . When f_k is equal to 1, the PANS equations collapse to the RANS formulation; when f_k tends to 0, the DNS solution is retrieved; for intermediate values of f_k , a portion of the turbulent kinetic energy is solved using Navier Stokes equations, while a portion is averaged with Reynolds-averaged approach, thus liberating a part

Chapter 7. Conclusions

of the fluctuating scales and improving the quality of the result compared to the fully-averaged solution. Of course, the case of a full DNS solution is feasible only if the computational grid is extremely fine, and, similarly with intermediate values of f_k it is necessary that the grid is able to support the level of required filter. Therefore, it is possible to calculate the value of f_k permitted by a particular grid: when grid is very coarse, high numbers of f_k are realized, when the grid becomes thicker, lower numbers of f_k can be adopted. When a complex CFD model that aims to calculate the flow around a large structure is considered, the number of elements is intrinsically very high due to the high Reynolds number and to the quantity of details, and it is therefore found to be fundamental that PANS models provide an improvement both with low values of f_k (DNS-like solution) and with higher values of f_k (RANS-like solution) thus permitting the adoption of the coarsest grid possible. The potentialities of this new class of models are many: a high accuracy, especially on the wall, comparable or better than that offered by the LES models; a lower computational demand compared to the LES models, since that, to reach a mesh-independent solution less cells and less tight time steps are needed; a simplicity in the implementation, since they are based on existing RANS models. Since these models are very recent, in this research project an original development was carried out to create new models based on this approach that were able to improve the accuracy in terms of turbulent fluctuations, especially in highly separated flows. Specifically, during the research project two new turbulence models were created based on the paradigm of the Partially-Averaged Navier-Stokes models: Realizable $k - \varepsilon$ PANS and $v^2 - f$ with variable C_μ PANS.

The first model was based on the RANS formulation of Shih's Realizable $k - \varepsilon$ model, a high-Reynolds model which provided an improvement over the popular Standard $k - \varepsilon$ RANS model to capture highly separated flows, and provided a more mathematically consistent formulation that ensures realizability and contains the effect of mean rotation on turbulence stress, by adding a variable formulation of the C_μ coefficient. Starting from this parent RANS model, a partially-averaged variation was here proposed. The original model was then tested over two benchmark cases, the case of the flow around a square cylinder and the case of the flow over a backwards-facing step. In both cases, the new model was compared with the literature version of the Standard $k - \varepsilon$ model, already existing in literature, showing an improvement in the ability to predict the fluctuating velocities in the recirculating region with the same computational grid. This feature is considered to be fundamental for the case of flow around megastructures since it represents one of the main phenomena involved.

The second model was, instead, based on the parent RANS formulation of the $v^2 - f$

model by Lien and Kalitzin with the correction by Davidson, Nielsen and Svenigsson, which is a high-resolution, low-Reynolds model that improves the ability of the Standard $k-\varepsilon$ model to capture the behavior of the flow near wall. The original development followed two steps:

1. The RANS model was enhanced introducing the same variable formulation for the C_μ coefficient, thus allowing a more precise calculation of the turbulent viscosity;
2. The enhanced model was then treated with Partially-Averaging paradigm thus creating a PANS version of the model.

The new model is thus called $v^2 - f$ with variable C_μ PANS, and was then validated using the benchmark case of the bakwards-facing step. With this validation, the model has shown a far superior behavior compared to the first original model (Realizable $k - \varepsilon$ PANS) and to the literature Standard $k - \varepsilon$ PANS, especially for cases where f_k filter-width value is very high, whereas, on the contrary, the other two models degraded quickly the results as the f_k increased.

As with any new turbulence model, also for these new models further validation activities will be needed, together with the deepening concerning the dynamic definition of the filter parameter f_k , as well as the development of specific boundary conditions to solve specifically the problem of the reproduction of the Atmospheric Boundary Layer. The use of PANS models for the purpose of reproducing environmental conditions is still to be explored and represents one of the main directions of future developments. The results here obtained are, however, found to provide precious information since they indicates that the $v^2 - f$ with variable C_μ PANS model, despite requiring an increased requirement for the grid refinement at the wall, provides an improved result in the rest of the domain, considering the same level of grid refinement in the rest of the domain, also for high f_k values and thus appears to be more suitable for the adoption in the calculation of time-varying wind loads on megastructures.

Within the chapter on the application of wind-induced fatigue calculation on a real structure, the calculation methods to be considered to evaluate the effects of wind on a megastructure by means of PANS models are discussed, indicating the future directions of subsequent development to this research project. The use of PANS models in the case of a megastructure therefore represents a natural point of continuation of this research activity and will allow to close the wind-induced fatigue computation loop entirely numerically.

Chapter 7. Conclusions

This will allow, together with a matured awareness of the phenomenon of wind-induced fatigue, to design more durable, safe and cost-efficient megastructures.

List of Abbreviations

ABL	Atmospheric Boundary Layer
AIJ	Architectural Institute of Japan
ASTM	American Society for Testing and Materials
BIM	Building Information Model
BLWT	Boundary-Layer Wind Tunnel
CAARC	Commonwealth Advisory Aeronautical Council
CDRFG	Consistent Discrete Random Flow Generator
CFD	Computational fluid dynamics
CHS	Circular Hollow Section
CNR	Consiglio Nazionale delle Ricerche
CPU	Central Processing Unit
DES	Detached Eddy Simulation
DFSEM	Divergence Free Synthetic Eddy Method
DNS	Direct Numerical Simulation
DOF	Degree of Freedom
ECCS	European Convention for Constructional Steelwork
ERCOFTAC	European Research Community On Flow, Turbulence And Combustion
FE	Finite Element
FEA	Finite Element Analysis
FEM	Finite Element Model
HPC	High Performance Computing

Chapter 7. Conclusions

IIW	International Institute of Welding
ISO	International Organization for Standardization
LES	Large Eddy Simulation
LHS	Left-Hand Side
LK	Launder, Kato
LRN	Low-Reynolds Number
MMK	Murakami, Mochida, Kondo
NDT	Non-Destructive Testing
NSIF	Notch Stress Intensity Factor
PANS	Partially Averaged Navier Stokes
PISO	Pressure Implicit with Splitting of Operators
PSD	Power Spectral Density
PSD	Power Spectral Density
QUICK	Quadratic Upstream Interpolation for Convective Kinematics
RANS	Reynolds-Averaged Navier Stokes
RNG	Re-Normalization Group
SED	Strain Energy Density
SFS	Sub-Filter Stress
SGS	Sub-Grid Stresses
SLS	Service Limit State
ULS	Ultimate Limit State
URANS	Unsteady RANS
VSG	Virtual Strain Gauge
WTT	Wind Tunnel Test
ZT	Zero-Transport

List of Figures

1.1	Very fine mesh suggested to be used for hot spot stress based approaches [18]	7
2.1	Politecnico di Milano Wind Tunnel facility	37
3.1	Sample application of the Rainflow algorithm [88]	50
3.2	Stress cycle density distribution (left) and stress cycle exceedance distribution (right)	51
3.3	Mean-amplitude stress cycles distribution [109]	51
3.4	Number of gust loads N_g for an effect $\Delta S/S_k$ during a 50 years period	57
3.5	Sensitivity of the fatigue damage on the main relevant parameters [108]	58
3.6	Directionality effect on the fatigue damage [108]	58
3.7	Example of fatigue details according to the Eurocode 1-9	60
3.8	Fatigue strength curves for direct stress ranges according to the Eurocode 1-9	61
3.9	Fatigue strength curves for direct stress ranges according to the IIW .	62
3.10	Example of shell finite element mesh and stress offsets to compute “local” nominal stress components. [92]	63
3.11	Stress fields near a weld toe under linear elastic hypothesis [92]	64
3.12	Example of block loading with three stress amplitudes [97]	65
3.13	Temporal representation of wind velocity: (a) real; (b) simplified [116]	66
3.14	Recommended values of the Eurocode 1-9 for the partial factor γ_{Mf} .	67

List of Figures

3.15	Schematic of fatigue reliability assuming damage tolerant and safe life methods and a failure with high consequence [113]	68
4.1	Wind-induced fatigue calculation	75
4.2	Wind simulation flow chart	76
4.3	Modal analysis	79
4.4	Statistical wind analysis	81
4.5	Cycle counting flow chart	84
4.6	Strain gauges in literature and in experimental tests	85
4.7	Local shell FE model of a connection	85
4.8	Sample VSGs	86
4.9	Detailed fatigue calculation	90
4.10	Visualuzation of free edes (blue) and base material (purple)	91
4.11	Toe checks to be performed along the weld	92
4.12	Toe checks to be performed at the start and finish of the weld	92
4.13	Root checks to be performed along the weld	93
4.14	Relevant stresses considered for the check	94
4.15	Stress concentrations effects	95
5.1	Triple decomposition of a turbulent, unsteady signal	104
5.2	Square cylinder: computational domain	105
5.3	Streamwise mean velocity along the center line. Left: wake region, right: recirculation region	106
5.4	Streamwise mean velocity along vertical line at $x/D = 0.5$	107
5.5	Comparison of streamwise Reynolds stress profile for different turbulence models	107
5.6	Comparison of streamwise Reynolds stress profile for different turbulence models	108
5.7	Comparison of pressure coefficients for different turbulence models	108
5.8	Coherent structures calculated using Q-criterion with $Q = 0.05$	109
5.9	Backwards facing step computational domain	110
5.10	Top: streamwise mean velocity profiles behind the step. Bottom: rms velocity profiles. Comparison with $f_k = 1.0$	113
5.11	Coherent structures calculated using Q-criterion with $Q = 10000$ for URANS Realizable $k - \varepsilon$	113
5.12	Top: streamwise mean velocity profiles behind the step. Bottom: rms velocity profiles. Comparison with $f_k = 0.7$	114

List of Figures

5.13	Coherent structures calculated using Q-criterion with $Q = 10000$ at $f_k = 0.7$	114
5.14	Top: streamwise mean velocity profiles behind the step. Bottom: rms velocity profiles. Comparison with $f_k = 0.45$	115
5.15	Coherent structures calculated using Q-criterion with $Q = 10000$ at $f_k = 0.45$	115
5.16	Top: streamwise mean velocity profiles behind the step. Bottom: rms velocity profiles. Comparison with $f_k = 0.2$	116
5.17	Coherent structures calculated using Q-criterion with $Q = 10000$ at $f_k = 0.2$	116
6.1	Roof structure of the AEK Stadium in Athens	122
6.2	Strut-and-tie behaviour of the hanging system	123
6.3	Layout of the restraints	123
6.4	Membrane roof system	124
6.5	Main truss and rafter system	124
6.6	Main truss typical joint	125
6.7	First cantilever modes of a long roof side (Mode 1) and of a short roof side (Mode 5)	125
6.8	Examples of low frequency global modes (Mode 6 and 7)	126
6.9	Local anti-symmetric mode of a long roof side (Mode 17) and of a short roof side (Mode 34)	126
6.10	Location of the station (red dot) and building site (blue dot) (Map from OpenStreetMap)	127
6.11	Ground roughness on the surroundings of the station site (red dot) (Map from OpenStreetMap)	127
6.12	Joint occurrence of wind speeds and sectors	129
6.13	Fitting of wind data to Weibull distribution curves	129
6.14	Polar representation of the joint probability distribution of wind speeds and sectors	131
6.15	Matching between statistical directional sector and simulated directions	132
6.16	Number of hours of occurrence of basic wind speeds (continuous line) and of wind speeds at the roof height (dots) for each simulated direction	133
6.17	BLWT of the Politecnico di Milano with AEK model	133
6.18	Model of the AEK stadium	134

List of Figures

6.19	Layout of the pressure taps over the roof and detail view of the high-density panel	134
6.20	Experimental admittance functions and ULS envelope	135
6.21	Moving average filter with $K = 1$	137
6.22	Load patch type	137
6.23	Load patch layout	137
6.24	Detail of the computational grid	141
6.25	Structural damping ratio adopted for the dynamic analysis	143
6.26	Observed nodes on the roof	144
6.27	PSD of the displacement at 21 m/s (direction +90)	144
6.28	PSD of the displacement at 7 m/s (direction +90)	145
6.29	PSD of the displacement at 21 m/s (direction -140)	145
6.30	PSD of the displacement at 7 m/s (direction -140)	145
6.31	PSD of the displacement at 21 m/s (direction 180)	146
6.32	PSD of the displacement at 7 m/s (direction 180)	146
6.33	Local shell FE model of a connection	148
6.34	Joint position in the global model	148
6.35	Sample solutions of the shell FE model with unitary displacements applied at the boundary	148
6.36	Virtual strain gauges selected in the connection (red markers)	149
6.37	Time history of stress at a VSG (blue line), peaks and valleys of measured cycles (markers), largest range (red line)	150
6.38	Fatigue load distribution at a VSG	151
6.39	Selected VSG	151
6.40	Computed cycles at a VSG for each wind direction	152
6.41	Computed cycles at a VSG for each wind direction	153
6.42	Local shell FE mode with the application of the boundary conditions that introduce the highest stress cycle in the sample VSG	154
6.43	Sample weld nearby the VSG. Blue and green cylinders represent the weld fillet at the sides (the two cylinders are not actual finite elements used in the calculation).	156
6.44	Summary report of the 28 checks performed on the selected weld	156
6.45	Cumulated damage for check f at weld start	157
6.46	Cycles distribution for check f at weld start	158
6.47	Damage distribution over different directions on selected VSG	159
6.48	Cumulated damage over different directions on selected VSG	160

List of Tables

3.1	Sample application of the Rainflow algorithm [88]	50
3.2	Hypothesis of wind-induced fatigue approach in CNR-DT 207 R1/2018 compared to requirements of wind-induced fatigue in megastructures .	59
4.1	Toe checks to be performed along the weld	92
4.2	Toe checks to be performed at the start and finish of the weld	93
4.3	Root checks to be performed along the weld	93
5.1	Results on square cylinder for various cases	106
5.2	Maximum reverse velocity (Exp.: $0.33U_\infty$)	111
5.3	Comparison of reattachment lengths x/H . $(x/H)_{exp} = 7.0$	111
6.1	Conversion factor of the recorded wind speeds based on the ground roughness for each statistical direction	128
6.2	Weibull parameters for each direction	130
6.3	List of considered wind tunnel simulations	138
6.4	List of ij transient simulations related to $i - th$ direction and $j - th$ velocity level	142

Acknowledgement

I would like to express my sincere thanks to Cimolai S.p.A. who supported this research activity financially and in particular to my corporate tutor, Eng. Catanzano, who first believed in this research project and who was a source of knowledge and guidance for the entire duration of my doctorate.

I would also like to express my deep gratitude to my academic supervisor Prof. Filippo Berto and to my academic co-supervisor Eng. Marco Antonello. Their contribution to my research activity has been invaluable.

The support of my colleagues, in particular Luca, Yuriy and Roberto, was also very important for the success of my thesis and I would like to extend my thanks to them as well.

Finally, I would like to thank Elisa for her constant encouragement during my studies, and also my family.

